Terahertz Spectroscopy of Low-dimensional Spin Systems

Dan Hüvonen

Supervisors: Urmas Nagel, Toomas Rõõm
National Institute of Chemical Physics and Biophysics

May 5, 2008

Contents

Chapter 1

Introduction

Low-dimensional quantum spin systems have received considerable attention during the past decade both from theoretical and experimental points of view. Investigations of two-dimensional superconducting cuprates and the search for related transition-metal oxides opened up a fascinating field of copper oxide compounds, vanadates, manganites and nickelates. Transition-metal oxides possess open d and f electron shells, where electrons are spatially confined to orbitals close to nuclei. These systems fall within two well understood theoretical limits: on one side, there are metals with weakly correlated electrons which are suitably described by band theory, and on the other side there are insulators which are better treated in the real space picture as a collection of localized charges. Between the two limits, in strongly correlated systems, the charges cannot be described as fully itinerant, nor fully localized at their atomic sites. These compounds show effects of strong electronic correlations and magnetism in low dimensions, in particular interplay between spin, charge and orbital degrees of freedom.

The theory of magnetism in one dimension has a history reaching back to the origin of quantum mechanics. This is due to the fact that a spin chain allows to obtain analytical or numerical solutions more easily. It was found that the suppression of "simple" long-range magnetic order reveals an enormous variety of possible ground states, exotic quasiparticles and many-body states. Recent theoretical progress has enabled a more detailed understanding of these effects. Parameters like dimerization, frustration, interchain coupling and spin-phonon coupling have an important impact on the ground state and the excitations of a quantum spin system.

A central concept in describing these low-dimensional quantum spin systems is that of a spin liquid where the ground state is dominated by strong

quantum fluctuations, pronounced spin-spin correlations and suppression of long-range magnetic order. The Heisenberg chain with isotropic antiferromagnetically coupled s=1/2 spins represents such a state in the sense that the spin-spin correlations decay algebraically and it can be denoted as a critical spin liquid. An interesting situation occurs when competing interactions lead to a sudden change of the excitation spectrum, e.g., the opening of an excitation gap or the formation of long-range magnetic order. These quantum phase transitions are controlled by the exchange coupling parameters, the exchange topology or by spin vacancies or can be driven by external parameters, such as magnetic field or pressure. The excitation gap may be realized with or without a spontaneously broken translational symmetry.

Experimental data that provides reference for theory is of essential importance in studying materials with such volatile properties. In an attempt to clarify the microscopic mechanisms behind peculiar properties, a variety of experimental probes - inelastic neutron scattering, nuclear magnetic resonance, electron spin resonance, X-ray diffraction and different optical measurements are often applied by specialists of respective fields, but nevertheless far-infrared optics measurements in magnetic fields have proven to supplement important information about low-energy properties of such materials. Very high sensitivity accompanied with polarization control and strong magnetic fields make the results obtained with terahertz optical spectroscopy setup at the National Institute of Chemical Physics and Biophysics in Tallinn unique. Current thesis is based on three recent publications [1, 2, 3] (provided in the Appendix), where author's contribution has been to both the experimental and the evaluational parts of the work. While the thesis concentrates on the spin chain and ladder compound $Sr_{14}Cu_{24}O_{41}$ [1] there exists an overlap with other quantum magnets that we have studied - a zig-zag chain material α'-NaV_2O_5 [2] and a 2D Shastry-Sutherland model compound $SrCu_2(BO_3)_2$ [3]. Namely, the magnetic ground state is separated from the first excited state by an energy gap in all these materials due to a dimerized spin configuration. The selection rules of the observed far-infrared excitations across this energy gap have called for a new theoretical approach - the dynamic Dzyaloshinskii-Moriya model that surprisingly proved to be successful in explaining singlet to triplet transitions in all three compounds.

The study of the physical properties of $Sr_{14}Cu_{24}O_{41}$ has kept researchers busy for over a decade and about 50 high quality publications in leading condensed matter physics journals (Physical Review Letters, Physical Review B, Physica B, Nature, Science) report findings on this material and its doped derivatives. Nevertheless, there is a lack of consensus in the literature

regarding spin and charge order in the chains of $Sr_{14}Cu_{24}O_{41}$ and the nature of the underlying ground state. We studied magnetic excitations using far-infrared (FIR) spectroscopy and strong magnetic fields with the aim to identify the spin states present in the chains of $Sr_{14}Cu_{24}O_{41}$.

This thesis mostly refers a recent study on $Sr_{14}Cu_{24}O_{41}$, but in an attempt to give self-contained story it starts from the construction of a spin Hamiltonian and describes the FIR experiment in detail before discussing the experimental results. The relevant part of the current thesis is organized into six chapters. The first chapter lines out the motivation for studying low energy properties of quantum magnets. The second chapter introduces the mathematical formalism for describing properties of spin systems, which will gradually be made more complicated to lead to observable results. The third chapter gives the layout and basic working principles of the experimental setup used in the current study. The fourth chapter concentrates on experimental results and discussions. The fifth chapter expands the discussion on the experimental results to singlet to triplet absorption selection rules in α'-NaV_2O_5, $SrCu_2(BO_3)_2$ and $Sr_{14}Cu_{24}O_{41}$. The sixth chapter contains conclusive remarks.

Support by Estonian Science Foundation grants 3443, 4926, 4927, 5553, 6138 and 7011 is acknowledged. National High Magnetic Field Laboratory is supported by NSF Cooperative Agreement No. DMR-0084173, by the State of Florida, and by the DOE. D.Hüvonen's visit to the NHMFL was supported by travel scholarship V.05-06/13 from the Archimedes Foundation.

I wish to express my gratitude to all collaborators, namely professors J. Akimitsu, H. Kageyama, R. K. Kremer and T. Timusk for providing various samples and for helpful discussions. Professor M. Dressel, P. Haas, J. Hwang, Y.-J. Wang for use of experimental facilities and discussions. I am most thankful to my supervisors T. Rõõm and U. Nagel for taking the time to teach me how scientific discoveries are made in contemporary science and the amount of dedication it demands.

I dedicate this thesis to my parents whose constant support has enabled me to pursue my interests.

Chapter 2

Theoretical principles

2.1 Spin Hamiltonian

Magnetic properties that are discussed throughout this thesis arise from electrons. It has been experimentally found that an electron possesses an intrinsic magnetic moment, or spin. The existence of such a moment is a consequence of relativistic considerations that are governed by the Dirac wave equation. Details can be found in various quantum mechanics textbooks (e.g. [4, 5]). We will limit our discussion to necessary definitions and the introduction of the effective spin Hamiltonian.

The quantum spin state of a spin-1/2 particle can be described by a complex-valued vector with two components, called a two-component spinor. When spinors are used to describe quantum states, quantum mechanical operators are represented by 2×2, complex Hermitian matrices.

The Pauli spin matrices are

$$\sigma_x = \begin{pmatrix} 0 & 1 \\ 1 & 0 \end{pmatrix}, \sigma_y = \begin{pmatrix} 0 & -i \\ i & 0 \end{pmatrix}, \sigma_z = \begin{pmatrix} 1 & 0 \\ 0 & -1 \end{pmatrix}, \mathbf{1} = \begin{pmatrix} 1 & 0 \\ 0 & 1 \end{pmatrix}. \tag{2.1}$$

Two spinors $\begin{pmatrix} 1 \\ 0 \end{pmatrix}$ and $\begin{pmatrix} 0 \\ 1 \end{pmatrix}$ form the complete basis for the Hilbert space describing the spin-1/2 particle. Thus, linear combinations of these two states can represent all possible states of the spin.

A convenient way of presenting quantum mechanics is using the operator representation. Spin operator components are defined as

$$\hat{S}^i = s\sigma_i$$

where $i = (x, y, z)$ and $s = \frac{1}{2}$ in units of $\hbar$. Usual angular momentum operator commutation rules apply.

In operator representation spinors are replaced by basis state vectors

$$\begin{pmatrix}1\\0\end{pmatrix} = |\uparrow\rangle\,, \quad \begin{pmatrix}0\\1\end{pmatrix} = |\downarrow\rangle. \tag{2.2}$$

After doing the algebra using Pauli matrices and spinors we get the following non-zero coupling amplitudes between spin states for spin operator components:

$$\begin{aligned}
&\langle\downarrow|\hat{S}_x|\uparrow\rangle = \langle\uparrow|\hat{S}_x|\downarrow\rangle = 1/2,\\
&\langle\downarrow|\hat{S}_y|\uparrow\rangle = -\langle\uparrow|\hat{S}_y|\downarrow\rangle = i/2,\\
&\langle\uparrow|\hat{S}_z|\uparrow\rangle = -\langle\downarrow|\hat{S}_z|\downarrow\rangle = 1/2.
\end{aligned} \tag{2.3}$$

In insulating crystals the dominant interaction between electron spins that gives rise to the magnetic properties is called the exchange interaction. The forces between electrons are electrostatic and therefore independent of spin, but Pauli principle, which requires antisymmetrization of wavefunctions, leads to correlation of spin orientations. Magnetic dipoles, associated with spins, interact directly, but since this interaction decays proportionally to r^3, it is far too weak to compete with electrostatic energy and is generally ignored.

The electronic interaction energy for two localized electrons can be written as

$$E = C - 2J(\hat{S}_1 \cdot \hat{S}_2 + \frac{1}{4}). \tag{2.4}$$

Where the Coulomb energy (C) and the exchange interaction (J) are given by

$$\begin{aligned}
C &= \int\int \psi_1^*(r_1)\psi_2^*(r_2)\tfrac{e^2}{|r_1-r_2|}\psi_1(r_1)\psi_2(r_2)d\tau_1 d\tau_2\\
&= \int\int \tfrac{e^2}{|r_1-r_2|}|\psi_1(r_1)|^2|\psi_2(r_2)|^2 d\tau_1 d\tau_2, \qquad (2.5)\\
J &= \int\int \psi_1^*(r_1)\psi_2^*(r_2)\tfrac{e^2}{|r_1-r_2|}\psi_1(r_2)\psi_2(r_1)d\tau_1 d\tau_2. \qquad (2.6)
\end{aligned}$$

The name "exchange interaction" comes from the fact that operator J exchanges spins 1 and 2 providing the system with a possibility to lower the energy depending on the relative orientation of the spins of the two electrons. One can easily see from from Eq. 2.4 that in case of $J > 0$ (ferromagnetic exchange interaction) the spins favor parallel configuration and antiparallel configuration minimizes energy in case of $J < 0$ (antiferromagnetic exchange interaction). It can be shown (e.g. [4]) that the exchange constant for direct exchange (Fig. 2.1a) is always positive. For antiferromagnetic exchange

to occur the so-called superexchange interaction is necessary, proposed by Kramers[6] and studied in more detail by Anderson [7]. This kind of spin coupling is characterized by an additional anion being situated between the magnetic ions which mediates the spin correlation (Fig. 2.1b). In practice the minus sign is usually dropped from the Hamiltonian for simplification, but with knowledge that the sign of J has to be reversed.

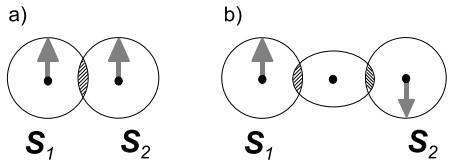

Figure 2.1: Exchange interactions: a) direct exchange interaction b) superexchange interaction via nonmagnetic ligand

As far as magnetic properties of materials are concerned it suffices to consider only the spin dependent part. Consequently, for two coupled spins the Hamiltonian can be written:

$$\hat{H} = J\hat{S}_1 \cdot \hat{S}_2. \tag{2.7}$$

The full basis for a spin dimer has 4 elements $\psi = |\uparrow\uparrow, \uparrow\downarrow, \downarrow\uparrow, \downarrow\downarrow\rangle$. Since

$$\hat{H} = J\hat{S}_1 \cdot \hat{S}_2 = J(\hat{S}_1^x \cdot \hat{S}_2^x + \hat{S}_1^y \cdot \hat{S}_2^y + \hat{S}_1^z \cdot \hat{S}_2^z), \tag{2.8}$$

we can use equations 2.3 and easily calculate the matrix elements of $\hat{H}$. The Hamiltonian in matrix form for this basis is

$$\hat{H}_{Jsp} = \begin{pmatrix} \frac{1}{4}J & 0 & 0 & 0 \\ 0 & -\frac{1}{4}J & \frac{1}{2}J & 0 \\ 0 & \frac{1}{2}J & -\frac{1}{4}J & 0 \\ 0 & 0 & 0 & \frac{1}{4}J \end{pmatrix}. \tag{2.9}$$

Diagonalization of 2.9 yields an antisymmetric singlet state with an eigenvalue $-3/4J$ and three symmetric triplet states with eigenvalues $1/4J$. It is natural to use the obtained dimer eigenfunctions as a new basis when investigating systems containing dimer subunits. The singlet-triplet basis

vectors are

$$\begin{aligned} |S\rangle &= \frac{1}{\sqrt{2}}(|\uparrow\downarrow\rangle - |\downarrow\uparrow\rangle), \\ |T_-\rangle &= |\downarrow\downarrow\rangle, \\ |T_0\rangle &= \frac{1}{\sqrt{2}}(|\uparrow\downarrow\rangle + |\downarrow\uparrow\rangle), \\ |T_+\rangle &= |\uparrow\uparrow\rangle. \end{aligned} \tag{2.10}$$

In general case the J coupling is anisotropic and a variety of physically important models stem from its anisotropy. For an anisotropic J we can write

$$\hat{H} = J_{xx}\hat{S}_1^x \cdot \hat{S}_2^x + J_{yy}\hat{S}_1^y \cdot \hat{S}_2^y + J_{zz}\hat{S}_1^z \cdot \hat{S}_2^z). \tag{2.11}$$

By choosing particular form for J different models have been defined:
$J_{xx} = J_{yy} = 0, J_{zz} \neq 0$ is the Iising model,
$J_{xx} \neq J_{yy} \neq 0, J_{zz} = 0$ is the XY model,
$J_{xx} = J_{yy} \neq 0, J_{zz} \neq 0$ is the XXZ model,
$J = J_{xx} = J_{yy} = J_{zz}$ is the Heisenberg model.
For a detailed analysis of physics behind all these models the reader should refer to the book by Bill Sutherland [8].

To account for external magnetic field ($\mathbf{B_0}$) effects the Zeeman coupling term must be included in the Hamiltonian. In our one dimer system the Hamiltonian becomes

$$\hat{H} = J\hat{S}_1 \cdot \hat{S}_2 + \mu_B \mathbf{B_0} \cdot \mathbf{g_1} \cdot \hat{S}_1 + \mu_B \mathbf{B_0} \cdot \mathbf{g_2} \cdot \hat{S}_2, \tag{2.12}$$

where $\mathbf{g_1}$ and $\mathbf{g_2}$ are the gyromagnetic ratio tensors for the respective spins and μ_B is the Bohr magneton. For spins in uniform crystal fields $\mathbf{g_1} = \mathbf{g_2}$ we can simplify the Hamiltonian to

$$\hat{H} = J\hat{S}_1 \cdot \hat{S}_2 + \mu_B g \mathbf{B_0} \cdot (\hat{S}_1^z + \hat{S}_2^z), \tag{2.13}$$

where the scalar g now denotes the $\mathbf{g}$ tensor value along the primary axis that is aligned with the field and the spin quantization axis.

Considering only two spins when discussing bulk properties where the spin density is in the order of 10^{20} cm^{-3} seems controversial. Strictly speaking, for bulk material one should sum over all spin-spin interactions in the material. However, the first simplification arises from that the exchange interactions become negligible between distant spins. In many cases it suffices to only account for few nearest-neighbor spin interactions.

A model relevant for the current thesis is the one-dimensional infinite Heisenberg spin 1/2 chain with alternating antiferromagnetic coupling constants $J_1 > J_2 > 0$, given by the following Hamiltonian

$$\hat{H} = \sum_{i}^{N} J_1 \hat{S}_{2i-1} \cdot \hat{S}_{2i} + J_2 \hat{S}_{2i} \cdot \hat{S}_{2i+1}. \tag{2.14}$$

There are several approximate results depending on the ratio J_1/J_2 to analytically predict the formation of the spin gap. Thermodynamics of different 1D spin 1/2 chains is analyzed by series expansion in a comprehensive paper by Johnston *et al.* [9] starting from an uniform chain limit (J_2=J_1) with no spin gap up to a fully dimerized chain limit (J_2=0) where the ground state is a product of singlets. Exact results can be obtained by diagonalization of a finite length chain Hamiltonian by implementing a periodic boundary condition $S_{N+1} = S_1$. The finite-size Hamiltonian can be solved numerically and system behavior described qualitatively although quantitative values become renormalized due to finite-size effects.

2.2 Dzyaloshinskii-Moriya interaction

The anti-symmetric Dzyaloshinskii-Moriya (DM) interaction is a combination of superexchange and spin-orbital interactions and is linear in spin-orbital coupling. Dzyaloshinskii gave a phenomenological explanation in 1958 [10] that weak ferromagnetism in antiferromagnets is possible without destroying the symmetry of the original state. Later Moriya [11] derived the same result rigorously using Anderson formalism.

Using second-order perturbation theory, Moriya (Eqs. 2.3 and 2.4 in Ref. [11]) derived a general effective spin Hamiltonian describing interaction between two spins

$$\hat{H}_S = J\hat{S}_k \cdot \hat{S}_l + \hat{S}_k \cdot \overleftrightarrow{A}_{\mathbf{kl}} \cdot \hat{S}_l + \mathbf{D}_{kl} \cdot \hat{S}_k \times \hat{S}_l. \tag{2.15}$$

The first term represents the isotropic symmetric exchange. The second and the third terms are the symmetric ($\overleftrightarrow{A}_{kl} = \overleftrightarrow{A}_{lk}$) and antisymmetric ($\mathbf{D}_{kl} = -\mathbf{D}_{lk}$) anisotropies.

The anti-symmetric DM interaction has the form

$$\hat{H}_{DM} = \mathbf{D} \cdot [\hat{S}_1 \times \hat{S}_2]. \tag{2.16}$$

For a particular spin system the allowed components of the DM interaction are determined by the symmetry of the spin complex, Fig. 2.2. The orientation of the DM vector is determined by the vector product of the vectors

connecting two spins over the superexchange path[12, 13]

$$\frac{\mathbf{D}}{|\mathbf{D}|} = [\mathbf{R}_{S_1,O} \times \mathbf{R}_{O,S_2}] \tag{2.17}$$

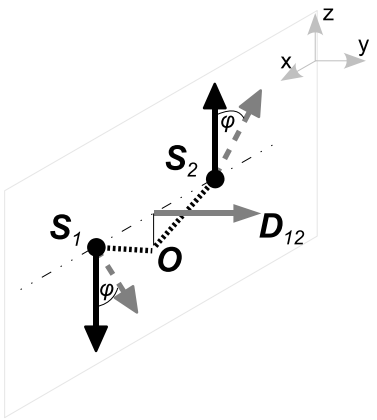

Figure 2.2: Effect of Dzyaloshinskii-Moriya interaction. If the superexchange path $S_1 - O - S_2$ is buckled in negative z-direction then the DM vector D_{12} is parallel to y axis and otherwise antiparallel spins become canted by an angle ϕ in (xz) plane.

However, as was pointed out by Shekhtman [14] in 1992, Moriya's derivation overlooked some symmetric anisotropy terms. The Dzyaloshinskii-Moriya interaction with first and second order symmetric corrections (Eq.(2.19) from Ref.[15]) is

$$\hat{H} = -\frac{|\mathbf{D}|^2}{4J}\hat{S}_1 \cdot \hat{S}_2 + \frac{1}{2J}\hat{S}_1 \cdot \mathbf{DD} \cdot \hat{S}_2 + \hat{H}_{DM}, \tag{2.18}$$

where the first term gives a correction to the isotropic part and the second, dyadic term, has the form of $\overleftrightarrow{A}$ in (2.15) giving corrections to both isotropic and anisotropic parts of the spin Hamiltonian. Summing up all interactions, the full Hamiltonian for a spin pair in magnetic field becomes

$$\hat{H} = (J - \frac{|\mathbf{D}|^2}{4J})\hat{S}_1 \cdot \hat{S}_2 + \frac{1}{2J}\hat{S}_1 \cdot \mathbf{DD} \cdot \hat{S}_2 + \mathbf{D} \cdot [\hat{S}_1 \times \hat{S}_2] + \mu_B g \mathbf{B_0} \cdot (\hat{S}_1 + \hat{S}_2). \tag{2.19}$$

The spin quantization axis z is chosen parallel to the applied field $\mathbf{B}_0$. The relative orientation of the DM vector $\mathbf{D}$ to the external magnetic field direction gives two qualitatively different cases - the field is parallel or the field is perpendicular to the DM vector. Taking a state vector $|\Psi\rangle =$

$(\mathrm{T}_+, \mathrm{T}_0, \mathrm{T}_-, \mathrm{S})$ in the singlet-triplet basis and $\mathbf{B}_0 \parallel \mathbf{D} \parallel \mathbf{z}$ the Hamiltonian 2.19 in matrix form becomes

$$H = \begin{pmatrix} \frac{1}{4}J + \frac{1}{16}\frac{D^2}{J} + G_z & 0 & 0 & 0 \\ 0 & \frac{1}{4}J - \frac{3}{16}\frac{D^2}{J} & 0 & -\frac{1}{2}\imath D \\ 0 & 0 & \frac{1}{4}J + \frac{1}{16}\frac{D^2}{J} - G_z & 0 \\ 0 & \frac{1}{2}\imath D & 0 & -\frac{3}{4}J + \frac{1}{16}\frac{D^2}{J} \end{pmatrix}, \tag{2.20}$$

where $G_z = g\mu_B B_0$ is the Zeeman term. One can see that the DM interaction has two effects on the eigenvalues of the dimer states. Firstly, the symmetric part adds a correction to the eigenvalues, $-3D^2/(16J)$ to $|\mathrm{T}_0\rangle$ and $D^2/(16J)$ to other states. Secondly, the antisymmetric part mixes $|\mathrm{T}_0\rangle$ and $|\mathrm{S}\rangle$ states as seen from off-diagonal matrix elements. Diagonalization of 2.20 gives new dimer states that are denoted as $\mathrm{t}_+, \mathrm{t}_0, \mathrm{t}_-, \mathrm{s}$. The states $|\mathrm{t}_+\rangle$ and $|\mathrm{t}_-\rangle$ are still pure $|\mathrm{T}_+\rangle$ and $|\mathrm{T}_-\rangle$ states respectively, but $|\mathrm{t}_0\rangle$ and $|\mathrm{s}\rangle$ states are linear combinations of $|\mathrm{T}_0\rangle$ and $|\mathrm{S}\rangle$ states. For arbitrarily chosen $J = 1, D = 0.4$, the eigenvalues are plotted on Fig. 2.3a.

For $\mathbf{B}_0 \perp \mathbf{D} \parallel \mathbf{y}$ orientation the matrix reads

$$H = \begin{pmatrix} \frac{1}{4}J - \frac{1}{16}\frac{D^2}{J} + G_z & 0 & -\frac{1}{8}\frac{D^2}{J} & \frac{\sqrt{2}}{4}D \\ 0 & \frac{1}{4}J + \frac{1}{16}\frac{D^2}{J} & 0 & 0 \\ -\frac{1}{8}\frac{D^2}{J} & 0 & \frac{1}{4}J - \frac{1}{16}\frac{D^2}{J} - G_z & \frac{\sqrt{2}}{4}D \\ \frac{\sqrt{2}}{4}D & 0 & \frac{\sqrt{2}}{4}D & -\frac{3}{4}J + \frac{1}{16}\frac{D^2}{J} \end{pmatrix}. \tag{2.21}$$

In this field orientation $|\mathrm{T}_-\rangle$ and $|\mathrm{T}_+\rangle$ are mixed into $|\mathrm{S}\rangle$ by $\hat{H}_{DM}$ and $|\mathrm{t}_0\rangle$ remains a pure state, $|\mathrm{t}_0\rangle = |\mathrm{T}_0\rangle$. The eigenvalues of 2.21 are plotted in Fig. 2.3b.

In summary, corrections to the energy spectrum due to the DM interaction are usually small because the correction is proportional to D^2/Δ, where D is the magnitude of the DM interaction and Δ is the separation of the singlet and triplet energy levels (in a single dimer model $\Delta = J$). In addition to the DM interaction there is a symmetric spin-spin interaction that is quadratic in spin-orbital coupling. Although the symmetric interaction does not couple the singlet and triplet states it affects the splitting of the triplet state sublevels. It was shown by Shekhtman *et al.*[14, 15] for a single bond superexchange that the triplet state remains degenerate in zero magnetic field if the full Hamiltonian (2.19) is used.

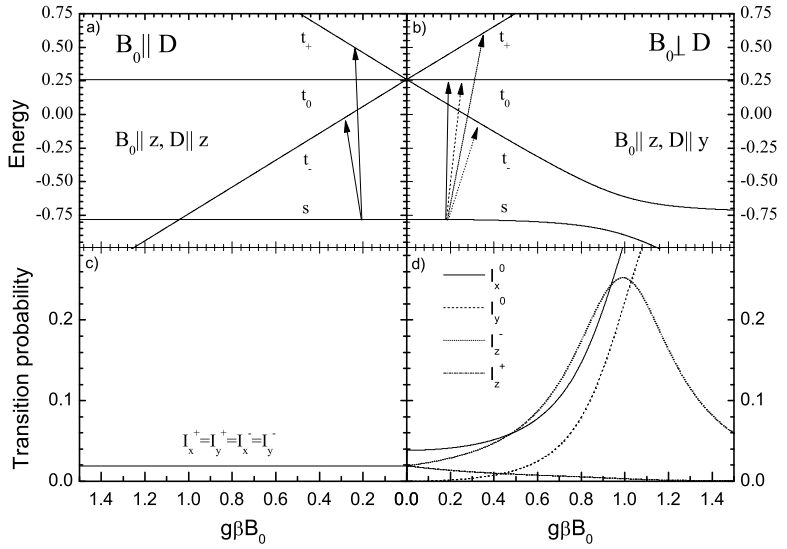

Figure 2.3: Eigenvalues of spin dimer states in the presence of DM interaction and transition probabilities I_i^j for operators $\hat{S}^i$, $i = x, y, z$ from ground state to triplet states $|t_j>$. a) Eigenvalues in $\mathbf{B}_0 \parallel \mathbf{D} \parallel \mathbf{z}$ orientation, b) Eigenvalues in $\mathbf{B}_0 \perp \mathbf{D} \parallel \mathbf{y}$ orientation, c) Magnetic dipole transition intensities from $|s>$ to $|t_j>$ when $\mathbf{B}_0 \parallel \mathbf{D} \parallel \mathbf{z}$, d) Magnetic dipole transition intensities from $|s>$ to $|t_j>$ states in graph b.

2.3 Singlet to triplet excitations

In the following analysis selection rules for a single photon absorption by a system with a singlet ground state are established. It is known from Maxwell equations that electromagnetic radiation must possess time-dependent electric $\mathbf{E}_1$ and magnetic field $\mathbf{H}_1$ components to propagate in space. Consequently there are two possible interaction mechanisms for electromagnetic radiation with matter - electric or magnetic. Electric and magnetic dipole transitions between singlet and triplet states are forbidden in principle. The reason for this is the different parity of the ground singlet state and the excited triplet state. The singlet state is anti-symmetric and the triplet state is symmetric relative to the interchange of two spins.

Since the magnetic field component $\mathbf{H}_1$ interacts with spins the same

way as static field, the magnetic dipole operator can be written

$$\hat{H}_{md} = g\mu_B \mathbf{H}_1 \cdot (\hat{S}_1 + \hat{S}_2). \tag{2.22}$$

It is evident that operator 2.22 is symmetric relative to interchange of spins, $\hat{H}_{md}(1,2) = \hat{H}_{md}(2,1)$. Transition intensity, induced by magnetic dipole operator, is proportional to the square of the matrix element modulus between initial and final states.

$$I_i^j \sim |\langle \mathrm{f}_j | \hat{S}_1^i + \hat{S}_2^i | \mathrm{i} \rangle|^2, i = x, y, z, \tag{2.23}$$

for light polarized along spin coordinates x,y or z.

2.3.1 Heisenberg model

Using relations 2.3 one can explicitly see, using our dimer example, that the magnetic dipole operator does not couple singlet and triplet states. For $\hat{S}^x$ we get

$$\begin{gathered} I \sim |\langle \mathrm{T}_- | \hat{H}_{md} | \mathrm{S} \rangle|^2 = \tfrac{1}{2} |\langle | \hat{S}_1^x + \hat{S}_2^x | \downarrow\downarrow \uparrow\downarrow - \downarrow\uparrow \rangle|^2 = \\ = \tfrac{1}{2} \cdot (\tfrac{1}{2} \cdot 0 - 0 \cdot \tfrac{1}{2})^2 = 0 \end{gathered}$$

$$\begin{gathered} I \sim |\langle \mathrm{T}_0 | \hat{H}_{md} | \mathrm{S} \rangle|^2 = \tfrac{1}{2} \cdot \tfrac{1}{2} |\langle \uparrow\downarrow + \downarrow\uparrow | \hat{S}_1^x + \hat{S}_2^x | \uparrow\downarrow - \downarrow\uparrow \rangle|^2 = \\ = \tfrac{1}{4} \cdot (0 + \tfrac{1}{2} \cdot \tfrac{1}{2} - \tfrac{1}{2} \cdot \tfrac{1}{2} - 0)^2 = 0 \end{gathered} \tag{2.24}$$

$$\begin{gathered} I \sim |\langle \mathrm{S} | \hat{H}_{md} | \mathrm{T}_+ \rangle|^2 = \tfrac{1}{2} |\langle \uparrow\downarrow - \downarrow\uparrow | \hat{S}_1^x + \hat{S}_2^x | \uparrow\uparrow \rangle|^2 = \\ = \tfrac{1}{2} \cdot (0 \cdot \tfrac{1}{2} - \tfrac{1}{2} \cdot 0)^2 = 0 \end{gathered}$$

The same result can be shown to hold for operators $\hat{S}^y$ and $\hat{S}^z$.

The electric dipole operator will not couple to spin states without an extra term in the Hamiltonian and we get a zero transition probability by default. One term that couples electric field component of the light to spin lattice comes from dynamic DM interaction model and is described further in this section.

2.3.2 Heisenberg model and static Dzyaloshinskii-Moriya interaction

In section 2.2 we established that in the presence of DM interaction singlet and triplet states become mixed. Although the corrections to the energy levels are small, the mixing of the singlet and the triplet state by the anti-symmetric interaction could be enough to produce experimentally detectable optical singlet to triplet transitions. The transition probabilities for the magnetic dipole operator in spin chains with DM interactions were calculated by Sakai *et al.* [16]. Calculating as in Eq. 2.24, but with eigenstates ($|\mathrm{t}_+\rangle, |\mathrm{t}_0\rangle, |\mathrm{t}_-\rangle, |\mathrm{s}\rangle$) of Hamiltonian 2.19 we get transition intensities for the dimer model with the DM interaction. Figure 2.3c shows transition intensities from the $|\mathrm{s}\rangle$ state for $\mathbf{B}_0 \parallel \mathbf{D} \parallel \mathbf{z}$ orientation. The alternating magnetic field $\mathbf{H}_1$, polarized along x or y axis (perpendicular to $\mathbf{B}_0$ and $\mathbf{D}$) gives non-zero intensities as shown in Fig. 2.3b. This is because $|\mathrm{s}\rangle$ has the triplet component $|\mathrm{T}_0\rangle$ mixed in and the transitions from $|\mathrm{T}_0\rangle$ to $|\mathrm{T}_-\rangle$ and $|\mathrm{T}_+\rangle$ are allowed by $\hat{S}^x$ and $\hat{S}^y$ operators. The transition probabilities do not depend on the strength of the applied field since the mixing of $|\mathrm{S}\rangle$ and $|\mathrm{T}_0\rangle$ is independent of $\mathbf{B}_0$.

In Fig. 2.3d transition intensities from $|\mathrm{s}\rangle$ state for $\mathbf{B}_0 \perp \mathbf{D} \parallel \mathbf{y}$ orientation are displayed. Transitions to $|\mathrm{t}_-\rangle$ and $|\mathrm{t}_+\rangle$ are observed when $\mathbf{H}_1 \parallel \mathbf{B}_0$ see I_z^- and I_z^+ in Fig. 2.3d. In high magnetic field I_z^- prevails over I_z^+ because the mixing of $|\mathrm{T}_-\rangle$ into the ground state increases and the mixing of $|\mathrm{T}_+\rangle$ decreases. Finite transition probability I_x^0 to the $|\mathrm{t}_0\rangle$ is observed in small fields when $\mathbf{H}_1 \perp \mathbf{B}_0, \mathbf{D}$ whereas $I_y^0 = 0$ ($\mathbf{H}_1 \parallel \mathbf{D}$) as B_0 approaches zero. Both transition probabilities are determined by the amount $|\mathrm{T}_-\rangle$ and $|\mathrm{T}_+\rangle$ are mixed into the ground state, since transition operators $\hat{\mathrm{S}}^{\mathrm{x}}$ and $\hat{\mathrm{S}}^{\mathrm{y}}$ couple these two states to the $|\mathrm{t}_0\rangle = |\mathrm{T}_0\rangle$ state. I_x^0 and I_y^0 gain intensity as the ground state changes into $|\mathrm{T}_-\rangle$ with increasing field.

In summary, the following selection rules are observed for the magnetic dipole transition from singlet to triplet state in the presence of DM interaction. *First*, if the magnetic field is parallel to the DM vector, $\mathbf{D} \parallel \mathbf{B}_0$, transitions to the triplet state sublevels $|\mathrm{t}_-\rangle$ and $|\mathrm{t}_+\rangle$ are observed. These transitions have field-independent intensities and do not depend on polarization in the plane perpendicular to the DM vector, $\mathbf{H}_1 \perp \mathbf{D}$. *Second*, if the magnetic field is perpendicular to the DM vector $\mathbf{B}_0 \perp \mathbf{D}$, then in small fields ($B_0 \ll J/g\mu_B$) the transition to $|\mathrm{t}_0\rangle$ has a weak field dependence and is observed in polarization $\mathbf{H}_1 \perp \mathbf{B}_0, \mathbf{D}$. The transitions to $|\mathrm{t}_-\rangle$ and

$|t_+\rangle$ are observed in $\mathbf{H}_1 \parallel \mathbf{B}_0$ polarization. In this polarization in magnetic fields, $g\mu_B B_0 \geq D$, the transition probability to $|t_-\rangle$ increases and to $|t_+\rangle$ decreases with increasing field.

2.3.3 Heisenberg model and dynamic Dzyaloshinskii-Moriya interaction

The idea that the electric dipole singlet to triplet transition is partially allowed when an optically active phonon lowers the crystal symmetry and therefore creates a dynamic DM interaction, was put forward by Cépas *et al.*[17, 18]. It will be shown that the electric field component of the far-infrared light $\mathbf{E}_1$ that couples to an optically active phonon can cause transitions between singlet and triplet states if this phonon creates a DM interaction by lattice deformation. The derivation is presented in greater detail in Ref. [2].

Electric dipole coupling between the phonon and the light in the long wavelength limit is

$$V = e\mathbf{Q} \cdot \mathbf{E_1}, \tag{2.25}$$

where e is an effective charge associated with a lattice normal coordinate $\mathbf{Q}$.

We expand the DM vector $\mathbf{D}$ into a power series of Q

$$\mathbf{D}(Q) = \mathbf{D}(0) + \frac{\partial \mathbf{D}}{\partial Q}\,|_{Q=0}\, Q + \ldots. \tag{2.26}$$

The first term is the static DM vector in the absence of lattice deformation and was analyzed in section 2.2. Here, for simplicity, $\mathbf{D}(0) = 0$ case will be considered. Quadratic correction terms in $\mathbf{D}$ (Eq. 2.19) are left out, because these symmetric interactions will not give us any transitions between singlet and triplet states. Keeping terms linear in Q we get for the DM interaction (2.16)

$$H_{DMQ} = Q\mathbf{D}_Q \cdot [\hat{S}_1 \times \hat{S}_2], \tag{2.27}$$

where $\mathbf{D}_Q \equiv \frac{\partial \mathbf{D}}{\partial Q}\,|_{Q=0}$. For the phonon system we use the secondary quantization presentation. The lattice normal coordinate Q can be presented in terms of creation and annihilation operators $a^\dagger$ and a, $Q = q(a^\dagger + a)$, where q is the transformation coefficient.

The Hamiltonian of the coupled spin-phonon system becomes

$$H = \hbar\,\omega_p\, a^\dagger a + J\hat{S}_1 \cdot \hat{S}_2 + g\mu_B \mathbf{B}_0 \cdot (\hat{S}_1 + \hat{S}_2) + H^{(1)}_{DMQ}, \tag{2.28}$$

$$H^{(1)}_{DMQ} = q(a^\dagger + a)\mathbf{D}_Q \cdot [\hat{S}_1 \times \hat{S}_2], \tag{2.29}$$

where $\hbar\omega_p$ is the phonon energy. In the low temperature limit the thermal population of phonon states is low, $\langle n \rangle \approx 0$, and we can consider only the phonon states with either 0 or 1 phonon, $|0\rangle$ and $|1\rangle$. Let the state vector be $\Psi = (\mathrm{T}_+1, \mathrm{T}_+0, \mathrm{T}_0 1, \mathrm{T}_0 0, \mathrm{T}_-1, \mathrm{T}_-0, \mathrm{S}1, \mathrm{S}0)$. The Hamiltonian (2.28) is diagonal in this basis except for the last term, $H^{(1)}_{DMQ}$. The eigenstates are labeled by $|\mathrm{s}n\rangle$ and $|\mathrm{t}_i n\rangle$ where $n = 0$ or 1. After diagonalization of the Hamiltonian (2.28) we treat V (2.25) as a time-dependent perturbation to calculate the transition probabilities from the ground state. Like with static DM, two distinct cases must be considered: $\mathbf{D}_Q \parallel \mathbf{B}_0$ and $\mathbf{D}_Q \perp \mathbf{B}_0$.

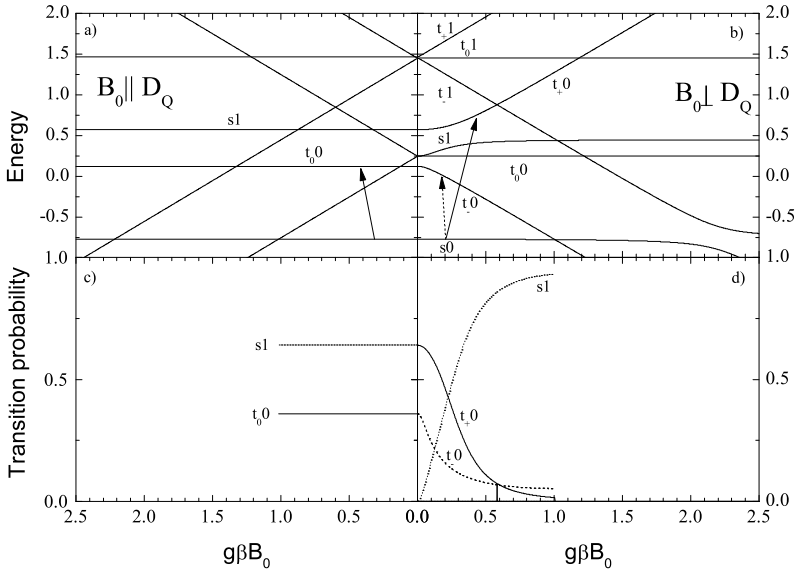

Figure 2.4: Eigenvalues of spin dimer states in the presence of a single phonon mode and dynamic Dzyaloshinskii-Moriya interaction, also transition probabilities from ground state.

$\mathbf{D}_Q \parallel \mathbf{B}_0 \parallel z$. The diagonal elements are the same as in (2.20) except that the phonon energy $\hbar\omega_p$ will be added if $n = 1$. Beside diagonal elements the non-zero elements of the Hamiltonian (2.28) are the ones created by $H^{(1)}_{DMQ}$: $\langle \mathrm{S}1|H^{(1)}_{DMQ}|\mathrm{T}_0 0\rangle = \langle \mathrm{S}0|H^{(1)}_{DMQ}|\mathrm{T}_0 1\rangle = -\langle \mathrm{T}_0 1|H^{(1)}_{DMQ}|\mathrm{S}0\rangle = -\langle \mathrm{T}_0 0|H^{(1)}_{DMQ}|\mathrm{S}1\rangle = \imath q D_Q/2$. The energy levels, calculated for $J = 1$,

$\hbar\omega_p = 1.2$, and $qD_Q = 0.4$, are shown in Fig. 2.4a. The largest repulsion is between $|\mathrm{s}1\rangle$ and $|\mathrm{t}_0 0\rangle$, which are linear combinations of $|\mathrm{S}1\rangle$ and $|\mathrm{T}_0 0\rangle$. The other two mixed states $|\mathrm{S}0\rangle$ and $|\mathrm{T}_0 1\rangle$ give us the ground state $|\mathrm{s}0\rangle$ and $|\mathrm{t}_0 1\rangle$. One has to keep in mind that not only the spin states are mixed, but also the phonon states $|0\rangle$ and $|1\rangle$ are mixed. All other 4 states that involve triplet states $|\mathrm{T}_\pm\rangle$ are pure states.

The splitting of energy levels has to be taken with some precaution. The splitting due to the dynamic DM is observed when there is one phonon excited, $n = 1$. This is not the case at thermal equilibrium at low T when $\langle n\rangle = 0$ (the possible role of zero-point vibrations is ignored in our approach). If the phonon is brought to the state $n = 1$ by the light-phonon interaction (2.25) the effect of one phonon on the shift of energy levels should be observed in the experiment, unless it is much smaller than the lifetime or inhomogeneous broadening of energy levels. The magnitude of the shift and whether it could be observed in the experiment or not will not affect conclusions about the transition probabilities.

Calculation of the transition probability $|\langle \mathrm{t}_j n'|V|\mathrm{s}0\rangle|^2$ is straightforward since V couples states that are diagonal in the basis of pure spin states and non-diagonal in the basis of phonon states $|0\rangle$ and $|1\rangle$. Two transitions from the ground state $|\mathrm{s}0\rangle$ are observed, to $|\mathrm{s}1\rangle$ and $|\mathrm{t}_0 0\rangle$ (Fig. 2.4c). If the dynamic DM is zero, then $|\mathrm{s}0\rangle = |\mathrm{S}0\rangle$, $|\mathrm{s}1\rangle = |\mathrm{S}1\rangle$, and $|\mathrm{t}_0 0\rangle = |\mathrm{T}_0 0\rangle$. The transition from $|\mathrm{s}0\rangle$ to $|\mathrm{s}1\rangle$ is an ordinary absorption of an infrared photon $\hbar\omega_p = E_{\mathrm{s}1} - E_{\mathrm{s}0}$ with probability 1. The transition to $|\mathrm{t}_0 0\rangle$ has zero probability. When the dynamic DM interaction is turned on, additional absorption sets in and a photon with energy $E_{\mathrm{t}_0 0} - E_{\mathrm{s}0}$ is absorbed. This can be viewed as a virtual excitation of a phonon by the light to the state $|1\rangle$ while the spin state remains singlet, and then the dynamic DM interaction (2.27) brings the (virtual) phonon back to $|0\rangle$ while changing the spin state to $|\mathrm{T}_0\rangle$. The polarization of the absorbed photon with respect to the crystal axes is determined by the phonon states involved.

$\mathbf{D}_Q \perp \mathbf{B}_0 \parallel z$. Choosing the dynamic DM vector parallel to y axis, $\mathbf{D}_Q = (0, D_Q, 0)$, we get 8 non-zero elements beside diagonal elements. The energy levels, calculated for $J = 1$, $\hbar\omega_p = 1.2$, and $qD_Q = 0.4$, are plotted in Fig. 2.4b. The strongest mixing occurs between $|\mathrm{S}1\rangle$ and $|\mathrm{T}_\pm 0\rangle$ giving the eigenstates $|\mathrm{s}1\rangle$ and $|\mathrm{t}_\pm 0\rangle$. Also, there is an additional mixing between $|\mathrm{T}_- 0\rangle$ and $|\mathrm{T}_+ 0\rangle$ levels in small fields. In small fields, $g\mu_B B_0 < J$, the mixing of $|\mathrm{S}0\rangle$ and $|\mathrm{T}_\pm 1\rangle$ is less pronounced since their separation is larger than the separation of $|\mathrm{S}1\rangle$ and $|\mathrm{T}_\pm 0\rangle$. Therefore, for the analysis of the transition probabilities the ground state can be taken as pure $|\mathrm{S}0\rangle$ and the transition probabilities are mainly determined by the mixing between $|\mathrm{S}1\rangle$ and $|\mathrm{T}_\pm 0\rangle$.

The effect of mixing of $|\mathrm{T}_{\pm}1\rangle$ into the ground state has a secondary effect on the transition probabilities. Transitions from the ground state to three excited states $|\mathrm{t}_{+}0\rangle$, $|\mathrm{t}_{-}0\rangle$, and $|\mathrm{s}1\rangle$ have non-zero probabilities (Fig. 2.4d). The transition probability to the $|\mathrm{s}1\rangle$ state increases with field because $|\mathrm{s}1\rangle$ changes gradually from the mixed state into $|\mathrm{S}1\rangle$. The transition probabilities to $|\mathrm{t}_{+}0\rangle$ and $|\mathrm{t}_{-}0\rangle$ state decrease as the field increases because the amount of $|\mathrm{S}1\rangle$ mixed into them decreases. Again, the polarization of the absorbed photon with respect to the crystal axes is determined by the phonon states involved.

Analytical results can be obtained in the limit $|E_{\mathrm{S}1} - E_{\mathrm{T}_i 0}| \gg qD_Q$, $i = -, 0, +$. This case holds when $|\hbar\omega_p - (J \pm g\mu_B B_0)| \gg qD_Q$. We find the first order perturbation corrections to the states $|\mathrm{S}n\rangle$ and $|\mathrm{T}_i n\rangle$, where $n = 0, 1$, using $H^{(1)}_{DMQ}$ (2.29) as perturbation. Then the transition probabilities are calculated between the new states $|\mathrm{s}0\rangle$ and $|\mathrm{t}_i 0\rangle$ as was done in the exact treatment.

For $\mathbf{D}_Q \parallel \mathbf{B}_0 \parallel \mathbf{z}$ we get

$$|\langle \mathrm{t}_0 0|V|\mathrm{s}0\rangle|^2 = I_p \frac{(qD_Q)^2(\hbar\omega_p)^2}{[(\hbar\omega_p)^2 - J^2]^2}, \tag{2.30}$$

where $I_p = (eqE_1)^2$ is the light absorption intensity by the infrared-active phonon. The transition probability from $|\mathrm{s}_0\rangle$ to the triplet level $|\mathrm{t}_0\rangle$ is independent of the magnetic field.

For the perpendicular case $\mathbf{D}_Q \perp \mathbf{B}_0 \parallel \mathbf{z}$

$$|\langle \mathrm{t}_- 0|V|\mathrm{s}0\rangle|^2 = I_p \frac{(qD_Q)^2(\hbar\omega_p)^2}{2[(\hbar\omega_p)^2 - (J - g\mu_B B_0)^2]^2}, \tag{2.31}$$

$$|\langle \mathrm{t}_+ 0|V|\mathrm{s}0\rangle|^2 = I_p \frac{(qD_Q)^2(\hbar\omega_p)^2}{2[(\hbar\omega_p)^2 - (J + g\mu_B B_0)^2]^2}. \tag{2.32}$$

If $\hbar\omega_p \ll J$ then the intensity of the transition from $|\mathrm{s}0\rangle$ to $|\mathrm{t}_-0\rangle$ increases with the magnetic field and decreases for the transition to $|\mathrm{t}_+0\rangle$. If $\hbar\omega_p \gg J$ then the intensity of the $|\mathrm{s}0\rangle$ to $|\mathrm{t}_+0\rangle$ transition increases and of $|\mathrm{s}0\rangle$ to $|\mathrm{t}_-0\rangle$ decreases. In the perturbation limit the zero field intensities of the transitions from $|\mathrm{s}0\rangle$ to $|\mathrm{t}_-0\rangle$ and $|\mathrm{t}_+0\rangle$ are equal.

In summary, the following selection rules are obtained for the electric dipole transition from the singlet to the triplet state in the presence of the dynamic DM interaction.

1. The polarization of the transition: $\mathbf{E}_1$ is parallel to the dipole moment of the optically active phonon that creates the dynamic DM interaction.

2. The orientation of the dynamic DM vector $\mathbf{D}_Q$ is determined by the symmetry of the lattice distortion created by the optically active phonon.

3. If $\mathbf{B}_0 \parallel \mathbf{D}_Q$ a magnetic field independent transition probability to the triplet state sublevel $|\mathrm{t}_0 0\rangle$ is observed.

4. If $\mathbf{B}_0 \perp \mathbf{D}_Q$ magnetic field dependent transition probabilities to the triplet state sublevels $|\mathrm{t}_+ 0\rangle$ and $|\mathrm{t}_- 0\rangle$ are observed.

2.3.4 Heisenberg model and a staggered g-tensor

The staggered g-tensor model has been helpful for example in understanding far-infrared absorption in the S=1 antiferromagnetic chain compound NENP [19]. The staggered g-tensor mechanism requires that the principal axes of a pair of spins with anisotropic g-tensors must not coincide. Let us consider for an example the spin $\mathbf{S_1}$ with its principal axes rotated from the crystal a axis by an angle θ and the spin $\mathbf{S_2}$ by an angle $-\theta$ and $\mathbf{B}_0 \parallel \mathbf{a}$. Let the Hamiltonian contain an isotropic exchange interaction and Zeeman interaction, Eq. 2.12. Matrix elements between the singlet and triplet states equal to $\pm B_0(g_a - g_b)\sin\theta\cos\theta$ appear.

The staggered g-tensor has two effects on optical transitions. Firstly, it mixes singlet and triplet states when B_0 is applied. The outcome is that the transition intensity from singlet to triplet state would increase proportionally to $(B_0)^2$ and both triplet levels, +1 and -1, experience the same field dependence. Secondly, the magnetic component of light would interact directly with the staggered part of the spin Hamiltonian. This mechanism is described in the paragraph right above Fig. 3 in Ref. [19], where it is concluded that for the mechanism the intensity does not depend on B_0 and is very weak.

Chapter 3

Experimental details

3.1 Overview of the TeslaFIR spectrometer

The experimental setup used for current work in Tallinn at National Institute of Chemical Physics and Biophysics is called TeslaFIR. This system is optimized for measurements in the far-infrared frequency range and equipped with a 12 Tesla superconducting magnet from Oxford Instruments. The far-infrared or THz frequency range typically ranges from 0.1 to 10 THz and designates the meeting point of optics and electronics. The TeslaFIR setup is excellent for studying excitations in spin systems, which typically have coupling constants in the order of 1 THz and the lowest excitations in the same energy scale. The benefit of having a 12 T magnet in conjunction with terahertz spectroscopy equipment is the ability to detect the splitting of electron spin levels, because the maximum field shifts the electron spin ($g \approx 2$) levels by 0.4 THz. Since the THz frequency range designates the crossover region from electronics to optics, it is also experimentally accessible from electronics side by means of high field electron spin resonance (ESR) measurements. ESR technique uses fixed frequency radiation source and magnetic field sweep to shift electron spin energy levels through the narrow radiation band while measuring the losses. Although ESR radiation sources can reach up few THz in frequency, the technique limits the detection to resonances with magnetic field dependent frequencies. In addition, information about absorption intensities and polarization dependence is not easily attainable. The advantage of optics experiment is the ability to measure in a broad and continuous spectral region, which enables to record dependence on polarization and temperature independently from magnetic field and makes absolute measurements of absorption coefficient for magnetic

and phononic modes possible. However, detection of transmitted radiation through the sample in the terahertz range is not straightforward. The main reason for this is the low contrast of the light source brightness compared to the background that reduces signal to noise ratio.

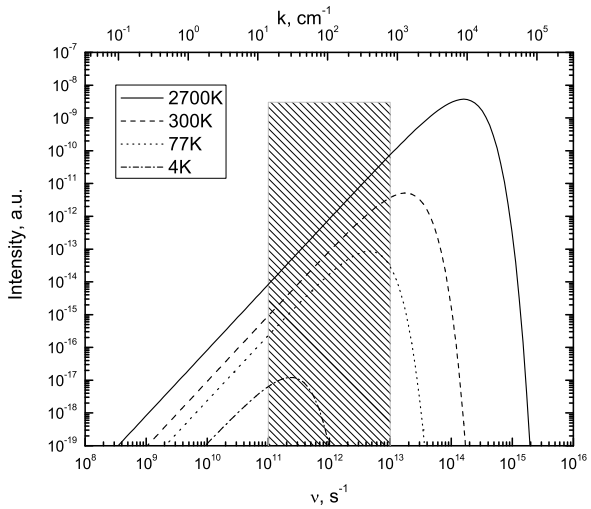

Figure 3.1: Blackbody radiation curves for typical lamp temperature (2700K), ambient temperature (300K), liquid nitrogen temperature (77K), liquid helium temperature (4K). Shaded area shows the terahertz range of electromagnetic radiation (0.1 - 10 THz)

One can see from Fig. 3.1 that while a typical light source at 2700 K is more than 10 orders of magnitude brighter than objects at ambient temperature in near infrared frequency range, the difference reduces to just 1 order of magnitude at 1 THz. Only at liquid helium temperatures will the background radiation be considerably suppressed. Additionally, use of metallic components at room temperature parts of the spectrometer such as mirrors and lightpipes is very useful because their emissivity reduces from blackbody by several orders of magnitude. Nevertheless contrast remains low and precise detection is a challenge.

The layout of the TeslaFIR spectrometer is shown on Fig. 3.2. Far-infrared light is produced by a mercury arc lamp. Most of the energy of the lamp goes to producing UV radiation, but we use the hot quartz housing of the lamp as infrared source and filter out the rest. Below about 1 THz the quartz housing becomes transparent and the hot plasma becomes the

main source of radiation. Unfortunately the density of the plasma is low and the overall gain in intensity is not too large. The light travels through a Martin-Puplett type interferometer, from which the modulated beam is focused into the cryostat light pipe. Traveling down the light encounters a stepper motor controlled polarizer, then a sample on a rotatable wheel and a wire-grid beamsplitter that splits the beam into two different light pipes. Two beams exiting the sample chamber will pass through filters at 4K and enter the detector chamber which houses two sensitive bolometers at 0.3 K. The bolometer signals are amplified then digitized by ADC computer board. This setup makes measurements in the range 2-250 cm^{-1} (0.06 - 7.5 THz) maximum apodized resolution of 0.12 cm^{-1} possible. Tunable experimental parameters include temperature, 2K to 200 K, polarization of the incident light and magnetic field from 0 to 12 T. Measurements are possible in Faraday and Voigt configurations. Additionally, reflectivity can be measured with a different sample probe head.

In the following sections the main components of the spectrometer are described in more detail.

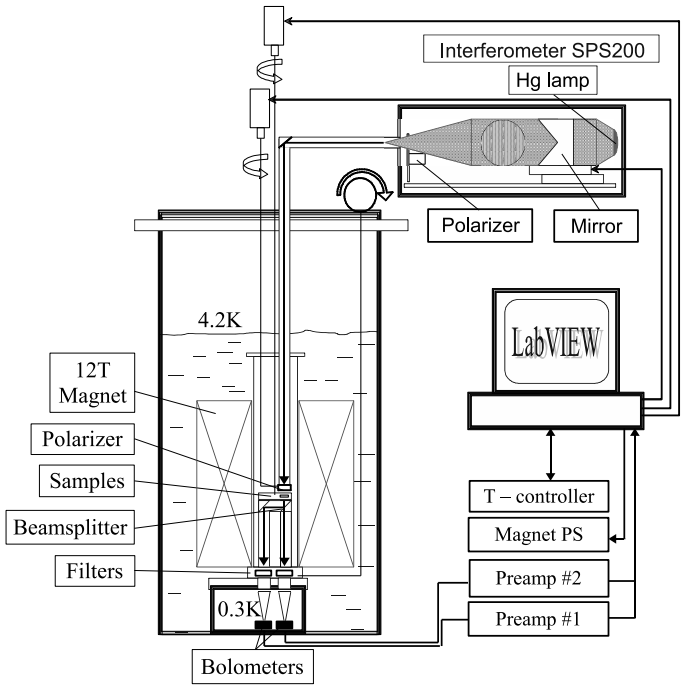

Figure 3.2: Layout of TeslaFIR spectrometer

3.2 Michelson and Martin-Puplett interferometers

The general spectrometric method known as Fourier transform spectroscopy (FTS) in which spectra are obtained by computational analysis of the interferograms produced by two-beam interferometers is now well established and widely used in spectroscopic studies in all research fields. Several textbooks give in-depth coverage of the subject, for example Ref. [20].

A two-beam interferometer is illustrated schematically in Fig. 3.3. When the movable reflector (M_m) is progressively displaced, to give a varying path difference x, the detector records a modulated intensity $I(x)$.

For the monochromatic light with wavenumber $k = \frac{1}{\lambda}$ the output intensity of such an interferometer varies as

$$I(x) = \frac{1}{2} I_0[1 + \cos(2\pi k x)] = \frac{1}{2} I_0[1 + \cos(\Delta)]. \tag{3.1}$$

One can see from equation 3.1 that theoretically half of the incident inten-

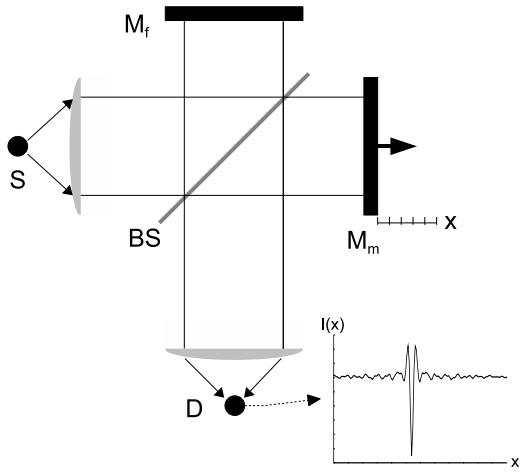

Figure 3.3: A Michelson two-beam interferometer, where S is the source, BS the beamsplitter, M_f the fixed mirror and M_m the movable reflector, and D the detector. A sample interferogram is displayed next to detector showing the variation of intensity I recorded as function of path difference x. Lenses illustrate focusing principle, but real systems use parabolic mirrors to overcome chromatic aberration and transmission losses

sity gets modulated and is spectrometrically useful. However in real systems the beamsplitter is not perfect and the useful intensity is a function of wavelength ranging from zero to half. To address the problem of inefficient beam

division a polarizing interferometer was described by D. H. Martin and E. Puplett [21]. One of possible realizations of the Martin-Puplett type interferometer is depicted in Fig. 3.4. Specific advantage of the Martin-Puplett

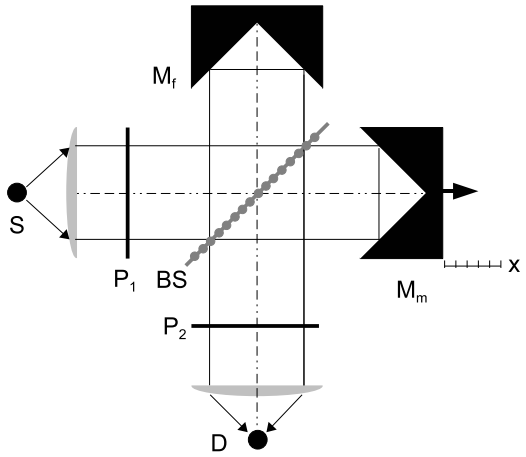

Figure 3.4: Schematic of a Martin-Puplett type interferometer used in SPS200

type interferometer is the high efficiency of a polarizing wire-grid beamsplitter over a broad and continuous range of spectral frequencies. A wire grid efficiently reflects the plane of polarization with electric field along the wires because the currents induced by the incident beam flow as they would in a continuous metal sheet. For the orthogonal plane of polarization the grid behaves more as a thin dielectric film and transmits well. This case holds for wavelengths λ that are greater than wire spacing d, see Fig. 3.5.

The linearly polarized light from polarizer P_1 (polarized along $\mathbf{p}$) incident on polarizing beamsplitter, that is rotated by 45 degrees, gets divided into two orthogonal components,

$$E_i = a\mathbf{p}\cos(\omega t) = \frac{a}{\sqrt{2}}[\mathbf{n}\cos(\omega t) + \mathbf{t}\cos(\omega t)], \tag{3.2}$$

where $\mathbf{n}$ or $\mathbf{t}$ are the unit vectors along and transverse to plane of polarization of the beamsplitter. Roof mirrors, with the roof edge parallel to $\mathbf{n}$ or $\mathbf{t}$, rotate the polarization of incident beams by 90 degrees and the beamsplitter changes from transmitting to reflecting and vice versa allowing near lossless recombination. Light leaving the beamsplitter after recombination is elliptically polarized, because of different phaseshifts Δ_a and Δ_b, containing all polarizations from linear to circular and linear (rotated 90°) again,

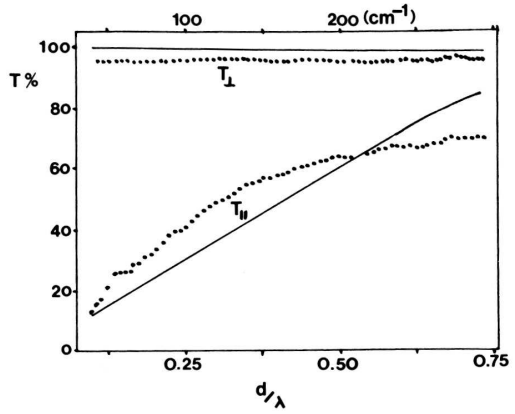

Figure 3.5: Wire grid beamsplitter transmittance for light polarized parallel and perpendicular to wire grid as a function of wire spacing (d) to wavelength (λ) ratio. Solid lines are theoretical values and dots show measured data for wire grid with d=25 μm. Wire spacing is five times the wire diameter [22]

depending on wavelength.

$$E_j = \frac{a}{\sqrt{2}}[\mathbf{n}\cos(\omega t + \Delta_a) + \mathbf{t}\cos(\omega t + \Delta_b)]. \tag{3.3}$$

Light leaving polarizer P_2 which is at an angle of 45 degrees with respect to the beamsplitter has

$$E_0 = E_j \cdot \mathbf{p} = \frac{a}{2}[\mathbf{n}\cos(\omega t + \Delta_a) + \mathbf{t}\cos(\omega t + \Delta_b)], \tag{3.4}$$

since $\mathbf{p}\cdot\mathbf{n} = \mathbf{p}\cdot\mathbf{t} = 1/\sqrt{2}$. After substitution $\Delta = \Delta_a - \Delta_b$ and $\bar{\Delta} = 1/2(\Delta_a + \Delta_b)$ and using trigonometric identities we get

$$|E_0| = a\cos(\omega t + \bar{\Delta})\cdot\cos(\Delta/2). \tag{3.5}$$

The emergent intensity from spectrometer is

$$|I_{0\|}| = |E_0|^2 = \frac{a^2}{2}\cos^2(\frac{\Delta}{2}) = \frac{a^2}{4}(1+\cos(\Delta)) = \frac{I_0}{2}(1+\cos(\Delta)). \tag{3.6}$$

If the axis of P_2 is 90 degrees to P_1 instead of parallel, then instead 3.4 we get

$$E_0 = E_j \cdot \mathbf{p}', \tag{3.7}$$

where $\mathbf{p} \cdot \mathbf{p}' = 0$ and the intensity is

$$|I_{0\perp}| = \frac{a^2}{4}(1 - \cos(\Delta)) = \frac{I_{0t}}{2}(1 - \cos(\Delta)). \tag{3.8}$$

Advantages that can be realized with polarizing interferometer are

a) an increased spectral range with a single beamsplitter,

b) the possibility to make refractive index measurements at millimeter wavelengths,

c) background interferogram recording together with sample interferogram by collecting the reflected beam from polarizer P_2,

d) elimination of a high mean level of interferogram by alternating relative orientation of polarizers P_1 and P_2 or by using two detectors in opposition - one receiving transmitted and the other the reflected beam. For a monochromatic source the difference of 3.6 and 3.8 is

$$I_{0\parallel} - I_{0\perp} = I_0 \cos(\Delta)), \tag{3.9}$$

which oscillates about the true zero-level.

The beamsplitter in SPS200 has photolitographically made $0.4\mu m$ thick aluminum wires which are $2\mu m$ wide and pitched $4\mu m$. A $12\mu m$ thick film of polyethylene terephthalate (Mylar) is used as substrate. The SPS200 interferometer can operate in rapid scan or in step and integrate mode. In the rapid scan mode the moving mirror is uniformly displaced and the output intensity of the interferometer varies as 3.6 or 3.8 depending on the direction of P_2. In the step and integrate mode the moving mirror is displaced by small steps and and the output polarizer is rotated at constant speed. The interferogram is collected by averaging the sinusoidally chopped signal at each interferogram point by a lock-in amplifier. Step and integrate mode utilizes Eq. 3.9. The SPS200 unit can also be converted to Michelson mode for measurements in a higher frequency range by substituting the beamsplitter for a non-polarizing one and removing the input and output polarizers.

3.3 Cryogenics of the TeslaFIR spectrometer

The physical parameters of the cryostat are given by the magnet that is available. The source of magnetic field in the current study was a superconducting Oxford Instruments 12 T magnet with a 50 mm cold bore. The use

of maximum field (12 T) requires current of 98 A passing through the coil at the temperature 4.2 K. The design and construction of TeslaFIR spectrometer has been done prior to this thesis author's joining the research group at NICPB. Nevertheless it is instructive to give an insight to TeslaFIR's operation.

The main liquid helium (^{4}He) bath is of cylindrical shape with a diameter of 30 cm to accommodate the superconducting magnet. The main bath is surrounded by a radiation shield at liquid nitrogen temperature inside the outer vacuum can. The liquid helium volume at maximum level in the main bath is about 40 liters. During operation the liquid helium evaporation rate is quite high, $\sim$ 1 liters per hour, due to relatively short cryostat design and a large number of tubes and wires going from the 4.2 K bath to the room temperature flange at top of the cryostat. A typical far-infrared transmission or reflection experiment with TeslaFIR utilizing magnetic fields lasts for 5 days and consumes approximately 120 liters of liquid helium and about 200 liters of liquid nitrogen.

Inside the main bath below the magnet lies the detector chamber which also houses a closed cycle ^{3}He cryostat. The ^{3}He cryostat consists of four major parts a) ^{3}He gas reservoir b) 1.6 K cooler c) absorber pump d) 0.3 K pot with a cold plate, Fig. 3.6. The ^{3}He cryostat has two operating modes - condensing mode and cooling mode. In *condensing mode* the charcoal absorber pump is regenerated by heating it to 70 K and the released ^{3}He gas is liquefied by the 1.6 K cooler. Liquid ^{3}He at 1.6 K drops into the 0.3 K pot. The condensing process takes approximately 1 hour and additional hour is needed for the absorber to cool down and pump ^{3}He down to 0.3 K. In *cooling mode* the absorber heater is off and the cold absorber pumps on the 0.3 K reservoir reducing the vapor pressure and consequently lowering the temperature to 0.3 K. Cooling mode is sustainable for 14 hours after which all liquid ^{3}He has vaporized and pumped into the absorber. Condensing is required to restart cooling mode.

The cryogenic cycle of an experiment begins by precooling the main bath along with the magnet with liquid nitrogen. Next the radiation shield is cooled down to liquid nitrogen boiling temperature (77 K). Since the mass of the magnet with the cryostat is large, precooling takes several hours and normally the operator waits for 12 hours for the system to reach thermal equilibrium. Next, liquid nitrogen is blown out from the main bath using helium gas and the main bath is cleaned from nitrogen gas by pumping and venting with helium gas few times. Liquid helium is transfered into the main bath. The first portion of liquid helium ($\sim$ 30 l) is transfered very slowly, within $\sim$ 2.5 hours, to let the cold helium gas cool the magnet and

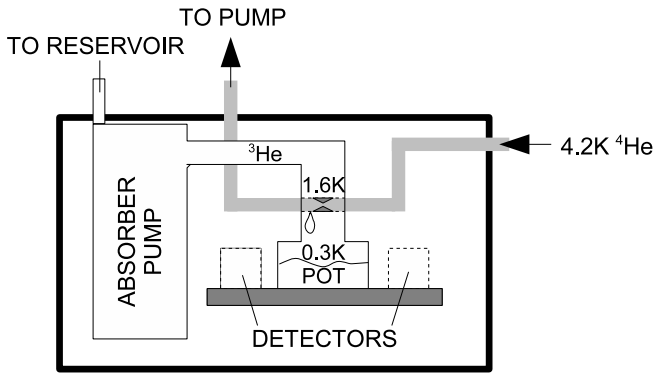

Figure 3.6: ^{3}He cryostat diagram

the rest of the main bath. Once the magnet has reached 4.2 K, the rest of liquid helium is added at normal speed - within few minutes. When the liquid helium level is above the 1.6 K cooler intake capillary, the 1.6 K cooler pump is turned on and ^{3}He cryostat is switched to condensing mode. After condensing the system is ready for measurement.

All experimental parameters, such as temperature, polarization, magnetic field, sample position, are computer controlled and lengthy automated experiments can be programmed. A conventional way of running TeslaFIR means that automated measurement runs during night- and daytime. At mornings and evenings the cryogenic fluid reservoirs are refilled and ^{3}He condensed. Such a schedule results up to 20 hours of useful experiment time within a day.

3.4 Bolometric detection

Bolometers are devices that respond to heating produced by absorbed radiation. Bolometric detectors have three main parts: an absorbing surface, a thermometer and a thermal link to heat sink, see Fig. 3.7. The design of these elements depends on the wavelength range over which the bolometer is to be operated, the background infrared power and the temperature of the heat sink. Bolometers have had extensive use because of their response throughout the infrared spectrum and their high absorptive efficiency (typically from 0.5 to 1). In order to get maximum sensitivity bolometers are typically cooled to very low temperatures. The TeslaFIR spectrometer has two 0.3 K bolometers that are cooled by pumping on liquid ^{3}He.

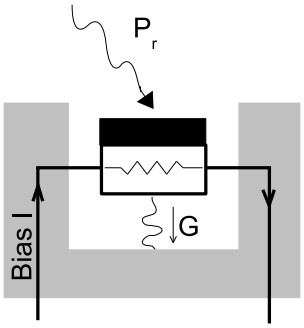

Figure 3.7: Bolometer construction. Power dissipated at bolometer by bias current I and absorbed radiative power P_r are balanced by thermal conductivity G to heat bath

The temperature of a bolometer and accordingly its sensitivity depends on several factors.

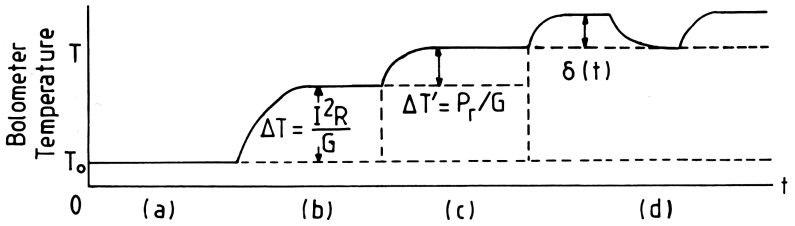

Figure 3.8: Bolometer temperature under different heat loads: a) base temperature b) bias current Joule heat c) background radiation heat d) operation with modulated radiation [23]

The time dependent heat balance equation that must be satisfied is:

$$I^2R(t) + P_r + q(t) - G(T - T_0) - G_e\delta(t) = C_p\delta(t), \tag{3.10}$$

where $q(t) = q_0(1 - e^{i\omega t})$ is the modulated radiation from the interferometer which causes temperature oscillations $\delta(t) = \delta_0(\omega)(1 - e^{i\omega t})$; C_p is bolometer heat capacity, I is bias current, G is heat conductivity, P_r is background radiation power and $G_e = dP_r/dT$ is the effective thermal conductance, which is the reciprocal of the temperature change caused by unit change in radiative power load.

By taking account only the time dependent part of 3.10, we get the

following equation for the modulated signal power

$$q(t) = G_e\delta(t) + C_p\delta(t). \tag{3.11}$$

The solution to this apart from phase lag is

$$\delta_0(\omega) = \frac{q_0}{G_e}\sqrt{1+\omega^2\tau_e^2}, \tag{3.12}$$

where the effective response time constant τ_e is given by

$$\tau_e \equiv \frac{C_p}{G_e}. \tag{3.13}$$

The ac voltage amplitude on the bolometer produced by the modulated power (3.12), is

$$V_s = \alpha IR\delta_0(\omega) = \frac{q_0\alpha IR}{G_e}\sqrt{1+\omega^2\tau_e^2}, \tag{3.14}$$

where $\alpha \equiv (1/R)dR/dT$ is the temperature coefficient of resistance. Looking at Eq. 3.14 one is tempted to increase the bolometer signal by

i) increasing the temperature change by absorbed radiation by decreasing G_e

ii) further amplification of the output voltage

iii) increasing the resistance change by increasing α and R.

The first option is limited by background radiation power and also by the relation 3.13. The latter means that increase in sensitivity is traded off for a longer time constant and consequently for longer collecting times. Options ii) and iii) can be optimized up to the limit set by thermodynamic noise processes:

a) radiation noise (fluctuations in absorbed power)

b) temperature noise (fluctuations in detector temperature)

c) Johnson noise (fluctuations in bolometer resistance).

A deeper insight into bolometer noise processes can be found in textbooks, e.g. [23]. In summary, in low background radiation conditions and where

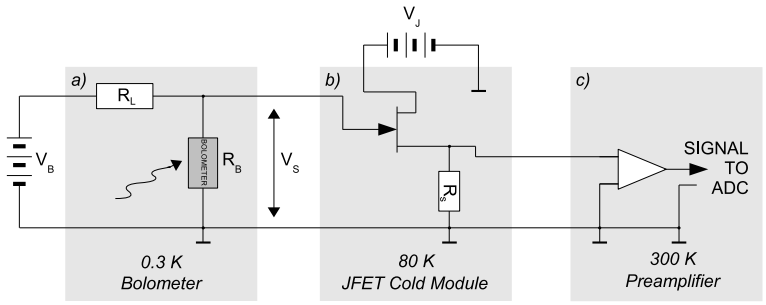

Figure 3.9: Electrical circuit for bolometer signal detection. a) Typical wiring for grounded bolometer - load resistor $R_L = 40M\Omega$ limits bias current from source V_B; voltage drop on bolometer $R_B \approx 600M\Omega$ gives signal voltage V_S. b) JFET cold module to change high ohmic output of bolometer to low ohmic input for preamplifier. Voltage drop on resistor $R_S = 10k\Omega$ is controlled by V_S on JFET gate c) preamplifier with gain 1000

Johnson and temperature noise are approximately equal the resulting noise equivalent power (NEP) in units $W/\sqrt{(Hz)}$ is given by

$$(NEP)_{J+T} \approx 10^{-11} T \sqrt{\frac{C_p}{\tau_e}}. \tag{3.15}$$

It follows that the detection limit imposed by internal processes depends only on parameters T, C_p, τ_e.

An overview of the bolometer electrical circuit implemented in TeslaFIR is given in Fig. 3.9.

The TeslaFIR setup uses grounded bolometers which is not an ideal case due to pickup of 50 Hz noise. Recent experience has shown that pickup of this noise can be avoided almost completely with a floating bolometer and good wiring. Figure 3.10 shows measured bolometer noise spectra in millivolts (with the preamplifier gain set to 1000) and the same data has been recalculated to NEP using bolometer specifications. The noise amplitude in the region where the signal is transformed (typically between 10 to 40 Hz) is about $20\,\mathrm{nV}/\sqrt{Hz}$ with only the preamplifier and $35\,\mathrm{nV}/\sqrt{Hz}$ with cold bolometer.

One can see in Fig. 3.10 that the NEP value given by the manufacturer (NEP $\approx 7 \cdot 10^{-16} W/\sqrt{Hz}$) corresponds to the measured value around 30 Hz.

Knowledge about the bolometer time constant is vital for successful experiments. We have determined that our IRLabs 0.3 K bolometers have a high frequency cutoff at 38 Hz. In practice this means, that the interferometer mirror displacement speed should to be such, that the useful signal at

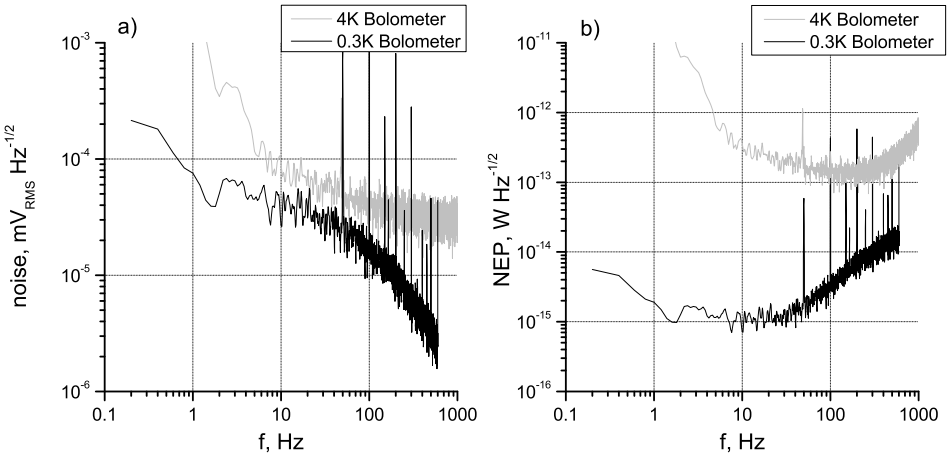

Figure 3.10: Measured noise (a) and noise equivalent power (b) for a 0.3 K and a 4 K IRLabs bolometers

the high cutoff (shortest wavelength) gets modulated with frequency below 38 Hz. For a signal at $k = 100\,\mathrm{cm}^{-1}$ and cutoff frequency $\nu = 38\,\mathrm{Hz}$ the mirror speed should be less than $v = 1/4 \cdot k^{-1} \cdot \nu = 0.08\,\mathrm{cm/s}$, which is a relatively slow speed. The factor 1/4 is introduced because the path difference gets modulated two times faster than the mirror speed and additional factor two accounts for the sampling density according to Nyquist criteria. Consequently, a single scan time at maximum resolution, which corresponds to 5 cm travel of the movable mirror in SPS200, results to more than 60 seconds. The overall averaging time for a single spectrum, with relative standard deviation less than 10^{-3}, can result up to half an hour.

In conclusion, collecting data with 0.3 K bolometers is time consuming, but worth while when looking for very small signals.

Chapter 4

Results and discussion

4.1 Overview of $Sr_{14}Cu_{24}O_{41}$

The key structural elements in all high-T_c superconductors are the CuO_2 planes, which makes the study of spin and charge dynamics in low dimensional copper oxide materials most attractive. The search for high-T_c superconductor materials led to a new structure type [24, 25] represented by $Sr_{14}Cu_{24}O_{41}$ containing both one-dimensional CuO_2 spin chains and two-dimensional Cu_2O_3 spin ladders, Fig. 4.1. The planar chains and ladders in this compound extend in the c axis direction and are alternately stacked along the b axis, separated by layers of Sr. The chain and ladder spin subsystems in $Sr_{14}Cu_{24}O_{41}$ interact weakly and are structurally incommensurate although the lattice constants in c direction satisfy an approximate relation $10\,c_{\mathrm{chain}} \approx 7\,c_{\mathrm{ladder}}$. The conductivity in $Sr_{14}Cu_{24}O_{41}$ is associated with the charge dynamics in the ladder layers. Sr substitution for Ca and external pressure leads to hole transfer from the chains to the ladders and to the occurrence of superconductivity in $Sr_{0.4}Ca_{13.6}Cu_{24}O_{41}$ with $T_c = 12\,\mathrm{K}$ at 3 GPa [26]. For a comprehensive overview on the charge and spin dynamics in this class of materials the reader is directed to Ref. [27]. Pure $Sr_{14}Cu_{24}O_{41}$ is a self-doped compound containing six holes per unit cell. A chain hole occupies oxygen $2p$ orbitals surrounding a central Cu spin and forms a Zhang-Rice (ZR) singlet[28] (-0-), rendering about 6 out of 10 Cu sites nonmagnetic. Spin dimers, two Cu^{2+} spins bridged by a ZR singlet (-↑-0-↓-) [29, 30, 31], are in the singlet state. Inelastic neutron scattering [32, 33, 34], high energy X-ray diffraction [35] and NMR[31] measurements have indicated that dimers organize with a periodicity of 5 chain units and are separated by two ZR singlets (-↑-0-↓-0-0-), see Fig. 4.2.

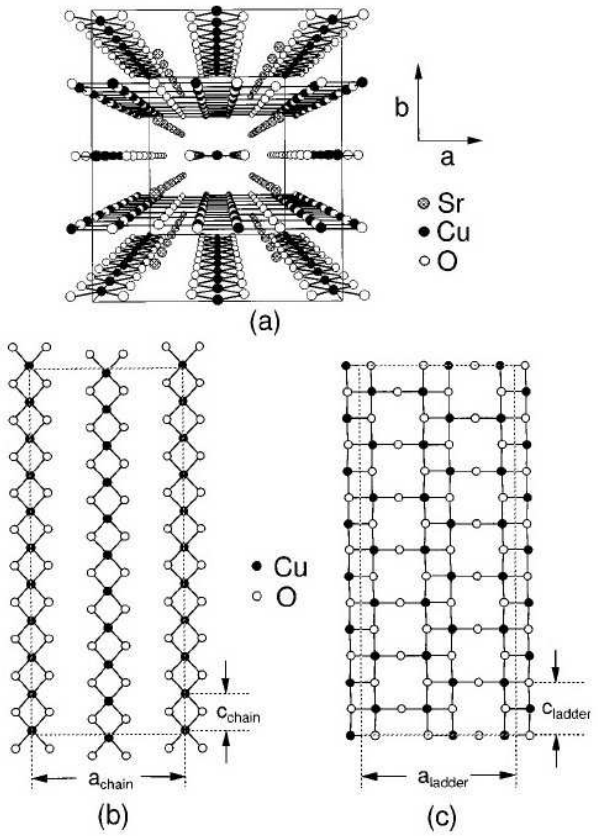

Figure 4.1: The crystal structure of $Sr_{14}Cu_{24}O_{41}$: a) alternating chain and ladder layers, b) CuO_2 chain layer structure, c) Cu_2O_3 ladder layer structure

Recent revised structural studies indicate extensive O atom position modulation out of the chain planes in $Sr_{14}Cu_{24}O_{41}$[36, 37, 38, 39, 40] and $Sr_{0.4}Ca_{13.6}Cu_{24}O_{41}$ [41, 42]. This modulation causes variations in the super-exchange between Cu atoms along the chain [43, 44]. In addition, displaced O atoms mediate the hole transfer between chains and ladders [41, 42]. It is estimated from bond-valence sum calculations, X-ray absorption spectroscopy, magnetization and optical conductivity measurements[39, 45, 30, 46, 47, 48] that 1-4% of the self-doped holes reside in the ladders in undoped $Sr_{14}Cu_{24}O_{41}$ at low temperature. The deficiency of holes in the chains means that the perfect alignment of dimers, separated by two ZR singlets yielding a five chain unit periodicity, cannot be satisfied. Very recently, in 2008, a resonant soft x-ray scattering (RSXS) study was published that focuses on hole ordering in $Sr_{14}Cu_{24}O_{41}$ [49] where the authors conclude that chain hole modulation has an incommensurate wave vector $L_c = 0.381$ and the charge density wave is stabilized due to chain and ladder misfit strain in contradiction with ZR singlet distribution proposed previously where $L_c = 0.5$.

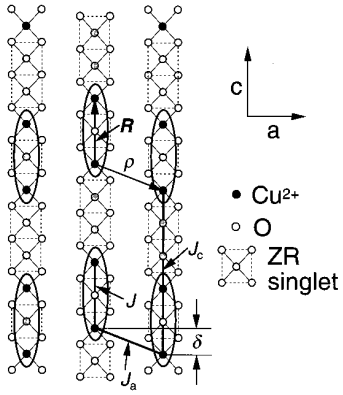

Figure 4.2: Proposed spin structure in the chains of $Sr_{14}Cu_{24}O_{41}$ [32]

There is a lack of consensus in the literature regarding spin and charge order in the chains of $Sr_{14}Cu_{24}O_{41}$ and the nature of the underlying ground state. We studied magnetic excitations using far-infrared (FIR) spectroscopy and strong magnetic fields with the aim to identify the spin states present in the chains of $Sr_{14}Cu_{24}O_{41}$.

4.2 Terahertz absorption in $Sr_{14}Cu_{24}O_{41}$

FIR transmission spectra in magnetic fields below 12T were recorded with the TeslaFIR spectrometer (Chapter 3). Spectra in fields above 12 T were measured at NHMFL in Tallahassee utilizing Bruker IFS 113v with a 18 T superconducting magnet and a 4 K silicon bolometer. Two single-crystalline samples of $Sr_{14}Cu_{24}O_{41}$ were used in the current study: a 1.1 mm thick crystal with an (ab)-plane area of 13.2 mm^2 (No. 4 in Fig. 4.3) and an (ac)-plane crystal with an area of 12.6 mm^2 and a thickness of 0.65 mm (No. 5 in Fig. 4.3). FIR transmission spectra in magnetic fields were recorded

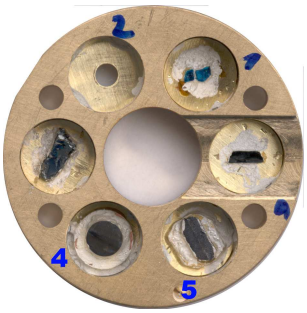

Figure 4.3: Sample wheel of the TeslaFIR spectrometer transmission probe. Positions No. 4 and 5 contain (ab)-plane and (ac)-plane $Sr_{14}Cu_{24}O_{41}$ crystals respectively

for a single sample without moving the sample wheel between field changes. Differential absorption spectra were calculated from transmitted intensity $I(B_0, \omega)$ using following formula:

$$\alpha(B_0, \omega) - \alpha(B_0^r, \omega) = -\frac{1}{d} \cdot \ln \frac{I(B_0, \omega)}{I(B_0^r, \omega)}, \tag{4.1}$$

where B_0 is the applied magnetic field, B_0^r is the reference field and d is sample thickness. Consequently, in differential absorption spectra presented here, lines belonging to reference magnetic field spectra are pointing downward, if present, and lines in fields under observation are pointing upward. Calculation of differential absorption makes detection of weak features in the spectra possible if a feature changes with the change the experimental parameter (magnetic field, temperature, polarization). For example, a transition from the singlet ground state to the triplet state $|T_0>$ is usually not observable in a differential absorption spectrum, because the energy of $|T_0>$ does not depend on the magnetic field. However, if the transition

intensity or the linewidth changes with magnetic field, then transition from $|S>$ to $|T_0>$ can be observed in differential absorption spectra.

4.2.1 Magnetic field dependence

Polarization-sensitive transmission measurements in the THz spectral region revealed an anisotropic response from the crystal (ab) plane. When the external magnetic field was applied along the c axis of the crystal (along the chains), two magnetic field dependent modes, T_1 and T_2 were found, which we assign to spin excitations in the chains of $Sr_{14}Cu_{24}O_{41}$.

Transitions to the triplet state T_1 were visible when the electric field component $\mathbf{E}_1$ of the radiation was polarized along the b axis. Observed

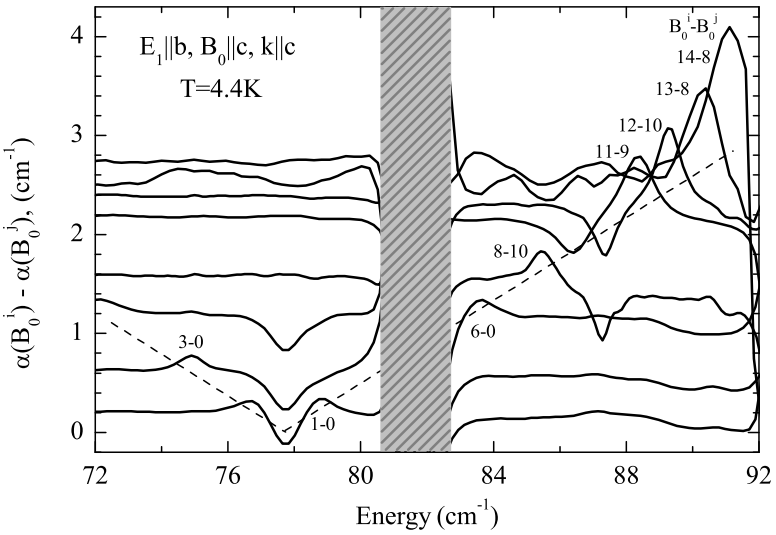

Figure 4.4: Differential absorption spectra of triplet T_1 in magnetic field applied in the c axis direction with light k vector $\mathbf{k} \parallel \mathbf{c}$ and polarization $\mathbf{E}_1 \parallel \mathbf{b}$ at 4.4 K. The spectra are shifted in the vertical direction by $0.2B_0^i$. Dashed lines are eye guides. The shaded area covers the spectral region of strong phonon absorption.

differential absorption spectra, measured in different magnetic fields at 4 K, are shown in Fig. 4.4. The triplet state has three spin sublevels, $M_S = -1, 0, +1$ what we denote as T(−), T(0), and T(+), see inset to Fig. 4.6.

The resonance frequency of the $T_1(0)$ level does not shift with field and thus escapes detection. The transition to the $T_1(-)$ sublevel loses intensity as the line shifts toward smaller energies in increasing field and gets too weak for detection in fields above 12 T. The transition to the $T_1(+)$ level gains intensity with increasing magnetic field up to the observation limit set by the strong phonon background at 92 cm^{-1} where the crystal becomes opaque to FIR radiation in $\mathbf{E}_1 \parallel \mathbf{b}$ polarization.

In $\mathbf{E}_1 \parallel \mathbf{a}$ polarization transitions to the triplet state T_2 are observed (Fig. 4.5). Transitions to the $T_2(+)$ level in fields below 2 T and to the $T_2(-)$ level are masked by strong absorption below 89 cm^{-1}. To check the light polarization and $\mathbf{B}_0$ orientation dependence, measurements on a thinner (ac)-plane crystal in Faraday and Voigt configuration were carried out, inset to Fig 4.5. In Faraday configuration, with $\mathbf{B}_0 \parallel \mathbf{b}$ and $\mathbf{E}_1 \parallel \mathbf{a}$ the triplet T_2 mode disappears from the infrared absorption spectrum. In Voigt configuration $\mathbf{B}_0 \parallel \mathbf{c}$ and $\mathbf{E}_1 \parallel \mathbf{a}$ the triplet T_2 mode is observable even in fields below 2 T. In addition, some absorption lines belonging to the $T_2(-)$ level were detected in Voigt configuration when $\mathbf{B}_0 \parallel \mathbf{c}$. However, because of strong phononic absorption below 89 cm^{-1} the intensities of $T_2(-)$ were not reliable and are not included in Fig 4.6a.

The spectral lines were fitted with a Lorentzian line shape. Line positions and intensities as a function of magnetic field are displayed in Fig. 4.6. We assume that $T_1(-)$ and $T_1(+)$ are degenerate at $B_0 = 0$ T and plot half of the measured line intensity for this field value. The same holds for the T_2 triplet.

The magnetic field dependence of the triplet line positions was fitted with the following formula

$$E_i(\pm) = \Delta_i \pm g_i \mu_B B_0, \tag{4.2}$$

where Δ_i is the singlet-triplet energy gap (line position in zero magnetic field) and g_i is the g factor for triplet T_i (solid lines in Fig. 4.6b). The fit yielded similar g factors for both triplets, $g_{1c} = 2.049 \pm 0.012$, $g_{2c} = 2.044 \pm 0.014$ and the energy gap values were fixed to the values obtained from Lorentzian fits in 0 T spectra $\Delta_1 = 77.8\,cm^{-1}$ and $\Delta_2 = 87.7\,cm^{-1}$. Additionally we observed a strong paramagnetic signal at 4 K with $g_c = 2.038 \pm 0.016$, see Fig. 4.11 and Section 4.2.4 for further discussion.

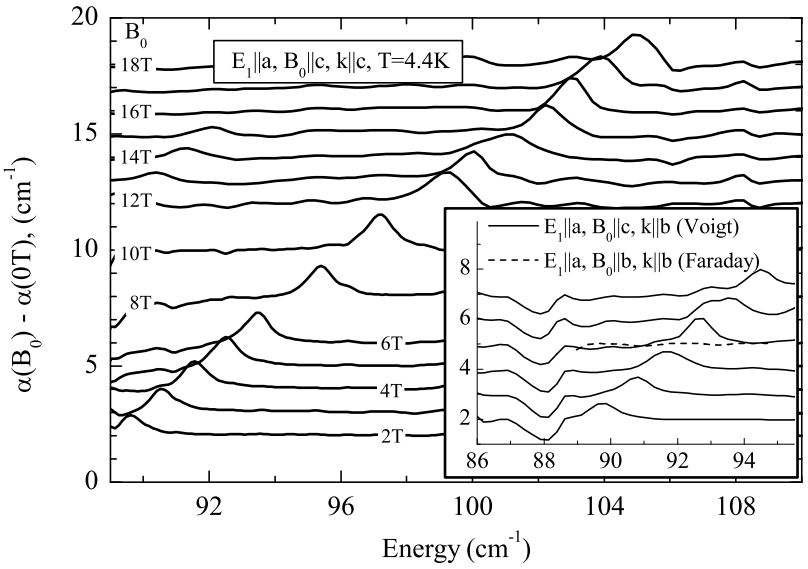

Figure 4.5: Differential absorption spectra of triplet T_2 in magnetic field applied in the c axis direction with light k vector $\mathbf{k} \parallel \mathbf{c}$ and polarization $\mathbf{E}_1 \parallel \mathbf{a}$ at 4.4 K measured using the (ab)-plane crystal. The spectra are offset in vertical direction by the magnetic field value B_0. The inset shows differential absorption spectra for the (ac)-plane crystal in Faraday (dashed line) and Voigt (solid line) configurations. Triplet $T_2(+)$ is not infrared-active when $\mathbf{B}_0 \parallel \mathbf{b}$ as shown by the dashed line for an arbitrary chosen $B_0 = 5$ T.

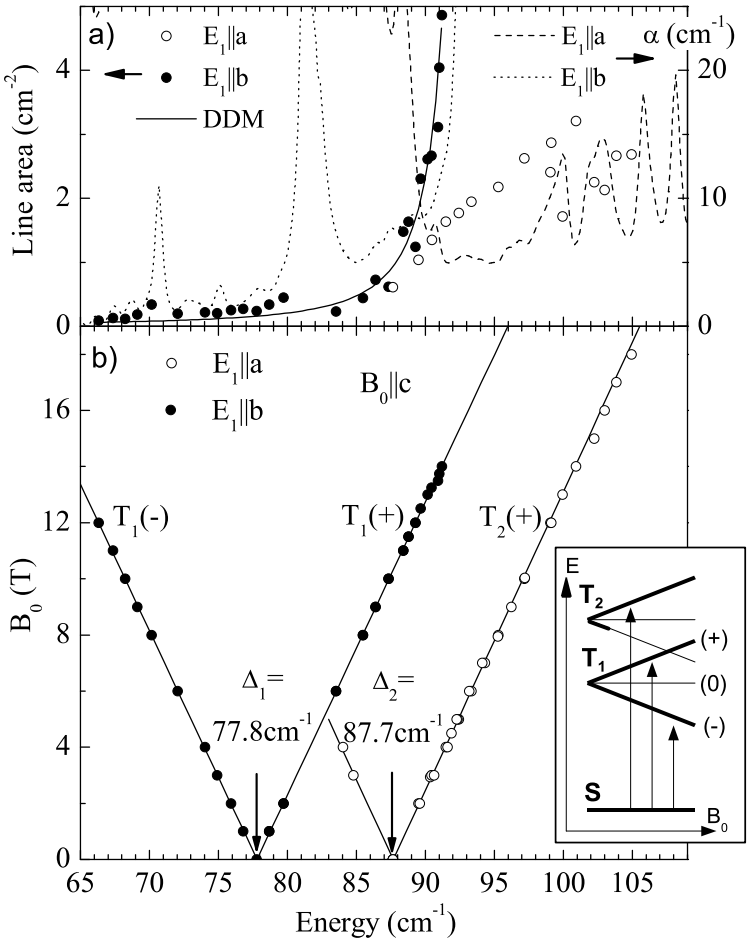

Figure 4.6: Magnetic field $\mathbf{B_0} \parallel \mathbf{c}$ dependence of line areas and positions. a) Line areas of triplet modes (left axis) and FIR absorption spectra (right axis) at temperature 4.4 K for $\mathbf{E}_1 \parallel \mathbf{a}$ and $\mathbf{E}_1 \parallel \mathbf{b}$ polarizations. The solid line is the dynamic Dzyaloshinskii-Moriya interaction model fit of the T_1 absorption line area. b) T_1 and T_2 line positions as a function of magnetic field B_0. The inset shows schematically the observed transitions.

4.2.2 Temperature dependence

The temperature dependence of the two singlet-triplet resonances was measured as the difference of 0 T and 10 T spectra at temperatures from 4 K to 60 K. Fig. 4.7b shows absorption lines in 0 T field for the triplet T_1. $Sr_{14}Cu_{24}O_{41}$ is not transparent in $\mathbf{E}_1 \parallel \mathbf{a}$ polarization at the zero field line position frequency of T_2 and therefore we analyze the T dependence of this triplet level in 10 T field, Fig 4.7a. Although both lines broaden and lose intensity as temperature increases, the T dependence of line positions is different. The T_1 triplet resonance shifts notably toward higher energies whereas the energy of T_2 remains unchanged, see Fig. 4.9a.

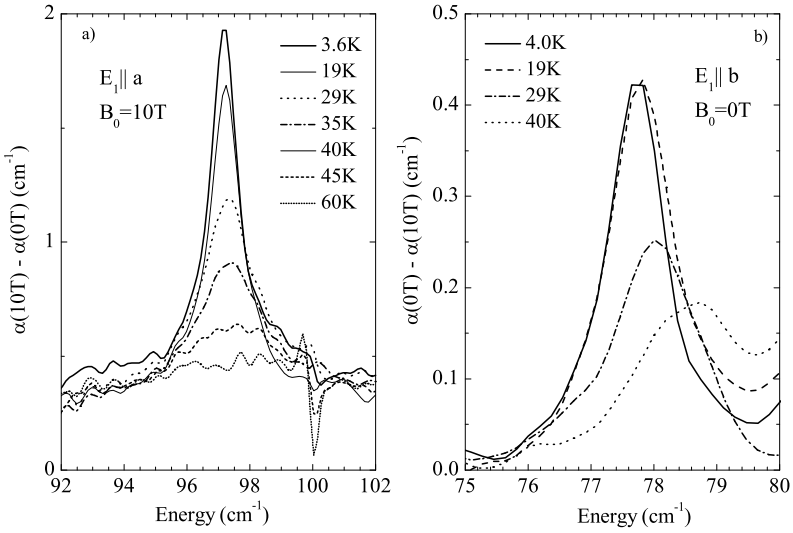

Figure 4.7: Temperature dependence of triplet modes: a) $T_2(+)$ in 10 T field, b) T_1 in zero magnetic field

The dispersion curves of the two magnetic excitations, acoustic and optic, with respective energies 11 meV and 12.5 meV at k points equivalent to $\mathbf{k} = 0$ have been measured by inelastic neutron scattering (INS) spectroscopy [32, 33]. A good fit of the experimental data was obtained by the simplest model for a weakly coupled dimer system. The dispersion in the c axis direction follows a cosine form with the periodicity of 0.2 reciprocal lattice units (Fig. 4.8). The temperature dependence of INS data demon-

strated that with rising temperature the dispersion curves flatten out since the inter-dimer couplings become negligible due to thermal fluctuations and the dimers behave more like isolated dimers. As the dispersion curves flatten, the acoustic mode at k space points near the Brillouin zone edge $(H, K, 0.1)$ shifts toward higher energies while the triplet state energy at $(H, K, 0)$ does not change (reciprocal lattice units H and K are integers in our discussion). In contrast to these considerations, the energy of the optic branch at $(H, K, 0.1)$ in the momentum space displays no temperature dependence while the energy near $(H, K, 0)$ lowers notably with temperature.

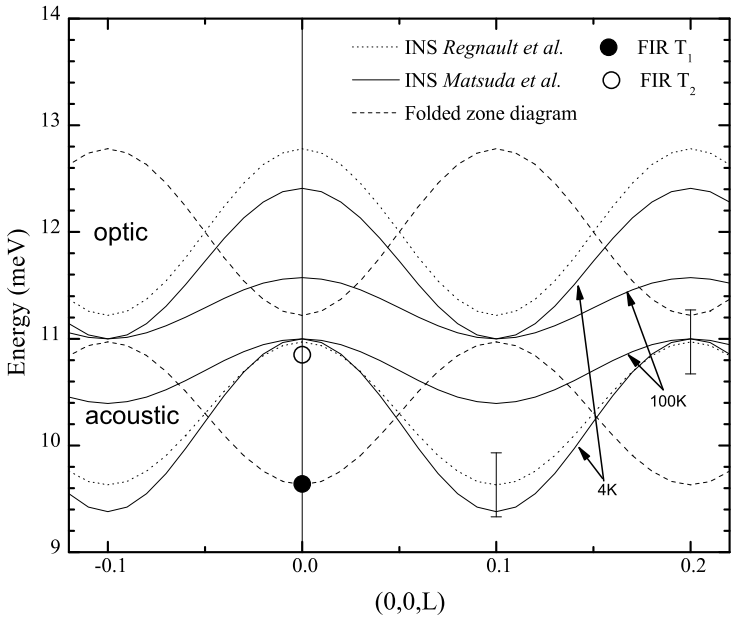

Figure 4.8: Dispersion curves of the magnetic excitations in the chains (Refs. [32] and [33]) and the observed triplet modes from FIR. The dashed lines are extra dispersion curves, derived from data of *Regnault et al.*[33], after doubling the unit cell in the c axis direction. The INS energy resolution is shown by error bars; FIR transitions have linewidth less than the size of experimental points on the graph.

It follows from the momentum conservation that an absorbed infrared photon creates a triplet excitation with $\mathbf{k}$ equal to photons momentum, $\mathbf{k} \approx 0$, which is in the center of Brillouin zone. INS data[32, 33] shows no excitation at 9.65 meV in the center of the Brillouin zone that would

correspond to the triplet excitation T_1, seen in FIR spectra. A possible explanation to overcome this discrepancy with INS results is to consider zone folding. Doubling of the unit cell size in the c axis direction is consistent with FIR data since then the energy of the back folded acoustic branch at $(H, K, 0.1)$ point would coincide with the energy of T_1, see Fig.4.8. Indeed, the triplet mode T_1 has a similar temperature dependence of its energy as the acoustic mode at k points equivalent (any integer value of H and K) to $(H, K, 0.1)$. We conclude that a magnetic unit cell of $10\, c_{\text{chain}}$ is compatible with our results.

The triplet T_2 has an energy similar to the acoustic mode at (H,K,0). In the folded zone picture the (H,K,0.1) point moves to the center of the Brillouin zone and is infrared-active as well. Due to the experimental uncertainty of the INS experiment (~ 0.5 meV) and a similar temperature dependence of acoustic and optic modes at this energy (≈ 11 meV) we cannot determine exactly whether the triplet T_2 belongs to the acoustic or the zone folded optic branch of excitations, seen by INS. However, the k points equivalent to $(H, K, 0)$ points of the acoustic excitation are closer in the energy scale to the triplet level T_2, seen by FIR. Consequently we assign triplet T_2 to the chain acoustic excitation branch (in INS notation) at $\mathbf{k} = 0$ point in the momentum space and refine the spin gap value for this point to 10.86 meV ($87.7\,\text{cm}^{-1}$).

The T dependence of intensity of the observed FIR transitions, I, is proportional to the population difference of singlet and triplet levels if we assume that the transition matrix element is independent of temperature. Following the Boltzmann distribution we get $I \sim [1 - \exp(-\Delta/kT)]/[1 + 3N \exp(-\Delta/k_B T)]$, where N is the number of triplet states, each 3-fold degenerate, and Δ is the singlet-triplet energy gap; we used an averaged value $\Delta = 11$ meV for all triplets. The solid line (Fig. 4.9b) indicates the calculated normalized transition intensity for a system with two triplet states and the dashed line for four triplet states in the new folded zone structure. Theoretical curves qualitatively explain the decrease in intensity. As the lines broaden with temperature, the determination of line areas becomes less accurate and thus T dependence of intensity cannot distinguish whether two or four triplet states exist.

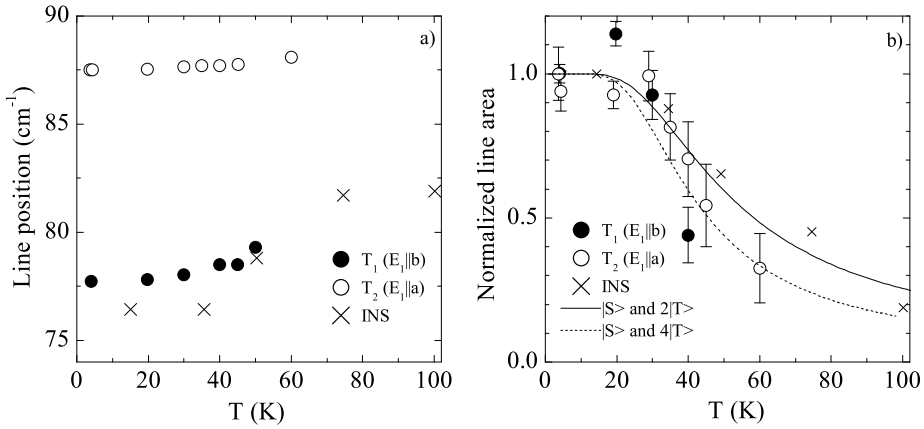

Figure 4.9: Temperature dependence of triplet modes: a) line positions, b) observed normalized transition intensities; calculated singlet-triplet transition line area assuming 2 triplets (solid line) or 4 triplets in the folded zone structure (dashed line). The INS data, Ref. [32], is at $\mathbf{k} = (2, 0, -0.1)$.

4.2.3 Linewidths

Linewidths of both triplets are 1 ± 0.2 cm^{-1} and do not depend on the strength of the magnetic field. Instrument resolution of 0.5cm^{-1} was used, which is significantly better than the observed triplet linewidths. At 20 K the linewidths of the singlet to triplet transitions seen in FIR are about 200 times larger than the ESR transitions [47]. The ESR observations report linewidth of 50 Oe at 20 K, which is equal to 5×10^{-3} T $\approx 0.005\,\mathrm{cm}^{-1}$, since $g\mu_B = 2 \cdot 0.467\mathrm{cm}^{-1}/\mathrm{T}$. The difference between the two experimental probes is that FIR transitions are across the spin gap while ESR transitions are within the triplet state. It is natural to assume that it is the distribution of spin gaps what makes the 200-fold increase of triplet linewidth in FIR spectroscopy compared to ESR linewidth. Theoretical calculations [44] have demonstrated that there is a substantial fluctuation, 8%, of intradimer exchange coupling, $\sim$ 10 meV, which contributes the most to the size of the spin gap. Such inhomogeneous distribution should result in a Gaussian and not a Lorentzian lineshape. However, there is an inter-dimer exchange, ~ 1 meV, that reduces the effect of inhomogeneous broadening and restores the Lorentzian lineshape, an effect similar to motional narrowing.

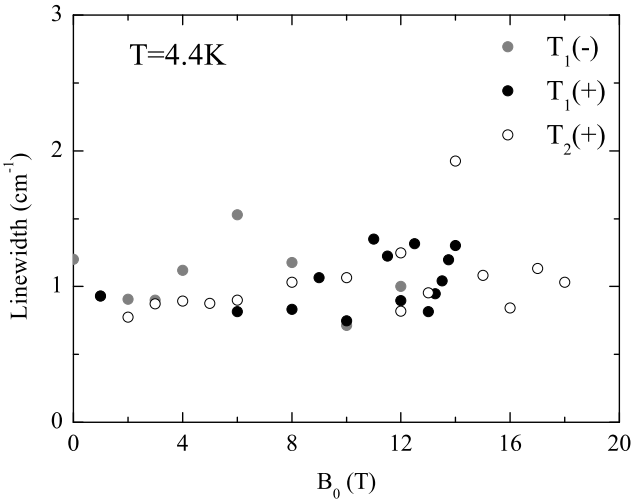

Figure 4.10: Linewidths of singlet-triplet transitions

4.2.4 Paramagnetic signal

In the FIR we observed two distinct magnetic signals at 4 K. Firstly, the transitions from the singlet ground state to triplet states T_1 and T_2, and secondly, a paramagnetic signal (Fig. 4.11). It is not expected that the para-

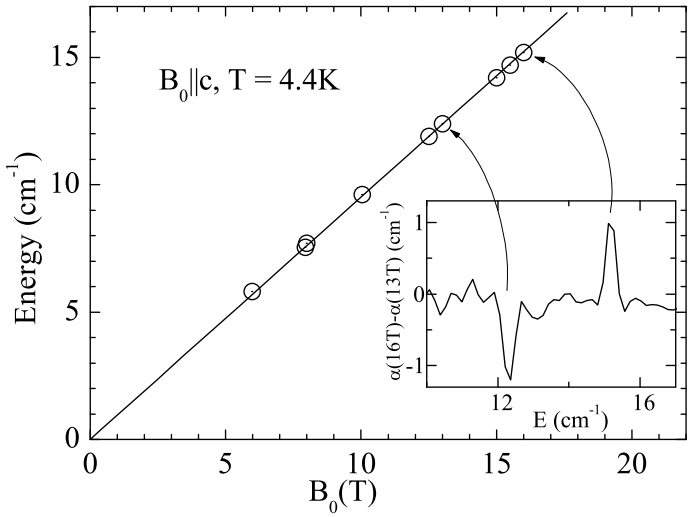

Figure 4.11: Magnetic field dependence of the paramagnetic transition energy in $\mathbf{B}_0 \parallel \mathbf{c}$ orientation. The line is a fit to the data yielding g-factor $g_c = 2.038 \pm 0.016$. The inset demonstrates the paramagnetic transition signal in differential absorption spectrum. The linewidth is resolution limited by instrument to $0.3\,\mathrm{cm}^{-1}$.

magnetic response at 4 K originates from a thermally excited triplet state in the chains due to a large spin gap, $\Delta \approx 11$ meV. There is evidence from susceptibility and ESR measurements that unpaired spins exist in $Sr_{14}Cu_{24}O_{41}$. The g factor of the paramagnetic signal $g_c = 2.038 \pm 0.016$ obtained from our experiments matches that of ESR g_c(4K)=2.038 at 4 K [48]. Above 20 K when the triplets are thermally populated, the ESR detects transitions between triplet levels $M_S = \pm 1$ and $M_S = 0$. The g factors of both triplets measured in FIR, $g_{1c} = 2.049$ and $g_{2c} = 2.044$, coincide with the averaged value g_c(20K) = 2.045 from ESR [48, 29, 47]. FIR measurements confirm directly that unpaired spins have g_c similar to the g factors of spin dimers g_{1c} and g_{2c}. Similar g_c components of the g tensor suggest a common local

environment for the triplet and the paramagnetic site magnetic moments, as was also proposed in Ref. [48]. Evidentially unpaired spins are in chains of $Sr_{14}Cu_{24}O_{41}$, instead of ladders. Unpaired Cu^{2+} spins in the chain subsystem destroy the perfect charge order with $5c_{\mathrm{chain}}$ periodicity and are in accord with the FIR active triplet T_1 which, as was discussed above, is a result of doubling of the unit cell.

Chapter 5

Selection rules of singlet to triplet excitation

This chapter is devoted to the discussion on the selection rules of the observed singlet-triplet transitions. Before discussion on the selection rules in $Sr_{14}Cu_{24}O_{41}$, selected results in α'-NaV_2O_5 and $SrCu_2(BO_3)_2$ will be presented to support the conclusions on $Sr_{14}Cu_{24}O_{41}$. For a comprehensive analysis on α'-NaV_2O_5 and $SrCu_2(BO_3)_2$ the reader should refer to the papers [2, 3].

The necessity for polarized light becomes most apparent when exploring the selection rules for absorbed radiation. The general idea behind discovering the light absorption mechanism is to use different experimental geometries while leaving the polarization constant with respect to crystal axes. In

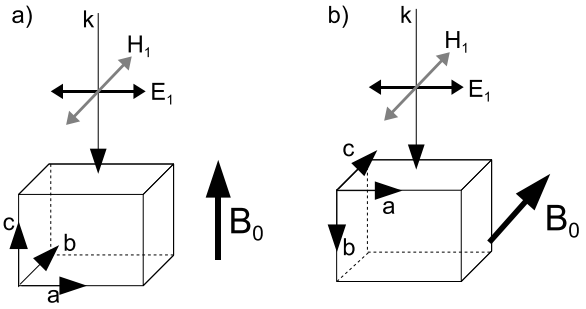

Figure 5.1: Experimental geometries for selection rules mapping: a) $\mathbf{E}_1 \parallel \mathbf{a}$ and $\mathbf{B}_0 \parallel \mathbf{c}$ in Faraday configuration b) $\mathbf{E}_1 \parallel \mathbf{a}$ and $\mathbf{B}_0 \parallel \mathbf{c}$ in Voigt configuration

Fig. 5.1 the electric field component of light remains polarized parallel to a

crystal axis, but the magnetic field component gets rotated from b to c axis when the experimental geometry is changed. If the absorption spectrum remain the same then the necessary conditions are proven. Now, if rotating the electric field polarization to a perpendicular orientation changes the absorption spectrum, then the absorption has electric dipole origin. Similarly magnetic dipole active absorption can be identified.

5.1 Selection rules in α'-NaV_2O_5

In α'-NaV_2O_5 magnetic properties arise from V^{4+} 1/2-spins that are localized on V_2O_5 ladder units in a zigzag pattern below $T_c < 34.7\,\mathrm{K}$, Fig.5.2a. We observed singlet to triplet excitation with an energy gap $8.13\,\mathrm{meV}$ ($65.4\,\mathrm{cm}^{-1}$). Using different experimental geometries we were able to conclude that the dominant light-spin coupling mechanism is of electric dipole origin. Singlet to triplet transition was the strongest when the electric field polarization of the incident light was parallel to a crystallographic axis ($\mathbf{E}_1 \parallel \mathbf{a}$). When the incident light polarization was perpendicular to the ladder planes ($\mathbf{E}_1 \parallel \mathbf{c}$) the transition was about 10 times weaker, but an enhancement of the singlet to triplet transition was observed when the applied magnetic field, either in $\mathbf{B}_0 \parallel \mathbf{a}$ or $\mathbf{B}_0 \parallel \mathbf{c}$, shifted the singlet to triplet resonance frequency to match the $68\,\mathrm{cm}^{-1}$ c-axis phonon energy, Fig. 5.3.

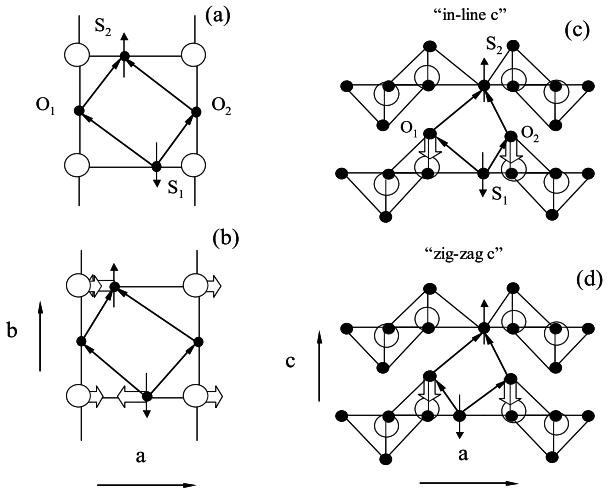

Figure 5.2: Cartoons of superexchange paths in the ab-plane (panels (a) and (b)) with one ladder shown and in the ac-plane ((c) and (d)) with two ladders shown. For illustrative purposes it is assumed that the spin is located on the rung oxygen. Oxygens are shown by filled circles and vanadium atoms by open circles. Block arrows show the displacement of atoms due to a phonon. (a) superexchange paths between two spins over on-leg oxygens within the same ladder in the zig-zag ordered phase; (b) same superexchange paths when an a-axis phonon is involved; (c) superexchange paths between two spins in the neighboring planes over apical oxygens displaced by a c-axis phonon when spins are in-line along c-axis or (d) zig-zag.

In the zigzag ordered low T phase two superexchange paths exist, one over on-leg oxygen O_1 and the other over O_2, shown in Fig.5.2a. The resultant DM vector is zero since the two DM vectors, pointing in **c**-direction, cancel each other out. The zero length of the DM vector follows from the general arguments of symmetry too as in this particular case there exists a local center of inversion located between two V-O-V rungs. In $\mathbf{E}_1 \parallel \mathbf{a}$ polarization the a-axis phonon mode at $518\,\mathrm{cm}^{-1}$ displaces on-rung oxygens along the rung (on-rung V-O-V stretching mode)[50], Fig 5.2b. Because of the phonon the two superexchange paths are not "equal" any more and the resulting DM vector points along the c-axis. The orientation of the dynamic DM vector, $\mathbf{D}_Q \parallel \mathbf{c}$, is consistent with the selection rules for the dynamic DM interaction observed experimentally. The transition to the $|\mathrm{t}_0 0\rangle$ was observed when $\mathbf{B}_0 \parallel \mathbf{D}_Q$ and the transitions to the $|\mathrm{t}_- 0\rangle$ and $|\mathrm{t}_+ 0\rangle$ states were observed when $\mathbf{B}_0 \perp \mathbf{D}_Q$, Fig. 11 in Ref. [2] .

Two superexchange arrangements along the c-axis are possible in the zigzag ordered phase, shown in Fig. 5.2c,d: in-line or zigzag. In $\mathbf{E}_1 \parallel \mathbf{c}$ polarization, in both arrangements, the displacement of the apical oxygens in the **c**-direction will create a dynamic DM along the b-axis. As one can see not only the dynamic, but also the static DM in the **b**-direction is allowed by the symmetry. According to the selection rules for the dynamic DM only the transitions to the triplet states with $m_S = 1$ and $m_S = -1$ are observed when the magnetic field is perpendicular to the dynamic DM vector $\mathbf{D}_Q \perp \mathbf{B}_0$. This condition if fulfilled when $\mathbf{D}_Q \parallel \mathbf{b}$ since the splitting of the triplet in the magnetic field is observed if $\mathbf{B}_0 \parallel \mathbf{a}$ or $\mathbf{B}_0 \parallel \mathbf{c}$, Fig. 5.3. The selection rules for the dynamic DM if $\mathbf{B}_0 \parallel \mathbf{D}_Q \parallel \mathbf{b}$ allow only transitions to the $m_S = 0$ level that does not shift with the magnetic field and we do not see it in the differential absorption spectra that are taken in different magnetic fields. In $\mathbf{E}_1 \parallel \mathbf{c}$ polarization the dynamic DM mechanism is brought in by the $68\,\mathrm{cm}^{-1}$ optically active c-axis phonon. The enhancement of the singlet-triplet absorption close to the $68\,\mathrm{cm}^{-1}$ line is present if the magnetic field is either parallel to a- or c-axis, but missing if the field is along the b-axis. In Fig. 5.3 the fit of the singlet to triplet transition intensities (Eqs. 2.31 and 2.32) to the dynamic DM absorption mechanism is shown. The input parameters are the resonance frequency of the phonon, $\omega_p = 68\,\mathrm{cm}^{-1}$, and the frequency of the singlet to triplet transition as the function of magnetic field, $\omega_{T_\pm} = \Delta \pm g\mu_B B_0$, where $\Delta = 65.4\,\mathrm{cm}^{-1}$ ($\Delta = J$ for a single dimer). We estimated the low temperature oscillator strength of the phonon from its temperature dependence presented, $\Omega_p^2 = 400\,\mathrm{cm}^{-2}$. The ratio of the singlet to triplet absorption oscillator strength Ω_{ST}^2 to the oscillator strength of the phonon, Ω_p^2, is $\Omega_{ST}^2/\Omega_p^2 \sim 0.13/400 = 3.3 \times 10^{-4}$. The only fit parameter,

the strength of the dynamic DM interaction, yielded $qD_Q = 0.13\,\mathrm{cm}^{-1}$.

In conclusion, the observed singlet to triplet transitions in α'-NaV_2O_5 are explained by the dynamic DM model. In $\mathbf{E}_1 \parallel \mathbf{a}$ polarization the selection rules are compatible with dynamic DM interaction, but the transition intensities cannot unambiguously prove that the a-axis phonon mode at $518\,\mathrm{cm}^{-1}$ is the driving force behind dynamic DM interaction in this polarization. In $\mathbf{E}_1 \parallel \mathbf{c}$ polarization the selection rules and transition intensities are in excellent accord with the dynamic DM model and the c-axis phonon mode at $68\,\mathrm{cm}^{-1}$.

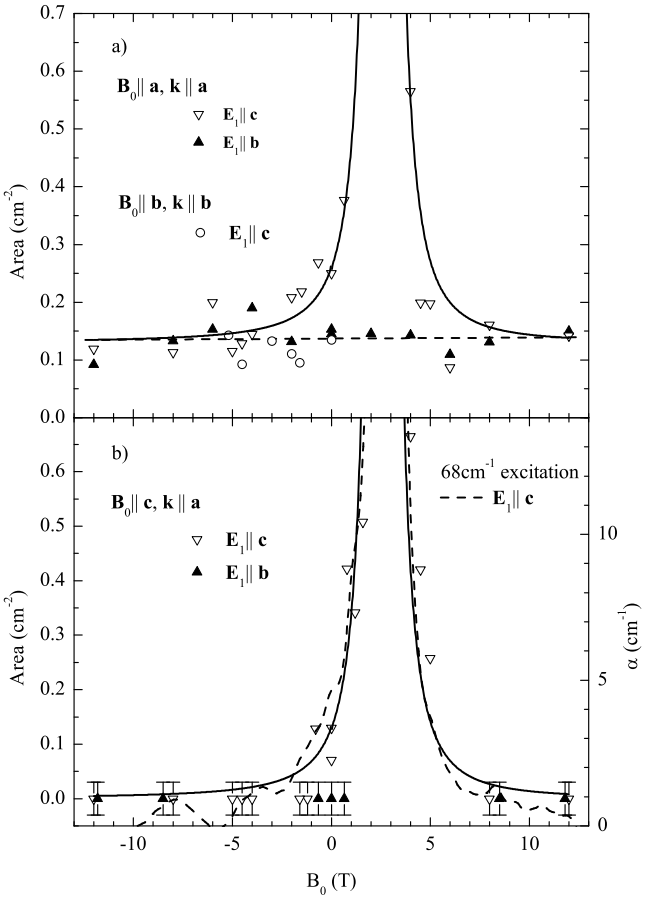

Figure 5.3: The magnetic field dependence of the singlet to triplet transition line area at 4.4 K in two polarizations, $\mathbf{E}_1 \parallel \mathbf{c}$ (empty symbols) and $\mathbf{E}_1 \parallel \mathbf{b}$ (filled triangles). The line areas are plotted in the negative field direction for the transition to the $m_S = -1$ triplet level and for the transition to $m_S = 1$ in the positive field direction. The zero field data points on the graph are one half of the measured area. (a): $\mathbf{B}_0 \parallel \mathbf{a}$ and $\mathbf{B}_0 \parallel \mathbf{b}$. (b): $\mathbf{B}_0 \parallel \mathbf{c}$. The dashed line in (a) is a guide for the eye. The dashed line in (b), units on the right axis, is the $68\,\mathrm{cm}^{-1}$ absorption line shape with the background subtracted and the energy units converted into magnetic field units using the triplet state g-factor, $g_c = 1.90$. The error bars shown only in (b) apply to data points in both panels. The solid line in (b) is a fit to the dynamical DM mechanism induced by the $68\,\mathrm{cm}^{-1}$ phonon.

5.2 Selection rules in $SrCu_2(BO_3)_2$

$SrCu_2(BO_3)_2$ is a physical realization of the Shastry-Sutherland orthogonal dimer model. Orthogonally aligned Cu^{2+} 1/2-spin dimers are in (ab) crystallographic planes, Fig 5.4a. The effective spin Hamiltonian for describing magnetic properties in $SrCu_2(BO_3)_2$ is essentially a sum of two single dimer Hamiltonians, each of which is described by Eq. 2.19. The effective two-dimer model containing an intra- and interdimer Heisenberg exchange (j_1 and , j_2) and static DM interactions for both bonds (d_1 and , d_2) is depicted in Fig. 5.4b. The analysis of selection rules is not straightforward in $SrCu_2(BO_3)_2$ due to static DM terms in the Hamiltonian which cause additional mixing of spin states. Therefore, only the selection rules of some of the dominant features will be discussed in this thesis.

As the result of the polarization sensitive measurement of FIR spectra we have identified that the main resonances in the spectra are electric dipole transitions, rather than being magnetic dipole transitions. In Fig. 5.5 differential absorption spectra at 4.4 K relative to 15 K, are displayed. The strong absorption lines at 52.3 and 53.5 cm^{-1} were identified[51] as electric dipole transitions, that are active in $\mathbf{E}_1 \parallel \mathbf{a}$ polarization. We see the same for the 43.0 cm^{-1} singlet and T_0 and T_1 triplets at 24.2 and 37.5 cm^{-1}, respectively, which are present in the spectra measured with $\mathbf{E}_1 \parallel \mathbf{a}$ regardless of $\mathbf{H}_1$ being perpendicular to the c axis or parallel to it. The lines are missing in $\mathbf{E}_1 \parallel \mathbf{c}$ polarization, instead a new line appears at 25.5 cm^{-1}, which is identified as another component of the triplet T_0.

In the case of $\mathbf{E}_1 \parallel \mathbf{c}$ polarization the optical c-axis phonon bends the Cu-O-Cu bond in the c-direction. We assume that the bending action of the phonon is the same on both dimers, Fig. 5.6. As a result the dynamic DM interaction on the dimer (1,2) is $q_c \mathbf{d}_{Q_c} \equiv \mathbf{d}_{3c} = (-d_{3c}, 0, 0)$ and on the dimer (3,4) $\mathbf{d}_{3c} = (0, d_{3c}, 0)$; the orientation of the Cartesian coordinates is the same as in Fig. 5.4 b. The calculated and the measured transition probabilities as a function of magnetic field are plotted in Fig. 4 of Ref. [3]. The overall agreement between the theory and the experiment is good.

In the case of $\mathbf{E}_1 \parallel \mathbf{a}$ polarization the optical a-axis phonon bends the Cu-O-Cu bond in the a-direction and creates a dynamic DM interaction in the c-direction, Fig. 5.6. If we choose $\mathbf{E}_1 \parallel \mathbf{a}$ the dynamic DM interaction is created on dimer (1,2), $q_a \mathbf{d}_{Q_a} \equiv \mathbf{d}_{3a} = (0, 0, d_{3a})$. In general, for an arbitrary orientation of $\mathbf{E}_1$ in the (ab) plane, both dimers will acquire a certain $\mathbf{d}_{3a}$ and for simplicity we can consider only $\mathbf{E}_1 \parallel \mathbf{a}$.

In zero magnetic field the transition to the central triplet component is observed, Fig. 5.5. When the $\mathbf{B}_0 \parallel \mathbf{c}$ field is turned on, transitions to

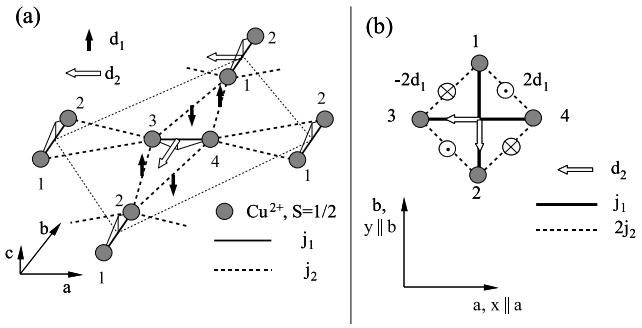

Figure 5.4: Cluster with two dimers $(1,2)$ and $(3,4)$. (a) Dimer $(3,4)$ and four nearest-neighbor dimers. The thin dashed line shows the two dimer cluster boundary. Thin solid lines show the distortion of Cu-Cu superexchange bonds due to the buckling of Cu-O-B planes. Thick solid and dashed lines are the inter- and intra-dimer superexchange constants j_1 and j_2; inter-dimer DM vectors ($\mathbf{d}_1$, solid arrow) are in the c direction and intra-dimer DM vectors ($\mathbf{d}_2$, empty arrow) in the (ab) plane along a and b axis. (b) The two dimer model after the periodic boundary condition has been applied; inter-dimer interactions have doubled.

$\mathrm{T}_0(0)$ are seen with the same intensity. This result is in agreement with the dynamic DM selection rule No. 3 (see section 2.3.3), since we have $\mathbf{B}_0 \parallel \mathbf{c} \parallel \mathbf{d}_{3a}$. When the $\mathbf{B}_0 \parallel \mathbf{a}$ field is turned on, transitions to triplet levels $\mathrm{T}_0(\pm)$ are seen, which is in agreement with dynamic DM selection rule No. 4. The experimentally observed transition intensities and the two-dimer model calculations with dynamic DM interaction coincide well in the case of $\mathbf{E}_1 \parallel \mathbf{a}$ as seen from Fig. 5 in Ref. [3].

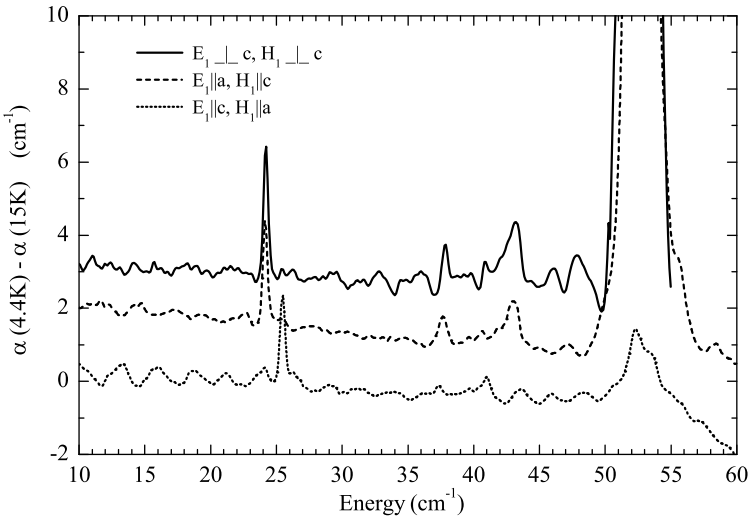

Figure 5.5: Differential absorption in $\mathbf{E}_1 \perp \mathbf{c}$ (two upper curves) and $\mathbf{E}_1 \parallel \mathbf{c}$ (lower curve) polarization. Spectra have been off-set in vertical direction.

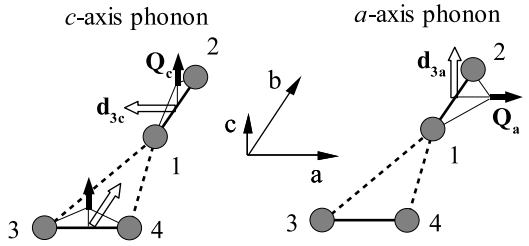

Figure 5.6: Intra-dimer dynamic DM interactions. A lattice distortion with the normal coordinate $\mathbf{Q}$ (solid arrow) creates an intra-dimer DM interaction $\mathbf{d}_3$ (empty arrow). The c-axis phonon creates a dynamic DM interaction on both dimers while the a-axis phonon affects the dimer $(1, 2)$ only.

5.3 Selection rules in $Sr_{14}Cu_{24}O_{41}$

In this section we analyze the selection rules in the primary sample in similar way as in the two previous sections in this chapter. Measuring FIR absorption spectra of the crystals in different experimental geometries has revealed that both singlet-triplet transitions in $Sr_{14}Cu_{24}O_{41}$ are electric dipole active. Indeed, with an (ab) plane crystal in Faraday geometry ($\mathbf{k} \parallel \mathbf{B}_0 \parallel c$), see Fig 5.1a, the triplet state T_1 was excited when $\mathbf{E}_1 \parallel \mathbf{b}$ or at the same time $\mathbf{H}_1 \parallel \mathbf{a}$. T_2 was excited by $\mathbf{E}_1 \parallel \mathbf{a}$ or $\mathbf{H}_1 \parallel \mathbf{b}$. Now, with an (ac) plane crystal in Voigt configuration ($\mathbf{k} \perp \mathbf{B}_0 \parallel c$), see Fig 5.1b, we observed that T_2 was again excited by $\mathbf{E}_1 \parallel \mathbf{a}$, but now with $\mathbf{H}_1 \parallel \mathbf{c}$ and the line disappeared when $\mathbf{E}_1 \parallel \mathbf{c}$ and $\mathbf{H}_1 \parallel \mathbf{a}$ without appearance of T_1 excitation.

Consequently $\mathbf{E}_1 \parallel \mathbf{b}$ polarized light excites the triplet state T_1 and $\mathbf{E}_1 \parallel \mathbf{a}$ light promotes singlets to the T_2 triplet state. In order to explain these observations we consider the dynamic Dzyaloshinskii-Moriya spin-phonon coupling mechanism that was described in Section 2.3.

There are several observations that suggest a dynamic DM interaction in spin chains of $Sr_{14}Cu_{24}O_{41}$. Firstly, the dependence on the light polarization, see also Fig. 5.7. The dynamic DM vector $\mathbf{D}_q$ is perpendicular to $\mathbf{E}_1$ and to the spin dimer axis that is the c axis in $Sr_{14}Cu_{24}O_{41}$. The triplet T_1 interacts with the electric field vector of the light $\mathbf{E}_1 \parallel \mathbf{b}$ and $\mathbf{D}_q$ is parallel to a axis for this triplet, Fig. 5.7a. The triplet T_2 interacts with the polarization $\mathbf{E}_1 \parallel \mathbf{a}$ and $\mathbf{D}_q$ is parallel to b axis, Fig. 5.7b. The selection rules are: i) if $\mathbf{B}_0 \parallel \mathbf{D}_q$ then the transition to T(0) is allowed and ii) if $\mathbf{B}_0 \perp \mathbf{D}_q$ then transitions to T($-$) and to T($+$) are allowed. One could see from Figs. 4.4 and 4.5 that the selection rule ii) is satisfied: T($-$) and T($+$) transitions are observed when $\mathbf{B}_0 \parallel \mathbf{c}$. Moreover, when the magnetic field was aligned along the b axis then the $T_2(+)$ line disappeared in $\mathbf{E}_1 \parallel \mathbf{a}$ geometry (Fig. 4.5). This behavior is consistent with the dynamic DM mechanism selection rule i).

Secondly, the dependence of transition intensities on magnetic field. According to Eq. 2.32 a shift in energy of the triplet level reduces (increases) the separation between the triplet level and the relevant phonon mode and increases (decreases) coupling between the triplet and phonon states. The magnetic field dependence of the intensity of the triplet T_1 excitation, Fig. 4.6a, was fitted with singlet-triplet transition probabilities for the dynamic DM model, Eq. 2.32. The spin gap value $\Delta = \Delta_1 = 77.8\,\mathrm{cm}^{-1}$ and the g factor $g = g_c = 2.049$ were fixed parameters; the phonon frequency, ω_{ph}, and $I_p(qD_q)^2$ were the fitting parameters. The fit converged to a phonon at $\omega_{ph} = 94 \pm 0.3\,\mathrm{cm}^{-1}$. A phonon peak has been detected at 95 cm^{-1} by

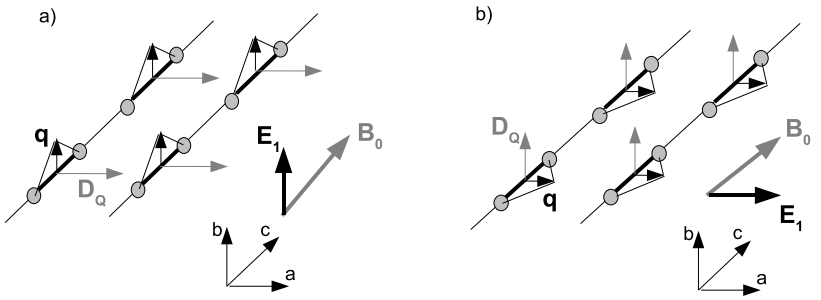

Figure 5.7: Dynamic Dzyaloshinskii-Moria vectors D_Q in the chains of $Sr_{14}Cu_{24}O_{41}$ in, a) $\mathbf{E}_1 \parallel \mathbf{a}$ and b) $\mathbf{E}_1 \parallel \mathbf{b}$.

reflectivity measurements [52]. In order to determine whether this 95 cm^{-1} phonon is the driving force behind the dynamic DM interaction in this compound normal mode calculations have to be performed. To our knowledge this has not been done yet for $Sr_{14}Cu_{24}O_{41}$.

Unfortunately, the limited B_0 range does not allow us to determine the dynamic DM-active a-axis optical phonon of T_2 triplet unambiguously.

Chapter 6

Conclusions

Terahertz spectroscopy in magnetic field can be used with success to study magnetic properties of low-dimensional spin materials. In this thesis dynamic Dzyaloshinskii-Moriya mechanism has been shown to cause singlet to triplet transitions in several spin systems and a detailed study of $Sr_{14}Cu_{24}O_{41}$ has been carried out.

- We have measured and reported the magnetic field and temperature dependence of two triplet modes in the chains of $Sr_{14}Cu_{24}O_{41}$ with zero field excitation energies $\Delta_1 = 77.8\,\mathrm{cm}^{-1}$ and $\Delta_2 = 87.7\,\mathrm{cm}^{-1}$ at 4 K.
- The triplet excitation at $77.8\,\mathrm{cm}^{-1}$ has not been observed before at the center of Brillouin zone. Hence the presently accepted spin lattice model for the chains in $Sr_{14}Cu_{24}O_{41}$ is incomplete and must include a triplet excitation at 77.8 cm^{-1} at $\mathbf{k} = 0$.
- We propose a back-folding of the triplet dispersion branches (observed in INS) due to the doubling of the magnetic supercell from 5 to 10 chain units.
- The determination of g factors for free spins ($g_c = 2.038$) and triplets ($g_{1c} = 2.049$, $g_{2c} = 2.044$) gave additional evidence that unpaired spins are in the chains and therefore the 5 chain unit periodicity cannot be retained.
- Observed optical selection rules for the otherwise forbidden singlet-triplet transitions are consistent with the dynamic Dzyaloshinskii-Moriya mechanism in all three studied compounds - α'-NaV_2O_5, $SrCu_2(BO_3)_2$ and $Sr_{14}Cu_{24}O_{41}$. Dynamic Dzyaloshinskii-Moriya mechanism has emerged as a single plausible explanation to an electric dipole interaction with spin lattice in the effective spin Hamiltonian representation.

Abstract

We have demonstrated that uniting high magnetic fields and sensitive detection with polarized THz radiation creates a valuable tool for investigating properties of low-dimensional spin systems. We have applied THz spectroscopy in studying magnetic field and temperature dependence of spin gap modes in α'-NaV_2O_5 and $SrCu_2(BO_3)_2$ and in particular in the chain substructure of $Sr_{14}Cu_{24}O_{41}$. "Telephone number" compound, $Sr_{14}Cu_{24}O_{41}$, is a representative of complicated structure type containing both one-dimensional CuO_2 spin chains and two-dimensional Cu_2O_3 spin ladders.

We found two triplet modes T_1 and T_2 at the center of the Brillouin zone at $\Delta_1 = 9.65\,\mathrm{meV}$ and $\Delta_2 = 10.86\,\mathrm{meV}$ in zero magnetic field. The T_1 mode was excited when the electric field vector **E** of the light was polarized along the b axis (perpendicular to the planes of chains and ladders) and T_2 was excited for $\mathbf{E} \parallel \mathbf{a}$ (perpendicular to the chains and along the ladder rungs). Up to the maximum magnetic field of 18 T, applied along the chains, the electron g factors of these two modes were similar, $g_{1c} = 2.049$ and $g_{2c} = 2.044$.

Full linewidth at half maximum for both modes was $1\,\mathrm{cm}^{-1}$ (0.12 meV) at 4 K and increased with temperature. The temperature dependence of mode energies and line intensities was in agreement with the inelastic neutron scattering results from two groups [Matsuda *et al.*, Phys. Rev. B **59**, 1060 (1999) and Regnault *et al.*, Phys. Rev. B **59**, 1055 (1999)]. The T_1 mode has not been observed by inelastic neutron scattering in the points of the k-space equivalent to the center of the Brillouin zone. Our study indicates that the zone structure model of magnetic excitations of $Sr_{14}Cu_{24}O_{41}$ must be modified to include a triplet mode at 9.65 meV in the center of the magnetic Brillouin zone.

It has been demonstrated experimentally that in three compounds, α'-NaV_2O_5, $SrCu_2(BO_3)_2$ and $Sr_{14}Cu_{24}O_{41}$, the observed singlet to triplet transitions are induced by electric field component of light. To account for electric dipole activity of singlet-triplet transitions the dynamic Dzyaloshinskii-

Moriya mechanism has been introduced. It explains experimentally observed polarization, frequency and magnetic field dependence of singlet to triplet transitions in $Sr_{14}Cu_{24}O_{41}$, and as well in α'-NaV_2O_5 and $SrCu_2(BO_3)_2$.

Kokkuvõte

Terahertspektroskoopia ehk kauge infrapunane spektroskoopia magnetväljades on tundlik meetod materjalide madalaenergeetiliste füüsikaliste omaduste uurimiseks. Oleme rakendanud kauget infrapunast spektroskoopiat spinnergastuste magnetvälja ning temperatuuri sõltuvuse uurimiseks $Sr_{14}Cu_{24}O_{41}$ ahelate alamsüsteemis. "Telefoni numbri" ühend, $Sr_{14}Cu_{24}O_{41}$, esindab keerukat struktuuri tüüpi, mis sisaldab nii ühemõõtmelisi CuO_2 spinnahelaid kui kahemõõtmelisi Cu_2O_3 spinnredeleid.

Leitud kahe tripletse ergastuse T_1 ja T_2 energia Brillouin'i tsooni keskel nullises magnetäljas on $\Delta_1 = 9.65\,\mathrm{meV}$ and $\Delta_2 = 10.86\,\mathrm{meV}$. Tripletne mood T_1 ergastus kui valguse elektrivektor **E** oli polariseeritud piki *b* kristalltelge ning mood T_2 ergastus kui $\mathbf{E} \parallel \mathbf{a}$. Kuni maksimaalse kasutatud väljatugevuseni (18 T) olid elektroni *g*-faktorid sarnased $g_{1c} = 2.049$ and $g_{2c} = 2.044$, kui magnetväli oli ahelate suunas.

Neeldumisjoonte laiused poole maksimumi peal olid mõlemal moodil $1\,\mathrm{cm}^{-1}$ (0.12 meV) temperatuuril 4 K ning kasvasid koos temperatuuri tõusuga. Mõlema moodi sageduse ja intensiivsuse temperatuurisõltuvus oli kooskõlas neutronhajumise andmetega kahe uurimisgrupi poolt [Matsuda *et al.*, Phys. Rev. B **59**, 1060 (1999) and Regnault *et al.*, Phys. Rev. B **59**, 1055 (1999)]. Tripletset moodi T_1 ei ole varem täheldatud pöördruumi punktides, mis vastavad Brillouin'i tsooni keskpunktile. Meie uuring näitab, et $Sr_{14}Cu_{24}O_{41}$ magnetergastuste tsooni mudelit peab täiendama tripletse moodiga energial 9.65 meV Brillouin'i tsooni keskel.

Käesolevas töös on eksperimentaalselt tõestatud, et kolmes ühendis - α'-NaV_2O_5, $SrCu_2(BO_3)_2$ ja $Sr_{14}Cu_{24}O_{41}$ - on singlett-triplett üleminekud põhjustatud valguse elektrivälja komponendi poolt. Dünaamilise Dzyaloshinskii-Moriya mehhanismi kirjeldus on esitatud seletamaks elektridipoolvälja mõju spinnsüsteemile. Viimane seletab eksperimendis nähtud singlett-triplett üleminekute polarisatsiooni, sageduse ja magnetvälja sõltuvuse kõigis kolmes ühendis.

Bibliography

[1] Dan Hüvonen, Urmas Nagel, Toomas Rõõm, P. Haas, M. Dressel, J. Hwang, T. Timusk, Y.-J. Wang, and J. Akimitsu. Magneto-optic far-infrared study of $Sr_{14}Cu_{24}O_{41}$: Triplet excitations in chains. *Phys. Rev. B*, 76:134418, 2007.

[2] T. Rõõm, D. Hüvonen, U. Nagel, Y.-J. Wang, and R. K. Kremer. Low-energy excitations and dynamic Dzyaloshinskii-Moriya interaction in α'-NaV_2O_5 studied by far-infrared spectroscopy. *Phys. Rev. B*, 69(14):144410, 2004.

[3] T. Rõõm, D. Hüvonen, U. Nagel, J. Hwang, T. Timusk, and H. Kageyama. Far-infrared spectroscopy of spin excitations and Dzyaloshinskii-Moriya interactions in the Shastry-Sutherland compound $SrCu_2(BO_3)_2$. *Phys. Rev. B*, 70(14):144417, 2004.

[4] Robert M. White. *Quantum Theory of Magnetism*. Springer, 2007.

[5] Charles Kittel. *Quantum Theory of Solids*. John Wiley & Sons, 1987.

[6] H. A. Kramers. L'interaction entre les atemos magnetogenes dans un cristal paramagnetique. *Physica A*, I.1:182, 1934.

[7] P. W. Anderson. Antiferromagnetism. Theory of Superexchange Interaction. *Phys. Rev.*, 79:350, 1950.

[8] Bill Sutherland. *Beautiful Models*. World Scientific Publishing Co. Pte. Ltd., 2004.

[9] D. C. Johnston, R. K. Kremer, M. Troyer, X. Wang, A. Klümper, S. L. Budko, A. F. Panchula, and P. C. Canfield. Thermodynamics of spin $S = 1/2$ antiferromagnetic uniform and alternating-exchange Heisenberg chains. *Phys. Rev. B*, 61(14):9558–9606, APR1 2000.

[10] I. Dzhyaloshinskii. A thermodynamic theory of weak ferromagnetism of antiferromagnetics. *J. Phys. Chem. Solids*, 4:241, 1958.

[11] T. Moriya. Anisotropic superexchange interaction and weak ferromagnetism. *Phys. Rev.*, 120(1):91–98, October 1 1960.

[12] F. Keffer. Moriya Interaction and the Problem of the Spin Arrangement in βMnS. *Phys. Rev.*, 126(3):896–900, May 1 1962.

[13] M. Lohmann, H. A. Krug von Nidda, M. V. Eremin, A. Loidl, G. Obermeier, and S. Horn. Charge Order in NaV_2O_5 Studied by EPR. *Phys. Rev. Lett.*, 85(8):1742, AUG 21 2000.

[14] L. Shekhtman, O. Entin-Wohlman, and A. Aharony. Moriya's anisotropic superexchange interaction, frustration, and Dzyaloshinsky's weak ferromagnetism. *Phys. Rev. Lett.*, 69(5):836–839, 1992.

[15] L. Shekhtman, A. Aharony, and O. Entin-Wohlman. Bond-dependent symmetric and antisymmetric superexchange interactions in La_2CuO_4. *Phys. Rev. B*, 47(1):174–182, 1993.

[16] Tôru Sakai, Olivier Cépas, and Timothy Ziman. An electron spin resonance selection rule for spin-gapped systems. *J. Phys. Soc. Jpn.*, 69(11):3521–3524, NOV 2000.

[17] O. Cépas, K. Kakurai, L. P. Regnault, T. Ziman, J. P. Boucher, N. Aso, M. Nishi, H. Kageyama, and Y. Ueda. Dzyaloshinski-Moriya Interaction in the 2D Spin Gap System $SrCu_2(BO_3)_2$. *Phys. Rev. Lett.*, 87:167205, 2001.

[18] O. Cépas, T. Sakai, and T. Ziman. Dynamics, selection rules and Dzyaloshinsky-Moriya interactions in strongly frustrated magnets. *Prog. Theor. Phys. Suppl.*, 145:43, 2002.

[19] P. P. Mitra and B. I. Halperin. Understanding far-infrared absorption in the S=1 antiferromagnetic chain compound NENP. *PRL*, 72:912, 1994.

[20] John Chamberlain. *The Principles of Interferometric Spectroscopy.* John Wiley, 1979.

[21] D. H. Martin and E. Puplett. Polarized interferometric spectrometry for the millimetre and submillimetre spectrum. *Infrared Physics*, 10:105, 1970.

[22] C. L. Mok, W. G. Chambers, T. J. Parkeran, and A. E. Costley. *Infrared Physics*, 19:437, 1979.

[23] D. H. Martin. *Infrared and Millimeter Waves*, volume 6. Academic Press, 1983.

[24] E. M. McCarron, M. A. Subramanian, J. C. Calabrese, and R. L. Harlow. The incommensurate structure of $Sr_{14-x}Ca_xCu_{24}O_{41}$ ($0 < x \quad 8$) a superconductor byproduct. *Materials Research Bulletin*, 23(9):1355, 1988.

[25] T. Siegrist, L. F. Schneemeyer, S. A. Sunshine, J. V. Waszczak, and S. Roth. A new layered cuprate structure-type, $(A_{1-x}A'_x)_{14}Cu_{24}O_{41}$. *Materials Research Bulletin*, 23(10):1429, 1988.

[26] M. Uehara, T. Nagata, J. Akimitsu, H. Takahashi, N. Mori, and K. Kinoshita. Superconductivity in the Ladder Material $Sr_{0.4}Ca_{13.6}Cu_{24}O_{41}$. *Journal of the Physical Society of Japan*, 65:2764, 1996.

[27] T. Vuletic, B. Korin-Hamzic, T. Ivek, S. Tomic, B. P. Gorshunov andM. Dressel, and J. Akimitsu. The spin-ladder and spin-chain system $(La, Y, Sr, Ca)_{14}Cu_{24}O_{41}$: Electronic phases, charge and spin dynamics. *Physics Reports*, 428:169–258, 2006.

[28] F. C. Zhang and T. M. Rice. Effective Hamiltonian for the superconducting Cu oxides. *Phys. Rev. B*, 37(7):3759–3761, Mar 1988.

[29] M. Matsuda and K. Katsumata. Observation of a dimerized state in the S=1/2 quasi-one-dimensional antiferromagnet $Sr_{14}Cu_{24}O_{41}$. *Phys. Rev. B*, 53(18):12201–12205, May 1996.

[30] S. A. Carter, B. Batlogg, R. J. Cava, J. J. Krajewski, W. F. Peck, Jr., and T. M. Rice. Hole Doping of the CuO_2 Chains in $(La,Sr,Ca)_{14}Cu_{24}O_{41}$. *Phys. Rev. Lett.*, 77(7):1378–1381, Aug 1996.

[31] Masashi Takigawa, Naoki Motoyama, Hiroshi Eisaki, and Shinichi Uchida. Spin and charge dynamics in the hole-doped one-dimensional-chain˘ladder composite material $Sr_{14}Cu_{24}O_{41}$: Cu NMR/NQR studies. *Phys. Rev. B*, 57(2):1124–1140, Jan 1998.

[32] M. Matsuda, T. Yosihama, K. Kakurai, and G. Shirane. Quasi-two-dimensional hole ordering and dimerized state in the CuO_2-chain layers in $Sr_{14}Cu_{24}O_{41}$. *Phys. Rev. B*, 59(2):1060–1067, Jan 1999.

[33] L. P. Regnault, J. P. Boucher, H. Moudden, J. E. Lorenzo, A. Hiess, U. Ammerahl, G. Dhalenne, and A. Revcolevschi. Spin dynamics in the magnetic chain arrays of $Sr_{14}Cu_{24}O_{41}$: A neutron inelastic scattering investigation. *Phys. Rev. B*, 59(2):1055–1059, Jan 1999.

[34] Roger S. Eccleston, Masatomo Uehara, Jun Akimitsu, Hiroshi Eisaki, Naoki Motoyama, and Shin-Ichi Uchida. Spin Dynamics of the Spin-Ladder Dimer-Chain Material $Sr_{14}Cu_{24}O_{41}$. *Phys. Rev. Lett.*, 81(8):1702–1705, Aug 1998.

[35] T. Fukuda, J. Mizuki, and M. Matsuda. Periodic hole structure in a spin-chain ladder material $Sr_{14}Cu_{24}O_{41}$. *Phys. Rev. B*, 66(1):012104, Jul 2002.

[36] Sander van Smaalen. Comment on "Periodic hole structure in a spin-chain ladder material $Sr_{14}Cu_{24}O_{41}$". *Physical Review B (Condensed Matter and Materials Physics)*, 67(2):026101, 2003.

[37] M. Braden, J. Etrillard, A. Gukasov, U. Ammerahl, and A. Revcolevschi. Neutron diffraction study of the lattice distortion related to charge ordering in $Sr_{14}Cu_{24}O_{41}$. *Physical Review B (Condensed Matter and Materials Physics)*, 69(21):214426, 2004.

[38] J. Etrillard, M. Braden, A. Gukasov, U. Ammerahl, and A. Revcolevschi. Structural aspects of the spin-ladder compound $Sr_{14}Cu_{24}O_{41}$. *Physica C*, 403:290–296, 2004.

[39] Y. Gotoh, I. Yamaguchi, Y. Takahashi, J. Akimoto, M. Goto, M. Onoda, H. Fujino, T. Nagata, and J. Akimitsu. Structural modulation, hole distribution, and hole-ordered structure of the incommensurate composite crystal $(Sr_2Cu_2O_3)_{0.70}CuO_2$. *Physical Review B (Condensed Matter and Materials Physics)*, 68(22):224108, 2003.

[40] Y. Gotoh, I. Yamaguchi, H. Eisaki, T. Nagata, and J. Akimitsu. Temperature dependence of atomic modulation in the incommensurate composite crystal structure of $(Sr_2Cu_2O_3)_{0.70}CuO_2$. *Physica C: Superconductivity*, 445-448:107, 2006.

[41] Tomoko Ohta, Fujio Izumi, Mitsuko Onoda, Masaaki Isobe, Eiji Takayama-Muromachi, and Alan W. Hewat. Modulated Structure of the Composite Crystal $Ca_{13.6}Sr_{0.4}Cu_{24+y}O_{41+z}$. *Journal of the Physical Society of Japan*, 66:3107, 1997.

[42] M. Isobe, M. Onoda, T. Ohta, F. Izumi, K. Kimoto, E. Takayama-Muromachi, A. W. Hewat, and K. Ohoyama. Low-temperature crystal and magnetic structures of the chain-ladder composite material $Sr_{0.4}Ca_{13.6}Cu_{24+y}O_{41+z}$: Hole redistribution and antiferromagnetic order. *Phys. Rev. B*, 62(17):11667–11676, Nov 2000.

[43] Alain Gelle and Marie-Bernadette Lepetit. Influence of the Incommensurability in $Sr_{14-x}Ca_xCu_{24}O_{41}$ Family Compounds. *Physical Review Letters*, 92(23):236402, 2004.

[44] A. Gelle and M.-B. Lepetit. $Sr_{14}Cu_{24}O_{41}$: a complete model for the chain sub-system. *The European Physics Journal B*, 46:489–496, 2005.

[45] N. Nücker, M. Merz, C. A. Kuntscher, S. Gerhold, S. Schuppler, R. Neudert, M. S. Golden, J. Fink, D. Schild, S. Stadler, V. Chakarian, J. Freeland, Y. U. Idzerda, K. Conder, M. Uehara, T. Nagata, J. Goto, J. Akimitsu, N. Motoyama, H. Eisaki, S. Uchida, U. Ammerahl, and A. Revcolevschi. Hole distribution in $(Sr, Ca, Y, La)_{14}Cu_{24}O_{41}$ ladder compounds studied by x-ray absorption spectroscopy. *Phys. Rev. B*, 62(21):14384–14392, Dec 2000.

[46] T. Osafune, N. Motoyama, H. Eisaki, and S. Uchida. Optical Study of the $Sr_{14-x}Ca_xCu_{24}O_{41}$ System: Evidence for Hole-Doped Cu_2O_3 Ladders. *Phys. Rev. Lett.*, 78(10):1980–1983, Mar 1997.

[47] V. Kataev, K.-Y. Choi, M. Grüninger, U. Ammerahl, B. Büchner, A. Freimuth, and A. Revcolevschi. Interplay of spin and charge dynamics in $Sr_{14-x}Ca_xCu_{24}O_{41}$. *Phys. Rev. B*, 64(10):104422, Aug 2001.

[48] R. Klingeler, B. Buchner, K.-Y. Choi, V. Kataev, U. Ammerahl, A. Revcolevschi, and J. Schnack. Magnetism of hole-doped CuO_2 spin chains in $Sr_{14}Cu_{24}O_{41}$: Experimental and numerical results. *Physical Review B (Condensed Matter and Materials Physics)*, 73(1):014426, 2006.

[49] A. Rusydi, P. Abbamonte, H. Eisaki, Y. Fujimaki, S. Smadici, N. Motoyama, S. Uchida, Y.-J. Kim, M. Rubhausen, and G. A. Sawatzky. Strain Amplification of the $4k_F$ Chain Instability in $Sr_{14}Cu_{24}O_{41}$. *Physical Review Letters*, 100(3):036403, 2008.

[50] Z. V. Popović, M. J. Konstantinović, R. Gajić, V. N. Popov, M. Isobe, Y. Ueda, and V. V. Moshchalkov. Phonon dynamics in AV_2O_5 (A = Na, Ca, Mg, Cs) oxides. *Phys. Rev. B*, 65:184303, 2002.

[51] T. Rõõm, U. Nagel, E. Lippmaa, H. Kageyama, K. Onizuka, and Y. Ueda. Far-infrared study of the two-dimensional dimer spin system $SrCu_2(BO_3)_2$. *Phys. Rev. B*, 61:14342, 2000.

[52] P. Haas and M. Dressel. reflectivity data from a private communication. *unpublished*, 2000.

Appendixes

Curriculum Vitae

Name **Dan Hüvonen**

Date of birth **26.09.1977**

E-mail **dan@kbfi.ee**

Nationality **Estonian**

Employment

National Institute of Chemical Physics and Biophysics, research scientist, 2002 - today

Sysop OÜ, Tallinn, computer specialist, 1998 - 2002

Educational Center of Tallinn, informatics teacher, 1995 - 2001; computer engineer, 1998 - 2001

Education

PhD Student, from 2002, supervisors Toomas Rõõm (NICPB), Urmas Nagel (NICPB), *Terahertz spectroscopy of spin and charge in low-dimensional systems*, Tallinn University of Technology and National Institute of Chemical Physics and Biophysics

Master's Degree, 2002, supervisor Arvo Mere, *Dielectric relaxation in potassium substituted hydrosodalites*, Tallinn University of Technology, Faculty of Science

Bachelor's Degree, 1999, supervisor Arvo Mere, *Dielectric relaxation in hydrosodalites*, Tallinn University of Technology, Faculty of Science

programmer, Educational Center of Tallinn, 1995

Tondiraba Secondary School, Tallinn, 1995

Scholarships

Kristjan Jaak's travel scholarship to conduct experimental work in National High Magnetic Field Laboratory, Tallahasse, USA, august 2005.

Publications

Hüvonen, D.; Nagel, Urmas; Rõõm, Toomas; Haas, P.; Dressel, M.; Hwang, J.; Timusk, T.; Wang, Y.-J.; Akimitsu, J. (2007). *Magneto-optic far-infrared study of $Sr_{14}Cu_{24}O_{41}$: Triplet excitations in chains.* Physical Review B, 76(13), 134418

Rõõm, T.; **Hüvonen, D.**; Nagel, U.; Hwang, J.; Timusk, T.; Kageyama, H. (2004). *Far-infrared spectroscopy of spin excitations and Dzyaloshinskii-Moriya interactions in a Shastry-Sutherland compound $SrCu_2(BO_3)_2$.* Physical Review B, 70, 144417 - 144417-8.

Rõõm, T.; **Hüvonen, D.**; Nagel, U.; Wang, Y.-J.; Kremer, R. K. (2004). *Low-energy excitations and dynamic Dzyaloshinskii-Moriya interaction in a'-NaV_2O_5 studied by far-infrared spectroscopy.* Physical Review B, 69, 144410 - 144410-19.

Mere, A.; **Hüvonen, D.**; Heinmaa, I.; Ruus, T. (2001). *Synthesis and electrical properties of potassium substituted hydrosodalites.* In: SMART OPTICAL INORGANIC STRUCTURES AND DEVICES : Conference on Smart Optical Inorganic Structures and Devices, AUG 16-19, 2000. , 2001, 301 - 306.

Conference presentations

Rõõm, T.; **Hüvonen, D.**; Nagel , H. Engelkamp, Y.J. Choi, C.L. Zhang, S. Park, S.-W. Cheong, M. Mostovoy (2008). *Spin Waves in multiferroic $LiCu_2O_2$: far infrared study in magnetic field.* Conference of Doctoral School of Material Science and Material Technology, Kääriku, Estonia, 2008, Poster.

Hüvonen, D.; Nagel, U.; Rõõm, T.; Haas, P.; Dressel, M.; Hwang, J.; Timusk, T.; Wang, Y.-J.; Akimitsu, J. (2007). *Far-infrared study of gapped spin excitations in the chains of* $Sr_{14}Cu_{24}O_{41}$. APS March Meeting, Denver CO, March 5-9, 2007, U15.00006, Talk.

Hüvonen, D.; Nagel, U.; Rõõm, T.; Haas, P.; Dressel, M.; Hwang, J.; Timusk, T.; Wang, Y.-J.; Akimitsu, J. (2007). *Low energy properties of* $Sr_{14}Cu_{24}O_{41}$, Conference of Doctoral School of Material Science and Material Technology, Tartu, Estonia, 2007, Talk.

Rõõm, T.; **Hüvonen, D.**; Nagel, U.; Haas, P.; Gorshunov, B.; Dressel, M.; Wang, Y.-J.; Akimitsu, J.; Sasaki, T.; Nagata, T. (2006). *Far-infrared study of* $Sr_{14}Cu_{24}O_{41}$*: spin gap in* CuO_2 *chains.* In: Low Energy Electrodynamics in Solids: Low Energy Electrodynamics in Solids, Laulasmaa, Estonia, 01.07.2006 - 06.07.2006, 2006, 23 - 23, Talk.

Hüvonen, D. (2006). *Low-dimensional magnetism through the eye of terahertz spectroscopy.* Conference of Doctoral School of Material Science and Material Technology, Tartu, Estonia, 2006, Talk.

Hüvonen, D.; Nagel, U.; Rõõm, T. (2005) *Low-dimensional magnetism studied by infrared spectroscopy*, Estonian Physical Society Meeting 2005, Tartu, Estonia, Talk.

Hüvonen, D. (2004). *Terahertz spectroscopy of spin excitations*, International Conference for Physics Students 2004, Novi Sad, Serbia, Talk.

Hüvonen, D.; Nagel, U.; Rõõm, T. (2004). *Far-Infrared Spectroscopy and Cluster Simulations of the Shastry-Sutherland Model for* $SrCu_2(BO_3)_2$. March Metting of the American Physcal Society. Montreal, Canada; March 22-26, 2004. , 2004, C1.089, Poster.

Nagel, U.; **Hüvonen, D.**; Rõõm, T.; Kageyama, H. (2004). *Far-infrared spectroscopy of spin excitations in* $SrCu_2(BO_3)_2$ *and dynamic Dzyaloshinskii-Moriya interaction.* March Metting of the American Physcal Society. Montreal, Canada; March 22-26, 2004. , 2004, P25.009, Talk.

Elulookirjeldus

Nimi **Dan Hüvonen**

Snniaeg **26.09.1977**

E-post **dan@kbfi.ee**

Rahvus **eestlane**

Teenistuskäik

Keemilise ja Bioloogilise Füüsika Instituut, teadur, alates 2002

Sysop OÜ, arvutispetsialist, 1998 - 2002

Tallinna Kesklinna Koolidevaheline Õppekeskus, informaatika õpetaja, 1995 2001; arvutispetsialist, 1998 - 2001

Haridustee

Doktorant, 2002 - ..., juhendajad Toomas Rõõm (NICPB), Urmas Nagel (NICPB), Spinni ja laengu teraherts-spektroskoopia madalamõõduslistes süsteemides, Tallinna Tehnikalikool ning Keemilise ja Bioloogilise Füüsika Instituut

Magistri kraad, 2002, juhendaja Arvo Mere, Dipoolne relaksatsioon kaaliumiga asendatud hdrosodaliitides, Tallinna Tehnikaülikool, Matemaatika-loodusteaduskond

Bakalaureuse kraad, 1999, juhendaja Arvo Mere, Dipoolne relaksatsioon hdrosodaliitides, Tallinna Tehnikaülikool, Matemaatika-loodusteaduskond

Laborant-programmeerija kutse, Tallinna Kesklinna Koolidevaheline Õppekeskus, 1995

Keskharidus, Tondiraba Keskkool, Tallinn, 1995

Stipendiumid

Kristjan Jaagu välislähetuse stipendium eksperimendi läbiviimiseks Rahvuslikus Kõrgete Magnetväljade Laboratooriumis, Tallahasse, USA, august 2005.

Publikatsioonid

Hüvonen, D.; Nagel, Urmas; Rõõm, Toomas; Haas, P.; Dressel, M.; Hwang, J.; Timusk, T.; Wang, Y.-J.; Akimitsu, J. (2007). *Magneto-optic far-infrared study of $Sr_{14}Cu_{24}O_{41}$: Triplet excitations in chains.* Physical Review B, 76(13), 134418

Rõõm, T.; **Hüvonen, D.**; Nagel, U.; Hwang, J.; Timusk, T.; Kageyama, H. (2004). *Far-infrared spectroscopy of spin excitations and Dzyaloshinskii-Moriya interactions in a Shastry-Sutherland compound $SrCu_2(BO_3)_2$.* Physical Review B, 70, 144417 - 144417-8.

Rõõm, T.; **Hüvonen, D.**; Nagel, U.; Wang, Y.-J.; Kremer, R. K. (2004). *Low-energy excitations and dynamic Dzyaloshinskii-Moriya interaction in a'-NaV_2O_5 studied by far-infrared spectroscopy.* Physical Review B, 69, 144410 - 144410-19.

Mere, A.; **Hüvonen, D.**; Heinmaa, I.; Ruus, T. (2001). *Synthesis and electrical properties of potassium substituted hydrosodalites.* In: SMART OPTICAL INORGANIC STRUCTURES AND DEVICES : Conference on Smart Optical Inorganic Structures and Devices, AUG 16-19, 2000. , 2001, 301 - 306.

Konverentsiettekanded

Rõõm, T.; **Hüvonen, D.**; Nagel , H. Engelkamp, Y.J. Choi, C.L. Zhang, S. Park, S.-W. Cheong, M. Mostovoy (2008). *Spin Waves in multiferroic $LiCu_2O_2$: far infrared study in magnetic field.* Conference of Doctoral School of Material Science and Material Technology, Kääriku, Estonia, 2008, Poster.

Hüvonen, D.; Nagel, U.; Rõõm, T.; Haas, P.; Dressel, M.; Hwang, J.; Timusk, T.; Wang, Y.-J.; Akimitsu, J. (2007). *Far-infrared study of gapped spin excitations in the chains of $Sr_{14}Cu_{24}O_{41}$.* APS March Meeting, Denver CO, March 5-9, 2007, U15.00006, Suuline.

Hüvonen, D.; Nagel, U.; Rõõm, T.; Haas, P.; Dressel, M.; Hwang, J.; Timusk, T.; Wang, Y.-J.; Akimitsu, J. (2007). *Low energy properties of $Sr_{14}Cu_{24}O_{41}$*, Conference of Doctoral School of Material Science and Material Technology, Tartu, Estonia, 2007, Suuline.

Rõõm, T.; **Hüvonen, D.**; Nagel, U.; Haas, P.; Gorshunov, B.; Dressel, M.; Wang, Y.-J.; Akimitsu, J.; Sasaki, T.; Nagata, T. (2006). *Far-infrared study of $Sr_{14}Cu_{24}O_{41}$: spin gap in CuO_2 chains.* In: Low Energy Electrodynamics in Solids: Low Energy Electrodynamics in

Solids, Laulasmaa, Estonia, 01.07.2006 - 06.07.2006, 2006, 23 - 23, Suuline.

Hüvonen, D. (2006). *Low-dimensional magnetism through the eye of terahertz spectroscopy.* Conference of Doctoral School of Material Science and Material Technology, Tartu, Estonia, 2006, Suuline.

Hüvonen, D.; Nagel, U.; Rõõm, T. (2005) *Low-dimensional magnetism studied by infrared spectroscopy*, Estonian Physical Society Meeting 2005, Tartu, Estonia, Talk.

Hüvonen, D. (2004). *Terahertz spectroscopy of spin excitations*, International Conference for Physics Students 2004, Novi Sad, Serbia, Suuline.

Hüvonen, D.; Nagel, U.; Rõõm, T. (2004). *Far-Infrared Spectroscopy and Cluster Simulations of the Shastry-Sutherland Model for* $SrCu_2(BO_3)_2$. March Metting of the American Physcal Society. Montreal, Canada; March 22-26, 2004. , 2004, C1.089, Poster.

Nagel, U.; **Hüvonen, D.**; Rõõm, T.; Kageyama, H. (2004). *Far-infrared spectroscopy of spin excitations in* $SrCu_2(BO_3)_2$ *and dynamic Dzyaloshinskii-Moriya interaction.* March Metting of the American Physcal Society. Montreal, Canada; March 22-26, 2004. , 2004, P25.009, Suuline.

Published Papers

Hüvonen, D.; Nagel, Urmas; Rõõm, Toomas; Haas, P.; Dressel, M.; Hwang, J.; Timusk, T.; Wang, Y.-J.; Akimitsu, J. (2007). *Magneto-optic far-infrared study of $Sr_{14}Cu_{24}O_{41}$: Triplet excitations in chains.* Physical Review B, 76(13), 134418

Rõõm, T.; **Hüvonen, D.**; Nagel, U.; Hwang, J.; Timusk, T.; Kageyama, H. (2004). *Far-infrared spectroscopy of spin excitations and Dzyaloshinskii-Moriya interactions in a Shastry-Sutherland compound $SrCu_2(BO_3)_2$.* Physical Review B, 70, 144417 - 144417-8.

Rõõm, T.; **Hüvonen, D.**; Nagel, U.; Wang, Y.-J.; Kremer, R. K. (2004). *Low-energy excitations and dynamic Dzyaloshinskii-Moriya interaction in a'-NaV_2O_5 studied by far-infrared spectroscopy.* Physical Review B, 69, 144410 - 144410-19.

Magneto-optic far-infrared study of $Sr_{14}Cu_{24}O_{41}$: Triplet excitations in chains

D. Hüvonen,* U. Nagel, and T. Rõõm
National Institute of Chemical Physics and Biophysics, Akadeemia tee 23, 12618 Tallinn, Estonia

P. Haas and M. Dressel
1. Physikalisches Institut, Universität Stuttgart, D-70550 Stuttgart, Germany

J. Hwang and T. Timusk
Department of Physics and Astronomy, McMaster University, Hamilton, Ontario, Canada L8S4M1

Y.-J. Wang
National High Magnetic Field Laboratory, Florida State University, 1800 East Paul Dirac Drive, Tallahassee, Florida 32306, USA

J. Akimitsu
Department of Physics and Mathematics, Aoyama-Gakuin University, Fuchinobe 5-10-1, Sagamihara, Kanagawa 229-8558, Japan
(Received 28 June 2007; published 23 October 2007)

Using far-infrared spectroscopy, we have studied the magnetic field and temperature dependence of the spin gap modes in the chains of $Sr_{14}Cu_{24}O_{41}$. Two triplet modes T_1 and T_2 were found in the center of the Brillouin zone at $\Delta_1=9.65$ meV and $\Delta_2=10.86$ meV in zero magnetic field. The T_1 mode was excited when the electric field vector **E** of the light was polarized along the *b* axis (perpendicular to the planes of chains and ladders) and T_2 was excited for $\mathbf{E}\|\mathbf{a}$ (perpendicular to the chains and along the rungs). Up to the maximum magnetic field of 18 T, applied along the chains, the electron *g* factors of these two modes were similar, $g_{1c}=2.049$ and $g_{2c}=2.044$. Full linewidth at half maximum for both modes was 1 cm^{-1} (0.12 meV) at 4 K and increased with *T*. The temperature dependence of mode energies and line intensities was in agreement with the inelastic neutron scattering results from two groups [M. Matsuda *et al.*, Phys. Rev. B **59**, 1060 (1999); L. P. Regnault *et al.*, *ibid* **59**, 1055 (1999)]. The T_1 mode has not been observed by inelastic neutron scattering in the points of the *k* space equivalent to the center of the Brillouin zone. Our study indicates that the zone structure model of magnetic excitations of $Sr_{14}Cu_{24}O_{41}$ must be modified to include a triplet mode at 9.65 meV in the center of the magnetic Brillouin zone.

DOI: 10.1103/PhysRevB.76.134418 PACS number(s): 75.25.+z, 78.30.−j, 75.10.Pq, 63.20.Kr

I. INTRODUCTION

Heisenberg spin 1/2 systems have been investigated extensively both by experimental and theoretical means due to their versatile low-energy physical properties and also because of their relevance to high-T_c superconducting materials. The search for high-T_c superconductor materials has led to a new structure type[1,2] represented by $Sr_{14}Cu_{24}O_{41}$ containing both one-dimensional CuO_2 spin chains and two-dimensional Cu_2O_3 spin ladders. Planar chains and ladders in this compound extend in the *c* axis direction and are alternately stacked along the *b* axis, separated by layers of Sr. Chain and ladder spin subsystems in $Sr_{14}Cu_{24}O_{41}$ interact weakly and are structurally incommensurate although the lattice constants in the *c* direction satisfy an approximate relation $10c_{chain}\approx 7c_{ladder}$. The conductivity in $Sr_{14}Cu_{24}O_{41}$ is associated with the charge dynamics in the ladder layers. Sr substitution for Ca and external pressure leads to hole transfer from the chains to the ladders and to the occurrence of superconductivity in $Sr_{0.4}Ca_{13.6}Cu_{24}O_{41}$ with $T_c=12$ K at 3 GPa.[3] For a comprehensive overview on the charge and spin dynamics in this class of materials, the reader is directed to Ref. 4. Pure $Sr_{14}Cu_{24}O_{41}$ is a self-doped compound containing six holes per unit cell. A chain hole occupies oxygen $2p$ orbitals surrounding a central Cu spin and forms a Zhang-Rice (ZR) singlet[5] (-0-), rendering about six out of ten Cu sites nonmagnetic. Spin dimers, two Cu^{2+} spins bridged by a ZR singlet (-↑-0-↓-),[6–8] are in the singlet state. Inelastic neutron scattering,[9–11] high-energy x-ray diffraction,[12] and NMR[8] measurements have indicated that dimers organize with a periodicity of five chain units and are separated by two ZR singlets (-↑-0-↓-0-0-).

Recent revised structural studies indicate extensive O atom position modulation out of the chain planes in $Sr_{14}Cu_{24}O_{41}$ (Refs. 13–17) and $Sr_{0.4}Ca_{13.6}Cu_{24}O_{41}$.[18] This modulation causes variations in the superexchange between Cu atoms along the chain.[19,20] In addition, displaced O atoms mediate the hole transfer between chains and ladders. It is estimated from bond-valence sum calculations, x-ray absorption spectroscopy, magnetization, and optical conductivity measurements[7,16,21–24] that 1%–4% of the self-doped holes reside in the ladders in undoped $Sr_{14}Cu_{24}O_{41}$ at low temperature. The deficiency of holes in the chains means that the perfect alignment of dimers, separated by two ZR singlets yielding five chain unit periodicity, cannot be satisfied. There is a lack of consensus in the literature regarding spin and charge order in the chains of $Sr_{14}Cu_{24}O_{41}$ and the nature of the underlying ground state. We studied magnetic excitations using far-infrared (FIR) spectroscopy and strong magnetic fields with the aim to identify the spin states present in the chains of $Sr_{14}Cu_{24}O_{41}$.

II. EXPERIMENT

FIR transmission spectra were recorded with a polarizing Martin-Puplett-type Fourier transform spectrometer SPS200. Samples, a 12 T superconducting magnet, and two 0.3 K silicon bolometers were inside a ^{4}He cryostat connected to the spectrometer through light pipe. A rotatable polarizer was placed in front of the sample. Spectra in fields above 12 T were measured at NHMFL in Tallahassee and in University of Toronto with 18 T superconducting magnets. In Tallahassee, experiments were carried out utilizing Bruker IFS 113v and a 4 K silicon bolometer, and in Toronto, spectrometer SPS200 was used with a 0.3 K silicon bolometer. Two single-crystalline samples of $Sr_{14}Cu_{24}O_{41}$ were used in the current study: a 1.1 mm thick crystal with an *ab*-plane area of 13.2 mm^2 and an *ac*-plane crystal with an area of 12.6 mm^2 and a thickness of 0.65 mm.

Differential absorption spectra in magnetic fields were calculated from transmitted intensity $I(B_0,\omega)$ using the following formula: $\alpha(B_0,\omega)-\alpha(B_0^r,\omega)=(-1/d)\ln(I(B_0,\omega)/I(B_0^r,\omega))$, where B_0 is the applied magnetic field, B_0^r is the reference field, and d is sample thickness. Consequently, in differential absorption spectra presented in this paper, lines belonging to reference magnetic field spectra are pointing downward, if present, and lines in fields under observation are pointing upward.

III. RESULTS

Polarization-sensitive transmission measurements in the FIR spectral region revealed an anisotropic response from the crystal *ab* plane. When the external magnetic field was applied along the *c* axis of the crystal (along the chains), two magnetic field dependent modes, T_1 and T_2, were found, which we assign to spin excitations in the chains of $Sr_{14}Cu_{24}O_{41}$. Transitions to the triplet state T_1 were visible when the electric field component $\mathbf{E}_1$ of the radiation was polarized along the *b* axis. Observed differential absorption spectra, measured in different magnetic fields at 4 K, are shown in Fig. 1. The triplet state has three spin sublevels $M_S=-1,0,+1$, which we denote as $T(-)$, $T(0)$, and $T(+)$, see inset of Fig. 3. The resonance frequency of the $T_1(0)$ level does not shift with field and thus escapes detection. The transition to the $T_1(-)$ sublevel loses intensity as the line shifts toward smaller energies in increasing field and gets too weak for detection in fields above 12 T. The transition to the $T_1(+)$ level gains intensity with increasing magnetic field up to the observation limit set by the strong phonon background at 92 cm^{-1} where the crystal becomes opaque to FIR radiation in $\mathbf{E}_1\|\mathbf{b}$ polarization.

In $\mathbf{E}_1\|\mathbf{a}$ polarization, transitions to the triplet state T_2 are observed (Fig. 2). Transitions to the $T_2(+)$ level in fields below 2 T and to the $T_2(-)$ level are masked by strong absorption below 89 cm^{-1}. To check the light polarization and $\mathbf{B}_0$ orientation dependence, measurements on a thinner *ac*-plane crystal in Faraday and Voigt configurations were carried out. When $\mathbf{B}_0\|\mathbf{b}$, the triplet T_2 mode disappears from the infrared absorption spectrum. Some absorption lines belonging to the $T_2(-)$ level were detected in Voigt configuration. However, because of strong phononic absorption, the intensities of $T_2(-)$ were not reliable and are not included in Fig. 3(a).

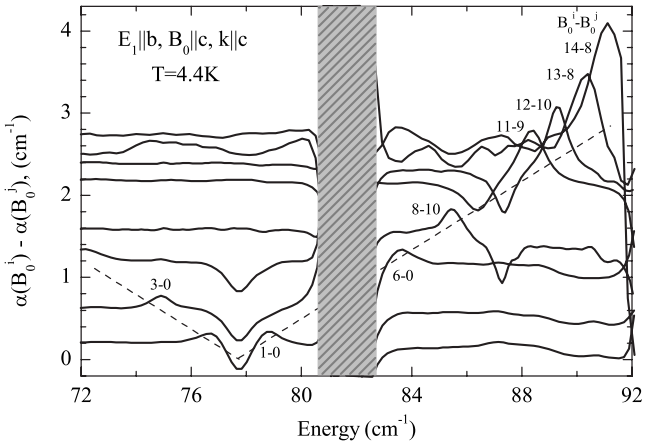

FIG. 1. Differential absorption spectra of triplet T_1 in magnetic field applied in the *c* axis direction with light *k* vector $\mathbf{k}\|\mathbf{c}$ and polarization $\mathbf{E}_1\|\mathbf{b}$ at 4.4 K. The spectra are shifted in the vertical direction by $0.2B_0^i$. Numbers beside absorption lines give values of the applied field B_0^i and reference field B_0^j. Dashed lines are eye guides. The shaded area covers the spectral region of strong phonon absorption.

The spectral lines were fitted with a Lorentzian line shape. Line positions and intensities as a function of magnetic field are displayed in Fig. 3. We assume that $T_1(-)$ and $T_1(+)$ are degenerate at $B_0=0$ T and plot half of the measured line intensity for this field value. The same holds for the T_2 triplet. Linewidths of both triplets are 1 ± 0.2 cm^{-1} and do not depend on the strength of the magnetic field. The corresponding *g* factors are similar, $g_{1c}=2.049\pm0.012$ and g_{2c}

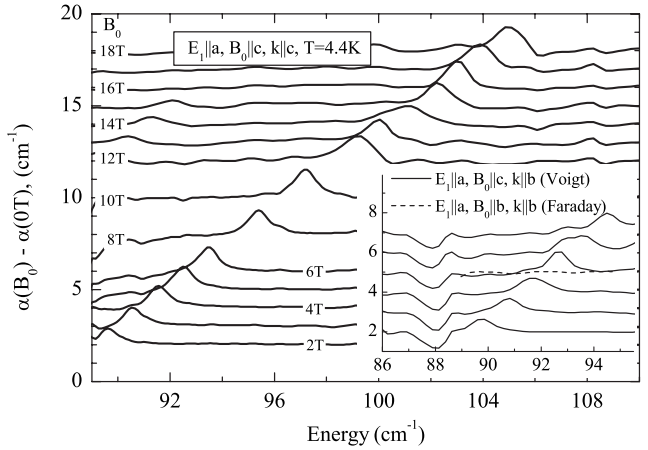

FIG. 2. Differential absorption spectra of triplet T_2 in magnetic field applied in the *c* axis direction with light *k* vector $\mathbf{k}\|\mathbf{c}$ and polarization $\mathbf{E}_1\|\mathbf{a}$ at 4.4 K measured using the *ab*-plane crystal. The spectra are offset in vertical direction by magnetic field value B_0. The inset shows differential absorption spectra for the *ac*-plane crystal in Faraday (dashed line) and Voigt (solid line) configurations. Triplet $T_2(+)$ is not infrared active when $\mathbf{B}_0\|\mathbf{b}$, as shown by the dashed line for an arbitrary chosen $B_0=5$ T.

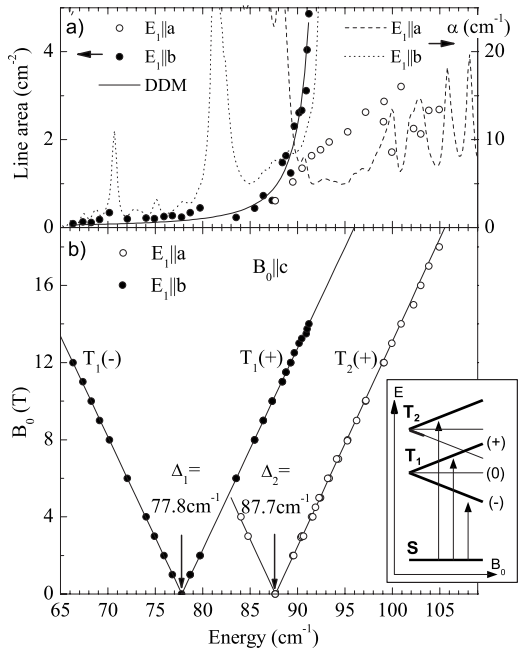

FIG. 3. Magnetic field $\mathbf{B}_0\|\mathbf{c}$ dependence of line areas and positions. (a) Line areas of triplet modes (left axis) and FIR absorption spectra (right axis) at temperature of 4.4 K for $\mathbf{E}_1\|\mathbf{a}$ and $\mathbf{E}_1\|\mathbf{b}$ polarizations. The solid line is the dynamic Dzyaloshinskii-Moriya interaction model fit of the T_1 absorption line area. (b) T_1 and T_2 line positions as a function of magnetic field B_0. The inset schematically shows the observed transitions.

$=2.044\pm0.014$. Additionally, we observed a strong paramagnetic signal at 4 K with $g_c=2.038\pm0.016$ (Fig. 4). The linewidth of the paramagnetic signal was below the used instrumental resolution limit, 0.3 cm^{-1}.

The temperature dependence of the singlet-triplet resonances was measured as the difference of 0 and 10 T spectra at temperatures from 4 to 60 K, see Fig. 5. Figure 5(b) shows absorption lines in 0 T field for triplet T_1. $Sr_{14}Cu_{24}O_{41}$ is not transparent in $\mathbf{E}_1\|\mathbf{a}$ polarization at zero field line position frequencies of T_2, and therefore, we analyze the T dependence of this triplet level in 10 T field. Although both lines broaden and lose intensity as temperature increases, the T dependence of line positions is different. The T_1 triplet resonance shifts notably toward higher energies, whereas the energy of T_2 remains unchanged, see Fig. 5(c).

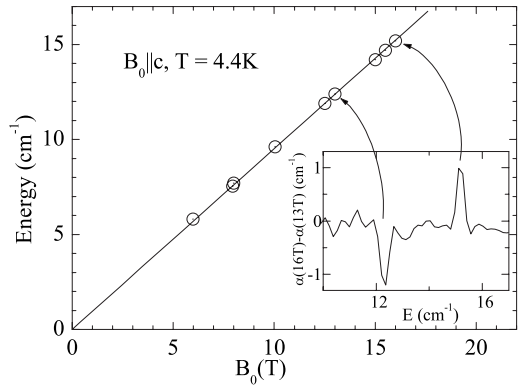

FIG. 4. Magnetic field dependence of the paramagnetic transition energy in $\mathbf{B}_0\|\mathbf{c}$ orientation. The line is a fit to the data yielding g factor $g_c=2.038\pm0.016$. The inset demonstrates the paramagnetic transition signal in differential absorption spectrum. The linewidth is resolution limited by instrument to 0.3 cm^{-1}.

IV. DISCUSSION

The dispersion curves of two magnetic excitations, acoustic and optic, with respective energies of 11 and 12.5 meV at k points equivalent to $\mathbf{k}=0$ have been measured by inelastic neutron scattering (INS) spectroscopy.[9,10] A good fit of the experimental data was obtained by the simplest model for a weakly coupled dimer system. The dispersion in the c axis direction follows a cosine form with the periodicity of 0.2 reciprocal lattice units (Fig. 6). The temperature dependence of INS data demonstrated that with increasing temperature, the dispersion curves flatten out since the interdimer couplings become negligible due to thermal fluctuations and the dimers behave more like isolated dimers. As the dispersion curves flatten, the acoustic mode at k space points near the Brillouin zone edge $(H,K,0.1)$ shifts toward higher energies, while the triplet state energy at $(H,K,0)$ does not change (reciprocal lattice units H and K are integers in our discussion). In contrast to these considerations, the energy of the optic branch at $(H,K,0.1)$ in the momentum space displays no temperature dependence, while the energy near $(H,K,0)$ lowers notably with temperature.

It follows from the momentum conservation that an absorbed infrared photon creates a triplet excitation with $\mathbf{k}$ equal to photon momentum, $\mathbf{k}\approx0$, and this is in the center of Brillouin zone. INS data[9,10] show no excitation at 9.65 meV in the center of the Brillouin zone that would correspond to the triplet excitation T_1, as seen in FIR spectra. A possible explanation to overcome this discrepancy with INS results is to consider zone folding. Doubling of the unit cell size in the c axis direction is consistent with FIR data, since then the energy of the back folded acoustic branch at $(H,K,0.1)$ point would coincide with the energy of T_1, see Fig. 6. Indeed, the triplet mode T_1 has a similar temperature dependence of its energy as the acoustic mode at k points equivalent (any integer value of H and K) to $(H,K,0.1)$. We conclude that a magnetic unit cell of $10c_{\text{chain}}$ is compatible with our results.

The triplet T_2 has an energy similar to the acoustic mode at $(H,K,0)$. In the folded zone picture, the $(H,K,0.1)$ point moves to the center of the Brillouin zone and is infrared active as well. Due to the experimental uncertainty of the INS experiment ($\sim$0.5 meV) and a similar temperature dependence of acoustic and optic modes at this energy ($\approx$11 meV), we cannot determine exactly whether the triplet T_2 belongs to the acoustic or the zone folded optic branch of excitations, as seen by INS. However, the k points equivalent to $(H,K,0)$ points of the acoustic excitation are closer in the energy scale to the triplet level T_2, as seen by FIR. Consequently, we assign triplet T_2 to the chain acoustic excitation branch (in INS notation) at $\mathbf{k}=0$ point in the momentum space and refine the spin gap value for this point to 10.86 meV (87.7 cm^{-1}).

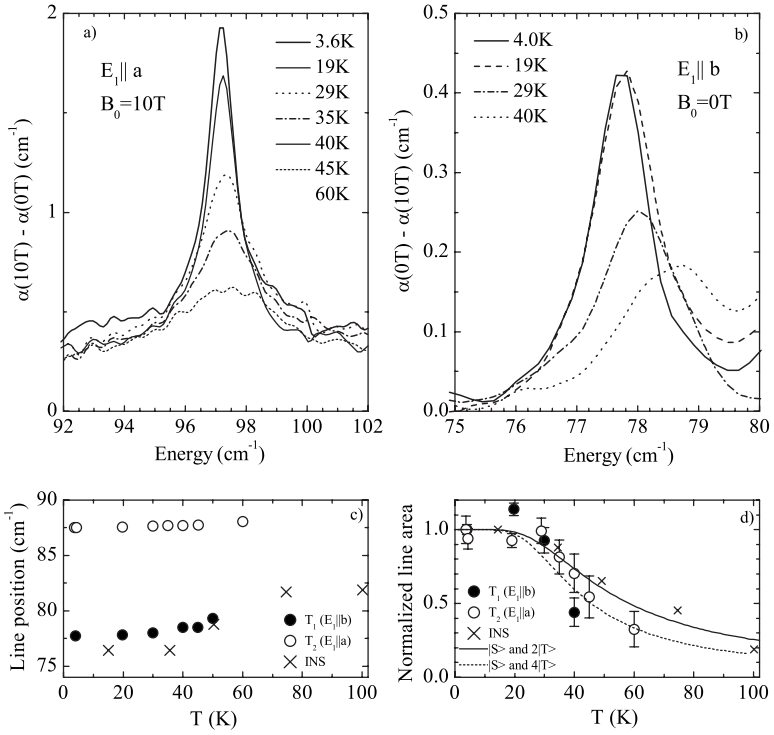

FIG. 5. Temperature dependence of triplet modes: (a) $T_2(+)$ in 10 T field, (b) T_1 in zero magnetic field, (c) line positions, and (d) observed normalized transition intensities; calculated singlet-triplet transition line area assuming two triplets (solid line) or four triplets in the folded zone structure (dashed line). The INS data, Ref. 9, are at $\mathbf{k}=(2,0,-0.1)$.

The T dependence of intensity of the observed FIR transitions, I, is proportional to the population difference of singlet and triplet levels if we assume that the transition matrix element is independent of temperature. Following the Boltzmann distribution, we get $I \sim [1-\exp(-\Delta/kT)]/[1+3N\exp(-\Delta/k_BT)]$, where N is the number of triplet states, each threefold degenerate, and Δ is the singlet-triplet energy gap; we used an averaged value $\Delta=11$ meV for all triplets. The solid line [Fig. 5(d)] indicates the calculated normalized transition intensity for a system with two triplet states and the dashed line for four triplet states in the new folded zone structure. Theoretical curves qualitatively explain the decrease in intensity. As the lines broaden with temperature, the determination of line area becomes less accurate, and thus T dependence of intensity cannot distinguish whether two or four triplet states exist.

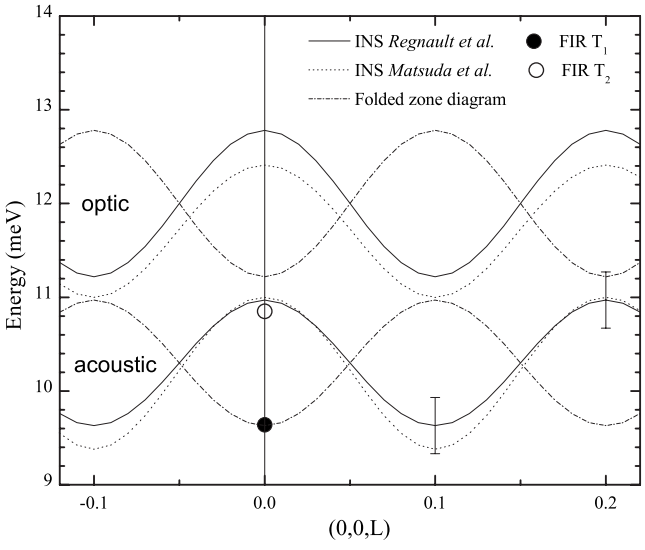

FIG. 6. Dispersion curves of the magnetic excitations in the chains (Refs. 9 and 10) and the observed triplet modes from FIR. The dash-dotted lines are extra dispersion curves, derived from data by *Regnault et al.* (Ref. 10), after doubling the unit cell in the c axis direction. INS energy resolution is shown by error bars; FIR transitions have linewidth less than the size of experimental points on the graph.

In the FIR, we observed two distinct magnetic signals at 4 K; firstly, the transitions from the singlet ground state to triplet states T_1 and T_2 and, secondly, a paramagnetic signal. It is not expected that the paramagnetic response at 4 K originates from a thermally excited triplet state in the chains due to a large spin gap, $\Delta \approx 11$ meV. There is evidence from susceptibility and electron spin resonance (ESR) measurements that unpaired spins exist in $Sr_{14}Cu_{24}O_{41}$. The g factor of the paramagnetic signal, $g_c=2.038\pm0.016$, obtained from our experiments matches that of ESR, $g_c(4\text{ K})=2.038$ at 4 K.[24] Above 20 K when the triplets are thermally populated, the ESR detects transitions between triplet levels $M_S=\pm1$ and $M_S=0$. The g factors of both triplets measured in FIR, $g_{1c}=2.049$ and $g_{2c}=2.044$, coincide with the averaged value, $g_c(20\text{ K})=2.045$ from ESR.[6,23,24] FIR measurements confirm directly that unpaired spins have g_c similar to spin dimers g factors g_{1c} and g_{2c}. Similar g_c components of the g tensor suggest a common local environment, as was proposed in Ref. 24, for the triplet and the paramagnetic site magnetic moments. Unpaired spins are in chains, instead of ladders. Unpaired Cu^{2+} spins in the chain subsystem destroy the perfect charge order with $5c_{\text{chain}}$ periodicity and are in accord with the FIR active triplet T_1 which, as we discussed above, is a result of doubling of the unit cell.

At 20 K, the linewidths of the singlet to triplet transitions seen in FIR is about 200 times larger than the ESR

transitions,[23] $1\text{cm}^{-1}/200=5\times10^{-3}\text{cm}^{-1}\approx50$ Oe. The difference between the two experimental probes is that FIR transitions are across the spin gap while ESR transitions are within the triplet state. It is natural to assume that it is the distribution of spin gaps what makes the 200-fold increase of triplet linewidth in FIR spectroscopy compared to ESR linewidth. Indeed, theoretical calculations[20] have demonstrated that there is a substantial fluctuation, 8%, of intradimer exchange coupling, ~10 meV, which contributes the most to the size of the spin gap. This inhomogeneous distribution should give a Gaussian and not a Lorentzian line shape. However, there is interdimer exchange, ~1 meV, that reduces the effect of inhomogeneous broadening and restores the Lorentzian line shape, an effect similar to motional narrowing.

Now, we discuss selection rules of the observed singlet-triplet transitions. We have determined by measuring the crystals in different experimental geometries that both singlet-triplet transitions are electric dipole active. $\mathbf{E}_1\|\mathbf{b}$ polarized light excites the triplet state T_1 and $\mathbf{E}_1\|\mathbf{a}$ light promotes singlets to the T_2 triplet state. The electric field component of light cannot directly couple to a spin system. In order to explain our observations, we consider a spin-phonon coupling mechanism where light couples to a phonon mode that lowers the symmetry of the lattice and generates an antisymmetric Dzyaloshinskii-Moriya (DM) interaction which couples singlet and triplet states. This dynamic DM transition mechanism has been successful in describing observed electric dipole active transitions in $SrCu_2(BO_3)_2$ (Refs. 25 and 26) and α'-NaV_2O_5.[27]

There are several observations that suggest a dynamic DM interaction in spin chains of $Sr_{14}Cu_{24}O_{41}$. First is the dependence on the light polarization. The dynamic DM vector $\mathbf{D}_q$ is perpendicular to $\mathbf{E}_1$ and to the spin dimer axis that is the c axis in $Sr_{14}Cu_{24}O_{41}$. The triplet T_1 interacts with electric field vector of the light $\mathbf{E}_1\|\mathbf{b}$, and $\mathbf{D}_q$ is parallel to the a axis for this triplet. The triplet T_2 interacts with the polarization $\mathbf{E}_1\|\mathbf{a}$, and $\mathbf{D}_q$ is parallel to the b axis. The selection rules are (i) if $\mathbf{B}_0\|\mathbf{D}_q$ then the transition to $T(0)$ is allowed and (ii) if $\mathbf{B}_0\perp\mathbf{D}_q$ then transitions to $T(-)$ and to $T(+)$ are allowed. One can see from Figs. 1 and 2 that the selection rules are satisfied: $T(-)$ and $T(+)$ transitions are observed when $\mathbf{B}_0\|\mathbf{c}$, and selection rule (ii) is satisfied. Moreover, when the magnetic field was aligned along the b axis, then the $T_2(+)$ line disappeared in $\mathbf{E}_1\|\mathbf{a}$ geometry (Fig. 2). This behavior is consistent with the dynamic DM mechanism selection rule (i). Second is the dependence of transition intensities on magnetic field. According to Eq. (1), a shift in energy of the triplet level reduces (increases) the separation between the triplet level and the relevant phonon mode and increases (decreases) coupling between the triplet and phonon states. The magnetic field dependence of the intensity of the triplet T_1 excitation, Fig. 3(a), was fitted with singlet-triplet transition probabilities for the dynamic DM model using Eqs. (13) and (14) from Ref. 27:

$$|\langle T(-)|V|S\rangle|^2 = I_p\frac{(qD_q)^2(\hbar\omega_{ph})^2}{2[(\hbar\omega_{ph})^2-(\Delta-g\mu_BB_0)^2]^2},$$

$$|\langle T(+)|V|S\rangle|^2 = I_p\frac{(qD_q)^2(\hbar\omega_{ph})^2}{2[(\hbar\omega_{ph})^2-(\Delta+g\mu_BB_0)^2]^2}. \quad (1)$$

The spin gap value $\Delta=\Delta_1=77.8\ \text{cm}^{-1}$ and the g factor $g=g_c=2.049$ were fixed parameters; the phonon frequency ω_{ph} and $I_p(qD_q)^2$ were the fitting parameters. The fit converged to a phonon at $\omega_{ph}=94\pm0.3\ \text{cm}^{-1}$. A phonon has been detected at 95 cm^{-1} by reflectivity measurements. In order to determine whether this 95 cm^{-1} phonon is the driving force behind the dynamic DM interaction in this compound, normal mode calculations have to be performed. To our knowledge, this has not been done yet. Unfortunately, the limited B_0 range does not allow us to determine the dynamic DM-active a-axis optical phonon of T_2 triplet unambiguously.

V. CONCLUSIONS

We have reported the magnetic field and temperature dependence of two triplet modes in the chains of $Sr_{14}Cu_{24}O_{41}$ with zero field excitation energies $\Delta_1=77.8\ \text{cm}^{-1}$ and $\Delta_2=87.7\ \text{cm}^{-1}$ at 4 K. The triplet excitation at 77.8 cm^{-1} has not been observed before at the center of Brillouin zone. Hence, the presently accepted spin lattice model for the chains in $Sr_{14}Cu_{24}O_{41}$ is incomplete and must include a triplet excitation at 77.8 cm^{-1} at $\mathbf{k}=0$. We propose a back folding of the triplet branches (observed in INS) due to the doubling of the magnetic supercell from five to ten chain units. The determination of g factors for free spins and triplets gave additional evidence that unpaired spins are in the chains and therefore the five chain unit periodicity cannot be retained. Optical selection rules for the observed singlet-triplet transitions are consistent with the dynamic Dzyaloshinskii-Moriya transition mechanism.

ACKNOWLEDGMENTS

Support by Estonian Science Foundation Grants No. 4926, No. 5553, and No. 6138 is acknowledged. National High Magnetic Field Laboratory is supported by NSF Cooperative Agreement No. DMR-0084173, by the State of Florida, and by the DOE. D.H.'s visit to the NHMFL was supported by the Archimedes Foundation.

*dan@kbfi.ee

[1] E. M. McCarron, M. A. Subramanian, J. C. Calabrese, and R. L. Harlow, Mater. Res. Bull. **23**, 1355 (1988).

[2] T. Siegrist, L. F. Schneemeyer, S. A. Sunshine, J. V. Waszczak, and S. Roth, Mater. Res. Bull. **23**, 1429 (1988).

[3] M. Uehara, T. Nagata, J. Akimitsu, H. Takahashi, N. Mori, and K. Kinoshita, J. Phys. Soc. Jpn. **65**, 2764 (1996).

[4] T. Vuletic, B. Korin-Hamzic, T. Ivek, S. Tomic, B. P. G. M.

Dressel, and J. Akimitsu, Phys. Rep. **428**, 169 (2006).
[5] F. C. Zhang and T. M. Rice, Phys. Rev. B **37**, 3759 (1988).
[6] M. Matsuda and K. Katsumata, Phys. Rev. B **53**, 12201 (1996).
[7] S. A. Carter, B. Batlogg, R. J. Cava, J. J. Krajewski, W. F. Peck, Jr., and T. M. Rice, Phys. Rev. Lett. **77**, 1378 (1996).
[8] M. Takigawa, N. Motoyama, H. Eisaki, and S. Uchida, Phys. Rev. B **57**, 1124 (1998).
[9] M. Matsuda, T. Yosihama, K. Kakurai, and G. Shirane, Phys. Rev. B **59**, 1060 (1999).
[10] L. P. Regnault, J. P. Boucher, H. Moudden, J. E. Lorenzo, A. Hiess, U. Ammerahl, G. Dhalenne, and A. Revcolevschi, Phys. Rev. B **59**, 1055 (1999).
[11] R. S. Eccleston, M. Uehara, J. Akimitsu, H. Eisaki, N. Motoyama, and S.-I. Uchida, Phys. Rev. Lett. **81**, 1702 (1998).
[12] T. Fukuda, J. Mizuki, and M. Matsuda, Phys. Rev. B **66**, 012104 (2002).
[13] S. van Smaalen, Phys. Rev. B **67**, 026101 (2003).
[14] M. Braden, J. Etrillard, A. Gukasov, U. Ammerahl, and A. Revcolevschi, Phys. Rev. B **69**, 214426 (2004).
[15] J. Etrillard, M. Braden, A. Gukasov, U. Ammerahl, and A. Revcolevschi, Physica C **403**, 290 (2004).
[16] Y. Gotoh, I. Yamaguchi, Y. Takahashi, J. Akimoto, M. Goto, M. Onoda, H. Fujino, T. Nagata, and J. Akimitsu, Phys. Rev. B **68**, 224108 (2003).
[17] Y. Gotoh, I. Yamaguchi, H. Eisaki, T. Nagata, and J. Akimitsu, Physica C **445-448**, 107 (2006).
[18] M. Isobe, M. Onoda, T. Ohta, F. Izumi, K. Kimoto, E. Takayama-Muromachi, A. W. Hewat, and K. Ohoyama, Phys. Rev. B **62**, 11667 (2000).
[19] A. Gelle and M.-B. Lepetit, Phys. Rev. Lett. **92**, 236402 (2004).
[20] A. Gelle and M.-B. Lepetit, Eur. Phys. J. B **46**, 489 (2005).
[21] N. Nücker *et al.*, Phys. Rev. B **62**, 14384 (2000).
[22] T. Osafune, N. Motoyama, H. Eisaki, and S. Uchida, Phys. Rev. Lett. **78**, 1980 (1997).
[23] V. Kataev, K.-Y. Choi, M. Grüninger, U. Ammerahl, B. Büchner, A. Freimuth, and A. Revcolevschi, Phys. Rev. B **64**, 104422 (2001).
[24] R. Klingeler, B. Buchner, K.-Y. Choi, V. Kataev, U. Ammerahl, A. Revcolevschi, and J. Schnack, Phys. Rev. B **73**, 014426 (2006).
[25] O. Cepas and T. Ziman, Phys. Rev. B **70**, 024404 (2004).
[26] T. Rõõm, D. Hüvonen, U. Nagel, J. Hwang, T. Timusk, and H. Kageyama, Phys. Rev. B **70**, 144417 (2004).
[27] T. Rõõm, D. Hüvonen, U. Nagel, Y.-J. Wang, and R. K. Kremer, Phys. Rev. B **69**, 144410 (2004).

Far-infrared spectroscopy of spin excitations and Dzyaloshinskii-Moriya interactions in the Shastry-Sutherland compound $SrCu_2(BO_3)_2$

T. Rõõm,* D. Hüvonen, and U. Nagel
National Institute of Chemical Physics and Biophysics, Akadeemia tee 23, 12618 Tallinn, Estonia

J. Hwang and T. Timusk
Department of Physics and Astronomy, McMaster University, Hamilton, Ontario L8S4M1, Canada

H. Kageyama
Department of Chemistry, Graduate School of Science, Kyoto University, Kyoto, 606-8502, Japan
(Received 30 March 2004; published 27 October 2004)

We have studied spin excitation spectra in the Shastry-Sutherland model compound $SrCu_2(BO_3)_2$ in magnetic fields using far-infrared Fourier spectroscopy. The transitions from the ground singlet state to the triplet state at 24 cm^{-1} and to several bound triplet states are induced by the electric field component of the far-infrared light. To explain the light absorption in the spin system we invoke a dynamic Dzyaloshinskii-Moriya (DM) mechanism where light couples to a phonon mode, allowing the DM interaction. Two optical phonons couple light to the singlet to triplet transition in $SrCu_2(BO_3)_2$. One is *a*-polarized and creates an intradimer dynamic DM along the *c* axis. The other is *c*-polarized and creates an intradimer dynamic DM interaction, it is in the (*ab*) plane and perpendicular to the dimer axis. Singlet levels at 21.5 and 28.6 cm^{-1} anticross with the first triplet as is seen in far-infrared spectra. We used a cluster of two dimers with a periodic boundary condition to perform a model calculation with scaled intra- and interdimer exchange interactions. Two static DM interactions are sufficient to describe the observed triplet state spectra. The static interdimer DM in the *c*-direction $d_1=0.7$ cm^{-1} splits the triplet state sublevels in zero field [Cépas *et al.*, Phys. Rev. Lett. **87**, 167205 (2001)]. The static intradimer DM in the (*ab*) plane (perpendicular to the dimer axis) $d_2=1.8$ cm^{-1}, allowed by the buckling of $CuBO_3$ planes, couples the triplet state to the 28.6 cm^{-1} singlet as is seen from the avoided crossing.

DOI: 10.1103/PhysRevB.70.144417 PACS number(s): 75.10.Jm, 78.30.Hv, 71.70.Gm, 76.30.Fc

I. INTRODUCTION

In spin systems with a ground singlet state and excited triplet state the energy gap between the singlet and the triplet can be tuned with an external magnetic field. In $SrCu_2(BO_3)_2$ it was discovered that in magnetic fields above 22 T, where the spin gap is expected to close, several magnetization plateaus appear.[1] At magnetization plateaus the triplets form a pattern which breaks the translational symmetry of the crystal structure.[2] The heavy mass of the triplet excitations arising from an almost flat dispersion of energy on momentum[3] favors the build-up of magnetic superstructures. Below the critical field $SrCu_2(BO_3)_2$ has a ground state described first by Shastry and Sutherland.[4]

$SrCu_2(BO_3)_2$ consists of planes of $CuBO_3$ and Sr atoms between the planes. Cu^{2+} spins ($S=1/2$) form Cu-Cu dimers arranged into orthogonal dimer network. $SrCu_2(BO_3)_2$ is an experimental realization of a Shastry-Sutherland model.[4] In the model there is an antiferromagnetic intradimer exchange coupling j_1 and interdimer coupling j_2 between spins on the nearest-neighbor dimers (Fig. 1). In the limit of $\alpha \equiv j_2/j_1 = 0$ the problem reduces to that of isolated dimers where the ground state is the product of singlet states and the first excited triplet state is at energy $\Delta_T = j_1$ above the ground state, where Δ_T is the energy per dimer. Shastry and Sutherland showed that for $0 < \alpha \leqslant 0.5$ singlets on all dimers is an exact ground state too. The exactness of the ground state and the heavy mass of triplet excitations is the consequence of frustration originating from the special geometry of the dimer lattice in the Shastry-Sutherland model where the bonds on neighboring dimers are orthogonal. Later on it has been shown that singlets on all dimers is the exact ground state for a larger range of α up to the quantum critical point $\alpha_c \approx 0.7$. At the quantum critical point the spin gap vanishes and a long-range antiferromagnetic order is established. Different theoretical approaches have been used to calculate α_c (see Ref. 5 for review). It is possible that between the exact singlet ground state and the anti-ferromagnetic state in certain range of α other gapped spin states exist.[6–11]

The singlet-triplet gap in $SrCu_2(BO_3)_2$, $\Delta_T = 24$ cm^{-1}, has been measured directly by several experimental techniques: inelastic neutron scattering,[3,12] electron spin resonance[13,14] (ESR), Raman scattering,[15] and far-infrared (FIR) spectroscopy.[16] Additional information besides Δ_T is needed to determine the exchange parameters of $SrCu_2(BO_3)_2$. The dispersion of the triplet excitation is not informative because of its flatness,[3] but positions of other excited states or the temperature dependence of thermodynamic parameters can be used for determining the exchange parameters. Miyahara and Ueda[5] found $j_1 = 59$ cm^{-1} and $\alpha = 0.635$. They added an interlayer coupling $j_3 = 0.09 j_1$ to the model to obtain a better fit of the magnetization *T*-dependence above the critical temperature $k_B T > \Delta_T$. Based on the analysis of excitation spectra[17] $j_1 = 50$ cm^{-1} and $\alpha = 0.603$ were proposed. Such

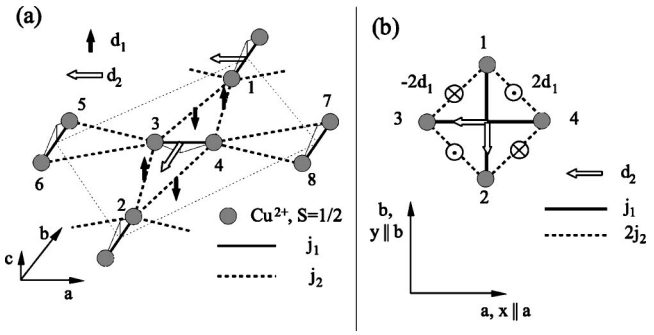

FIG. 1. Cluster with two dimers (1,2) and (3,4). (a) Dimer (3,4) and four nearest-neighbor dimers. The thin dashed line shows the two dimer cluster boundary. Thin solid lines show the distortion of Cu-Cu superexchange bonds due to the buckling of Cu-O-B planes. Thick solid and dashed lines are the inter- and intradimer superexchange constants j_1 and j_2; interdimer DM vectors ($\mathbf{d}_1$, solid arrow) are in the c direction and intradimer DM vectors ($\mathbf{d}_2$, empty arrow) in the (ab) plane along a and b axis. (b) The two dimer model after the periodic boundary condition has been applied; interdimer interactions have doubled.

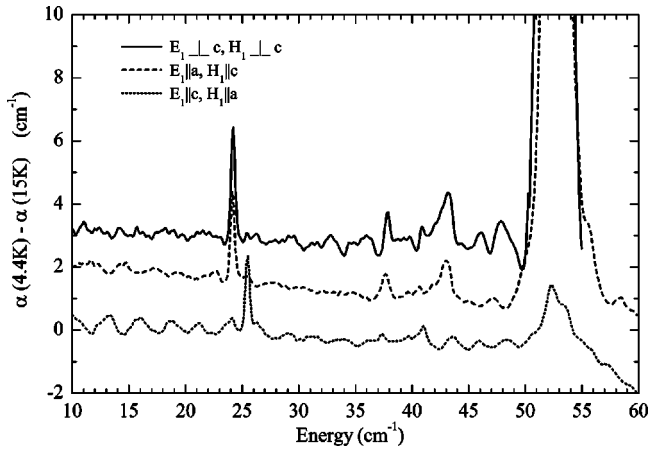

FIG. 2. Differential absorption in $\mathbf{E}_1 \perp \mathbf{c}$ (two upper curves) and $\mathbf{E}_1 \| \mathbf{c}$ (lower curve) polarization. Spectra have been offset in the vertical direction.

scattering of parameters could be either due to the incomplete model or due to the approximations made in theoretical calculations. $SrCu_2(BO_3)_2$ is near to the quantum critical point α_c where the energy levels of the spin system are sensitive to the choice of j_1 and α. A singlet level in the spin gap at 21 cm^{-1} found in the ESR spectra[14] may help to find proper parameters for the model.

Interactions other than inter- and intradimer exchange coupling can spoil the exactness of the ground state. This is important in high magnetic fields where the triplet state becomes degenerate with the ground singlet state. At this critical field even a weak interaction between the singlet and the triplet state mixes the two states completely. The singlet and triplet state anticrossing effects were seen in the high field ESR experiments.[14] A possible antisymmetric interaction which couples the singlet and the triplet states is the DM interaction. An intradimer DM is allowed by symmetry but its strength is not known below room temperature. Above room temperature $d_2 = 2.5$ cm^{-1} has been estimated from the ESR linewidth.[18] The interdimer DM interaction, $d_1 = 1.5$ cm^{-1}, perpendicular to the dimer planes[12] partially lifts the degeneracy of the triplet state but does not couple the triplet state to the singlet state. The effect of DM interactions on the magnetic dipole active ESR transitions in $SrCu_2(BO_3)_2$ was investigated theoretically in Ref. 19.

Lattice distortions, static or dynamic, are important in $SrCu_2(BO_3)_2$ since they lower the crystal symmetry and allow magnetic interactions which are otherwise forbidden in a more symmetric environment. $SrCu_2(BO_3)_2$ has a structural phase transition at 395 K (Ref. 20) that induces a buckling of $CuBO_3$ planes in the low T phase. As the phase transition point is approached from below the Raman-active 62 cm^{-1} optical phonon mode softens.[21] Acoustic phonon modes have spin-phonon coupling at magnetization plateaus.[22] It has been proposed that a spin superstructure at $1/8$ plateau observed by nuclear magnetic resonance at 35 mK is stabilized by a lattice distortion.[2] Instantaneous breaking of lattice symmetry by an optical phonon allows electric dipole active singlet-triplet transitions[23] that explains FIR polarized absorption spectra in $SrCu_2(BO_3)_2$.[16]

Our aim is to find out which additional interactions are required to the Shastry-Sutherland model that add triplet corrections to the ground state. For that we do FIR absorption measurements with polarized light in magnetic field and compare the absorption line frequencies and intensities with values calculated with a two dimer model including the dynamic DM effect. The important information is in the polarization and magnetic field dependence of the FIR absorption lines and in the avoided crossing effects.

We studied single crystals of $SrCu_2(BO_3)_2$, Ref. 24. The first sample consisted of two pieces 0.65 mm thick in the a-direction with the total area of 12 mm^2 in the (ac) plane. The second sample was 0.6 mm thick in the c-direction and had an area of 11.5 mm^2 in the (ab) plane. The experimental details are described in Refs. 16 and 25.

II. RESULTS AND DISCUSSION

A. FIR spectra and electric dipole transitions

As the result of the polarization sensitive measurement of FIR spectra we have identified that the main resonances in the spectra are electric dipole transitions, rather than being magnetic dipole transitions. In Fig. 2 differential absorption spectra at 4.4 K relative to 15 K, are displayed. The strong absorption lines at 52.3 and 53.5 cm^{-1} were identified[16] as electric dipole transitions, that are active in $\mathbf{E}_1 \| \mathbf{a}$ polarization. We see the same for the 43.0 cm^{-1} singlet and T_0 and T_1 triplets (see Table I) at 24.2 and 37.5 cm^{-1}, respectively, which are present in the spectra measured with $\mathbf{E}_1 \| \mathbf{a}$ regardless of $\mathbf{H}_1$ being perpendicular to the c axis or parallel to it. The lines are missing in $\mathbf{E}_1 \| \mathbf{c}$ polarization,[26] instead a new line appears at 25.5 cm^{-1}, which is identified as another component of the triplet T_0.

The triplets are split by the magnetic field $\mathbf{B}_0$. Differential absorption spectra in $\mathbf{E}_1 \| \mathbf{a}$ polarization for one magnetic field direction, $\mathbf{B}_0 \| \mathbf{a}$, measured relative to the zero field, are

TABLE I. Singlet and triplet excitations observed in the FIR spectra at 4.4 K in the order of increasing zero field energies $\hbar\omega_0$ (in cm^{-1} units). When a line is visible in two $\mathbf{E}_1$ polarizations, both are indicated. The corresponding $\mathbf{H}_1$ polarizations are also indicated. *S* and *T* label the singlet and triplet states; + (−) denotes levels which energy increases (decreases) with $\mathbf{B}_0$ and 0 indicates levels where the energy stays constant; g_a and g_c are the *g*-factors with $\mathbf{B}_0\|\mathbf{a}$ and $\mathbf{B}_0\|\mathbf{c}$, respectively. The labeling of T_0 levels is shown in Fig. 5. The zero field intensities A_0 (in cm^{-2} units) of T_0 (⋆) are described in the text and in Figs. 4–6. High energy excitations are labeled by their energies.

Label	$\mathbf{E}_1$	$\mathbf{H}_1$	A_0	$\hbar\omega_0$	g_a	g_c
S_1	*a*	*c*		21.50±0.03		
$T_{0m}(\pm)$	*a*,*c*	*c*,*a*	⋆	22.72±0.05	1.988	2.219
$T_{0p,m}(0)$	*a*,*c*	*c*,*a*	⋆	24.11±0.05		
$T_{0p}(\pm)$	*a*,*c*	*c*,*a*	⋆	25.51±0.05	1.988	2.219
S_2	*a*,*c*	*c*,*a*		28.57±0.03		
$T_1(\pm)$	*c*	*a*	0.3±0.2	37.49±0.03	1.996	2.264
$T_1(\pm)$	*a*	*b*,*c*	0.9±0.2	37.51±0.04	2.001	2.23
$T_1(0)$	*a*	*c*	0.9±0.2	37.69±0.09		
$T_{38.7}(\pm)$	*a*	*c*		38.74±0.03	2.026	
$T_{38.7}(0)$	*c*	*a*		38.70±0.15		
$T_{39.1}(\pm)$	*c*	*a*		39.08±0.15	2.067	2.29
$S_{39.7}$	*a*	*c*	0.19±0.05	39.71±0.04		
$T_{40.5}(\pm)$	*a*	*c*		40.45±0.03	1.97	
$T_{40.7}(\pm)$	*c*	*a*	0.2±0.1	40.67±0.03		2.243
$T_{40.7}(0)$	*a*,*c*	*c*,*a*	0.2±0.1	40.70±0.16		
$T_{41.1}(\ )$	*c*	*a*	0.4±0.1	41.11±0.13	2.10	
$T_{42.7}(+)$	*a*	*c*	0.2±0.1	42.7±0.2		2.25
S_{43}	*a*	*b*,*c*	2.6±0.3	43.00±0.16		
$T_{43.5}(\pm)$	*c*	*a*	0.2±0.1	43.54±0.03		2.31
$S_{44.7}$	*c*	*a*		44.7±0.4		
$S_{47.0}$	*c*	*a*		47.04±0.04		
$T_{48.2}(\pm)$	*c*	*a*	0.04±0.02	48.21±0.09		2.27
$S_{52.3}$	*a*	*b*,*c*	86±14	52.24±0.08		
$S_{53.5}$	*a*	*b*,*c*	24±3	53.44±0.07		

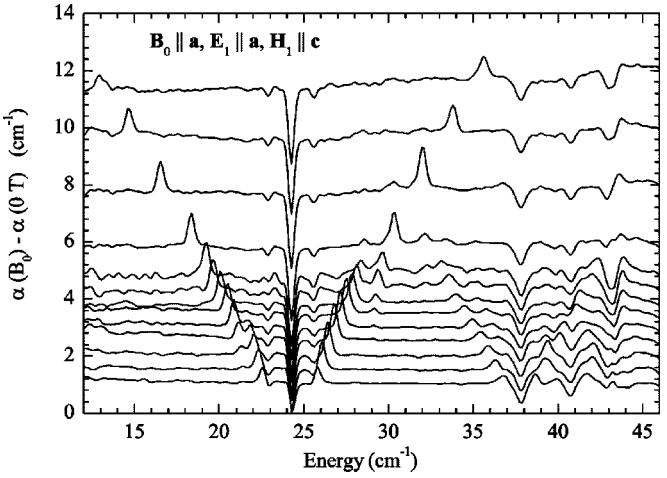

FIG. 3. Differential absorption spectra in magnetic field $\mathbf{B}_0\|\mathbf{a}$ at 4.4 K. Vertical offset equals the magnetic field value in Tesla.

displayed in Fig. 3. We see an anticrossing of the $T_{0m}(-)$ level with the singlet S_1 at 21.5 cm^{-1} and an anticrossing of the $T_{0p}(+)$ level with the singlet S_2 at 28.6 cm^{-1}. All the peaks in the measured spectra in different light polarizations and $\mathbf{B}_0$ directions were fitted with Lorentzians. The results are summarized in Table I and displayed in Figs. 4–6. The states above 38 cm^{-1} are labeled by their zero field frequencies. The magnetic field independent energy levels are labeled as singlets with the exception of those in the middle of the triplet levels $T(\pm)$.

B. Dynamic Dzyaloshinskii-Moriya mechanism and optical transitions: Two dimers

The Hamiltonian for a spin pair with exchange coupling *j* and DM interaction **d** on the bond connecting spins *k* and *l* reads

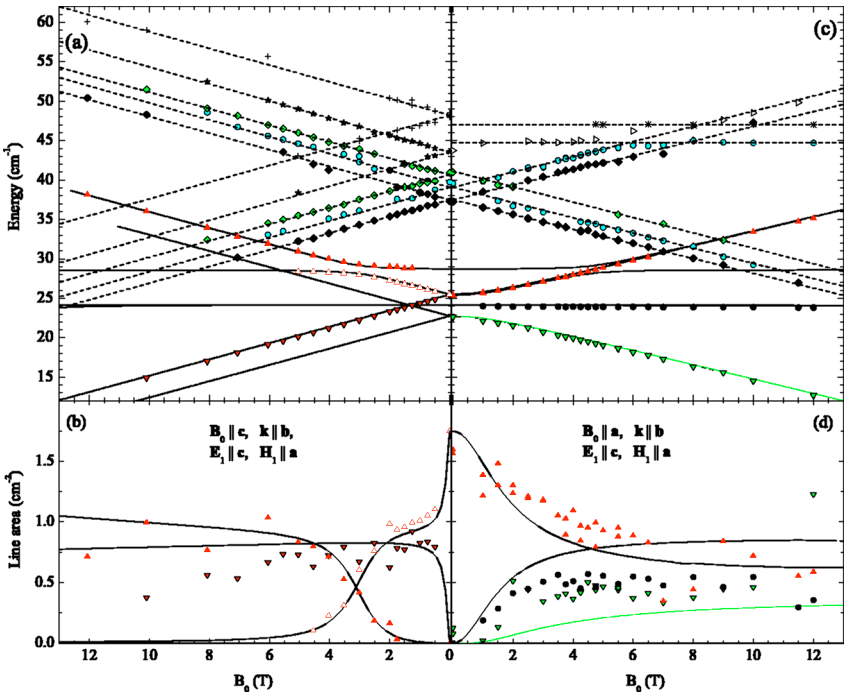

FIG. 4. (Color online) Magnetic field dependence of line positions and line areas in $\mathbf{E}_1\|\mathbf{c}$ polarization at 4.4 K; (a), (b) $\mathbf{B}_0\|\mathbf{c}$; (c), (d) $\mathbf{B}_0\|\mathbf{a}$. Solid lines are the results of the calculation based on the two dimer model: $j_1 = 24$ cm^{-1}, $2j_2 = 9.8$ cm^{-1}, $2d_1 = 1.4$ cm^{-1}, and $d_2 = 1.8$ cm^{-1}. Dashed lines in panels (a) and (c) are fits with parameters given in Table I.

$$H^{kl}_{\text{stat}} = \left(j - \frac{|\mathbf{d}|^2}{4j}\right)\mathbf{S}_k \cdot \mathbf{S}_l + \frac{1}{2j}\mathbf{S}_k \cdot \mathbf{d}\mathbf{d} \cdot \mathbf{S}_l + \mathbf{d} \cdot [\mathbf{S}_k \times \mathbf{S}_l] + g\mu_B \mathbf{B}_0 \cdot (\mathbf{S}_k + \mathbf{S}_l). \quad (1)$$

Here we included Shekhtman corrections[27,28] which are quadratic in $\mathbf{d}$ (see also Ref. 25). The last term is the Zeeman energy of spins in the magnetic field $\mathbf{B}_0$ where g is the electron spin g-factor and μ_B is the Bohr magneton.

The formalism to introduce the spin-phonon coupling is similar to one used in Refs. 23 and 25. We are interested in singlet to triplet transitions. Therefore the relevant term is the antisymmetric DM interaction $\mathbf{d}(Q)\cdot[\mathbf{S}_k \times \mathbf{S}_l]$ which couples the singlet to the triplet state. We expand the DM vector $\mathbf{d}(Q)$ into a power series of the lattice normal coordinate Q

$$\mathbf{d}(Q) = \mathbf{d}(0) + \left.\frac{\partial \mathbf{d}}{\partial Q}\right|_{Q=0} Q + \ldots, \quad (2)$$

where $\mathbf{d}(0) \equiv \mathbf{d}$ is the static DM interaction in (1). We keep terms linear in Q. The full Hamiltonian for a spin pair including the phonons is

$$H^{kl} = H^{kl}_{\text{stat}} + \hbar\omega_p a^\dagger a + q(a^\dagger + a)\mathbf{d}_Q \cdot [\mathbf{S}_k \times \mathbf{S}_l], \quad (3)$$

where $\mathbf{d}_Q \equiv \partial \mathbf{d}/\partial Q|_{Q=0}$. The lattice normal coordinate Q is presented in terms of phonon creation and annihilation operators $a^\dagger$ and a, $Q = q(a^\dagger + a)$, where q is the transformation coefficient and ω_p is the phonon frequency. The spin-phonon coupling term in (3) is linear in $a^\dagger$ and a. Therefore the phonon states with the occupation numbers n and n' are coupled where $n' = n \pm 1$. We will consider only two phonon states $|0\rangle$ and $|1\rangle$, which is justified when $k_B T \ll \hbar\omega_p$.

The normal coordinate Q in the dynamic DM singlet to triplet optical transition mechanism belongs to an optical phonon. Electric dipole coupling between a phonon and light in the long wavelength limit is

$$V = eQE_1 = eq(a^\dagger + a)E_1, \quad (4)$$

where e is the effective charge associated with the lattice normal coordinate Q. Here we assumed $\mathbf{E}_1\|\mathbf{Q}$ and dropped the time dependence of V. Once the eigenstates of (3) are known the optical transition probability between the ground state $|\phi\rangle$ and the excited state $|\phi'\rangle$ is calculated as $I = |\langle\phi'|V|\phi\rangle|^2$.

To calculate optical transitions in $SrCu_2(BO_3)_2$ we use a two dimer model depicted in Fig. 1. In this model intradimer and interdimer superexchange interactions j_1 and j_2 are considered. The interdimer static DM vector $\mathbf{d}_1$ is along the c axis and alternates from bond to bond. The intradimer static DM vector $\mathbf{d}_2$ exists due to the buckling of Cu-O-B planes.[20] The direction of DM vectors is defined by the right-hand rule where the path is along the Cu-O-Cu bond (for $\mathbf{d}_1$ Cu-O-B-O-Cu) in the direction of increasing spin index k. In the vector product $\mathbf{S}_k \times \mathbf{S}_l$ the spin with a smaller index is on the left, $k < l$. When a periodic boundary condition is applied to the two dimer cluster, bounded by a box drawn with a thin dashed line in Fig. 1(a), an effective spin model is obtained where the interdimer interactions are doubled, Fig. 1(b). The doubling is necessary to conserve the number of next-nearest-neighbor bonds, which is four.

The Hamiltonian for the two dimer cluster is the sum of pairwise interactions (3) where the sum runs over all the bonds in the cluster. We will use a basis $|ABn\rangle$, where A runs over the singlet S and three triplet components T_-, T_0, and T_+ on the j_1 bond of the dimer (1,2) and B over the singlet and triplet states of the dimer (3,4). n is the number of phonons, 0 or 1. The basis has 32 components. Below we consider a- and c-axis phonons, shown in Fig. 7, named by the direction of their electric dipole moment.

1. Energy levels

The effect of the dynamic DM interaction on the position of energy levels is small because we take $\hbar\omega_p = 100$ cm^{-1}

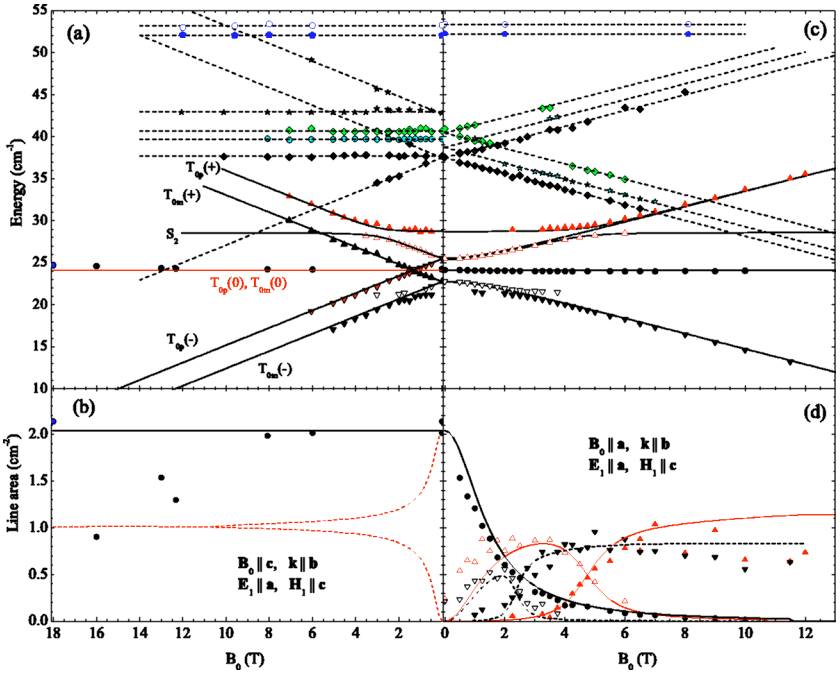

FIG. 5. (Color online) Magnetic field dependence of line positions and line areas in $\mathbf{E}_1\|\mathbf{a}$ polarization at 4.4 K; (a), (b) $\mathbf{B}_0\|\mathbf{c}$; (c), (d) $\mathbf{B}_0\|\mathbf{a}$. Solid lines are the results of the calculation based on the two dimer model: $j_1=24$ cm^{-1}, $2j_2=9.8$ cm^{-1}, $2d_1=1.4$ cm^{-1}, and $d_2=1.8$ cm^{-1}. Dashed lines in panels (a) and (c) are fits with parameters given in Table I. The solid line in panel (b) is the sum of two theoretical line areas of S_0 to $T_{0m}(0)$ and to $T_{0p}(0)$ transitions shown by dashed lines. Dashed lines in (d) are eye guides (see text). The 18 T point a panels (a) and (b) was measured at 1.8 K.

that is substantially larger than the singlet-triplet gap. We use this value since there are no optical phonons with substantial spectral weight below 100 cm^{-1} as our transmission measurements show. The energy spectrum can be analyzed separately from the dynamic DM effect because of the high phonon energy. The calculated energy levels are the same in Figs. 4 and 5. In these figures only the zero phonon levels of the triplet T_0 and S_2 are shown. The levels with one excited phonon are offset by $\hbar\omega_p$ to higher energies and are not shown.

In a two dimer system two singlets, two triplets, and a quintet are present. The ground state is a product of singlets $|SS\rangle$. The first triplet is a linear combination of $|ST\rangle$ and $|TS\rangle$. In the two dimer model the singlet-triplet splitting is not renormalized by the interdimer coupling j_2 and the energy of the triplet excitation is $E_{T0}=j_1$. The second singlet, a bound state of two triplets, is at $E_{S1}=2j_1-2(2j_2)$. To stress the fact that in the two dimer model with a periodic boundary condition the interdimer bonds are effectively doubled, we write $2j_2$ explicitly. There are two other bound states of two triplets, a triplet at $E_{T1}=2j_1-(2j_2)$ and a quintet at $E_Q=2j_1+(2j_2)$. These energies and the ground state wave function are slightly changed by the static DM interactions d_1 and d_2. The spin states $|ST_i\rangle$ and $|T_iS\rangle$ are strongly mixed by the interdimer d_1 since they are degenerate in any field.

The states are labeled in Fig. 5. The following parameters were used to fit the energy spectra plotted in Figs. 4 and 5. The energy of one-triplet sublevels $T_{0m}(0)$ and $T_{0p}(0)$ gives us $j_1=24.0$ cm^{-1}. To get the singlet S_2 at 28.6 cm^{-1} we use $2j_2=9.8$ cm^{-1}. Triplet levels are split in zero field by $2d_1=1.4$ cm^{-1}. The intradimer $d_2=1.8$ cm^{-1} induces an avoided crossing of $T_{0p}(+)$ and S_2. In a simplified picture the one-triplet excitation is the $|ST\rangle$ (or $|TS\rangle$) state and the excited singlet is $|TT\rangle$. d_2 "flips" the singlet to the triplet state on one of the dimers and thus couples $T_{0p}(+)$ to S_2.

2. c-axis phonon

The optical *c*-axis phonon bends the Cu-O-Cu bond in the *c*-direction. We assume that the bending action of the phonon is the same on both dimers, Fig. 7. As a result the dynamic DM interaction on the dimer (1,2) is $q_c\mathbf{d}_{Q_c}\equiv\mathbf{d}_{3c}=(-d_{3c},0,0)$ and on the dimer (3,4) $\mathbf{d}_{3c}=(0,d_{3c},0)$; the orientation of the Cartesian coordinates is the same as in Fig. 1(b). The calculated and the measured transition probabilities as a function of magnetic field are plotted in Figs. 4(b) and 4(d) for two field orientations. In zero field a line at 25.5 cm^{-1} is present. The area of this line is the only scaling parameter between the theory and the experiment. Note that the transition to the triplet level, which anticrosses with S_2, is optically active when $\mathbf{B}_0\|\mathbf{c}$. When $\mathbf{B}_0\|\mathbf{a}$ there is no anticrossing for the optically active triplet level.

The overall agreement between the theory and the experiment is good. There is a disagreement between the intensities of the middle and lower triplet components in the theory and in the experiment, Fig. 4(d). In the theory the intensity of the middle component is approximately three times as strong as the lower component while in the experiment they are equal. We tried several changes in our model to make the intensities of the two triplet components more equal and none of them helped. These unfruitful changes were the shift of the phonon frequency, a small out-of-plane component of $\mathbf{B}_0$ and an in-plane component of the interdimer DM vector $\mathbf{d}_1$.

3. a-axis phonon

The optical *a*-axis phonon bends the Cu-O-Cu bond in the a-direction and creates a dynamic DM interaction in the c-direction, Fig. 7. If we choose $\mathbf{E}_1\|\mathbf{a}$ the dynamic DM interaction is created on dimer (1,2), $q_a\mathbf{d}_{Q_a}\equiv\mathbf{d}_{3a}=(0,0,d_{3a})$. In general, for an arbitrary orientation of $\mathbf{E}_1$ in the (ab) plane, both dimers will acquire a certain $\mathbf{d}_{3a}$. For the time being we assume $\mathbf{E}_1\|\mathbf{a}$.

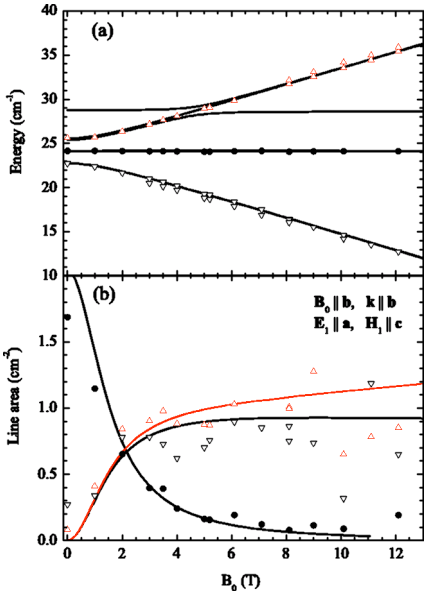

FIG. 6. (Color online) Line positions (a) and line areas (b) in $\mathbf{E}_1\|\mathbf{a}$ and $\mathbf{B}_0\|\mathbf{b}$ configuration at 4.4 K. The lines are results of the calculation based on the two dimer model and dynamic DM interaction. The additional splitting of triplet components (triangles) is caused by the magnetic field $\mathbf{B}_0$ being misaligned by 9° out of the (*ab*) plane (Ref. 26). In panel (b) the line area (triangles up or triangles down) is a sum of line areas of split components.

In zero magnetic field the transition to the central triplet component is observed, Fig. 2. As the $\mathbf{B}_0\|\mathbf{c}$ field is turned on, Fig. 5(b), the central line, being a sum of two overlapping transitions, conserves its intensity. The experimentally observed drop in intensity with increasing field is a *T* effect. At 1.8 K (18 T field) the intensity is recovered. Besides the strong central line there are in zero field two sidepeaks ten times weaker at 22.7 and 25.5 cm^{-1} corresponding to transitions to the twice degenerate states $T_{0m}(\pm)$ and $T_{0p}(\pm)$. The dynamic DM interactions due to the *a*- and *c*-axis phonons in this $\mathbf{B}_0$ orientation give zero intensity for the sidepeaks. The detailed analysis of the mechanism causing these weak transitions is difficult because in other polarizations and field orientations stronger mechanisms are prevailing. The sidepeaks split in the magnetic field and an avoided crossing with S_1 and S_2 is seen in the experiment.

When the magnetic field is in the (*ab*) plane two cases must be considered, $\mathbf{B}_0\|\mathbf{E}_1$ and $\mathbf{B}_0\perp\mathbf{E}_1$. In Figs. 5(c) and

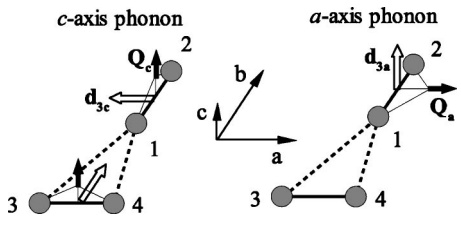

FIG. 7. Intradimer dynamic DM interactions. A lattice distortion with the normal coordinate **Q** (solid arrow) creates an intradimer DM interaction $\mathbf{d}_3$ (empty arrow). The *c*-axis phonon creates a dynamic DM interaction on both dimers while the *a*-axis phonon affects the dimer (1,2) only.

5(d) the $\mathbf{B}_0\|\mathbf{E}_1$ case is shown. Here are optically active the triplet levels which anticross with the singlet states. In $\mathbf{B}_0\perp\mathbf{E}_1$ field orientation, Fig. 6, the optically active triplet levels do not anticross with the singlet states. The mutual orientation of $\mathbf{B}_0$ and $\mathbf{E}_1$ is important because $\mathbf{E}_1\|\mathbf{a}$ creates $\mathbf{d}_{3a}$ on the dimer (1,2) and not on (3,4). Which set of the twofold degenerate triplet levels is optically active depends on the relative orientation of $\mathbf{B}_0$ and $\mathbf{d}_2$ on the dimer where $d_{3a}\neq 0$. In Fig. 5, $\mathbf{B}_0\|\mathbf{d}_2$ and in Fig. 6, $\mathbf{B}_0\perp\mathbf{d}_2$. An additional splitting of $T_{0m}(\pm)$ and $T_{0p}(\pm)$ by 0.6 cm^{-1} seen in Fig. 6 is because $\mathbf{B}_0$ is out of (*ab*) plane by 9°.

C. Static and dynamic DM in $SrCu_2(BO_3)_2$

We have shown that the first triplet state energy spectra are well described with two static DM interactions, $\mathbf{d}_1$ and $\mathbf{d}_2$. The information about $\mathbf{d}_1$ and $\mathbf{d}_2$ is contained in the position of energy levels and in the FIR absorption line intensities. The interdimer $\mathbf{d}_1$ determines the magnetic field dependence of intensities and the triplet state level energy splitting. The intradimer $\mathbf{d}_2$ determines the extent of the avoided crossing with S_2 and the magnetic field dependence of intensities near the avoided crossing points. Over the magnetic field range of our experiment the intensities of the singlet-triplet absorption lines do not depend on the dynamic part of the DM interaction, because the phonon energies are large compared to the triplet state energy.

Other inter- and intradimer DM interaction components besides $\mathbf{d}_1$ and $\mathbf{d}_2$ have been considered to describe experimental data.[18,29] These are the in-plane component of the interdimer DM $\mathbf{d}_{xy}$ and the symmetry-forbidden intradimer DM $\mathbf{d}_z$ in the *c*-direction. We included $\mathbf{d}_{xy}$ and $\mathbf{d}_z$ in the two dimer model and found that calculations with nonzero $\mathbf{d}_{xy}$ and $\mathbf{d}_z$ give results contradicting with the experiment. Our argument, which is independent of whether a particular infrared transition is allowed or forbidden, relies on the observed and calculated crossing-anticrossing effects between the triplet and the singlet states.

If $\mathbf{B}_0\|\mathbf{c}$ and $\mathbf{d}_{xy}\neq 0$ then $T_{0m}(+)$ would have an avoided crossing with S_2 contradicting the experiment, where $T_{0p}(+)$ anticrosses with the singlet [Fig. 5(a)]. Also $\mathbf{d}_z$ does not give any anticrossing between S_2 and $T_{0m}(+)$ or $T_{0p}(+)$. In high field nonzero $\mathbf{d}_2$ creates an avoided crossing between the ground state S_0 and the triplet branch $T_{0m}(-)$ as observed in the experiment[14] while nonzero $\mathbf{d}_{xy}$ or $\mathbf{d}_z$ do not create an avoided crossing between S_0 and $T_{0m}(-)$ or $T_{0p}(-)$. However, the two dimer model does not predict the experimentally observed[14] avoided crossing between S_0 and $T_{0p}(-)$.

In $\mathbf{B}_0\|\mathbf{a}$ field orientation both $\mathbf{d}_{xy}$ and $\mathbf{d}_z$ add, in addition to $\mathbf{d}_2$, to the avoided crossing of one of the triplet components with S_2. The experimental data can be fitted with a single value $d_2=1.8$ cm^{-1} in both field orientations, $\mathbf{B}_0\|\mathbf{a}$ and $\mathbf{B}_0\|\mathbf{c}$. If $\mathbf{d}_{xy}$ and $\mathbf{d}_z$ were comparable in magnitude to $\mathbf{d}_2$, then the extent of avoided crossing would be different in $\mathbf{B}_0\|\mathbf{a}$ and $\mathbf{B}_0\|\mathbf{c}$ field orientations.

Our conclusion is that the dominant DM interactions are $d_1=0.7$ cm^{-1} and $d_2=1.8$ cm^{-1}. In the magnetization plateau state the lattice parameters of $SrCu_2(BO_3)_2$ may change due to spin-phonon coupling.[22] Our calculation of energy levels

did not account for static lattice distortions and therefore we cannot make any conclusions about $\mathbf{d}_{xy}$ and $\mathbf{d}_z$ and the strength of $\mathbf{d}_1$ and $\mathbf{d}_2$ in high magnetic fields.

The intensity of the FIR singlet-triplet transitions depends on the strength of the dynamic DM and on the frequency and the oscillator strength of the phonon. Since the particular phonons involved in the dynamic DM effect in $SrCu_2(BO_3)_2$ are not known we can give only the relative strength of dynamic DM interactions. The *a*- and *c*-polarized singlet-triplet transitions have similar oscillator strengths. These are 2.0 cm^{-2} ($\mathbf{E}_1\|\mathbf{a}$) and 1.7 cm^{-2} ($\mathbf{E}_1\|\mathbf{c}$) if we compare the two lower spectra in Fig. 2 which have been measured on the same sample by changing the direction of the light polarization. The ratio of the dynamic DM interactions for the two mechanisms is $d_{3a}/d_{3c}=\sqrt{2\times 2.0/1.7}=1.5$ if we assume that *a*- and *c*-axis phonons have equal frequencies and oscillator strengths. The factor 2 accounts for the *a*-axis phonon creating a dynamic DM only on the dimer with its axis perpendicular to $\mathbf{E}_1$.

D. Staggered *g*-tensor

The importance of the staggered *g*-tensor in $SrCu_2(BO_3)_2$ was pointed out by Miyahara *et al.*[30] The staggered *g*-tensor exists in $SrCu_2(BO_3)_2$ because of the buckling of Cu-O-B planes below 395 K. It mixes singlet and triplet states similar to the static DM interaction $\mathbf{d}_2$. The strength of the staggered *g*-tensor interaction can be estimated and we show that its effect on the energy of the spin levels is small compared with the effect of $\mathbf{d}_2$. The Zeeman term H_{Zs} couples singlet and triplet states on a single dimer and is proportional to $g_s\mu_B B_0$, where $g_s=(g_{\bar{x}}-g_{\bar{z}})\sin\phi\cos\phi$ (Ref. 30). The angle $\phi\approx 6°$ is the buckling angle of the Cu-O-B plane.[20] The components $g_{\bar{x}}$ and $g_{\bar{z}}$ of the Cu ion *g*-tensor are not known but we take $g_{\bar{x}}\approx g_a=1.998$ and $g_{\bar{z}}\approx g_c=2.219$ (Table I) and get $g_s=0.023$. The staggered term H_{Zs} increases linearly with magnetic field. The largest field where the anticrossing between T_0 and S_2 takes place is 5 T. In this field the magnitude of the staggered *g*-tensor term in the Hamiltonian is 0.05 cm^{-1}, which is much smaller than the static intradimer DM term $d_2=1.8$ cm^{-1}. We conclude that the dominant coupling between the singlet and the triplet is due to the static DM interaction $\mathbf{d}_2$.

E. States of bound triplets

Several states besides the one-triplet excitation are infrared-active (Table I). We showed that the two dimer model explains well the energies of the one-triplet states and transitions to them. In the two dimer model with $j_1=24$ cm^{-1} and $2j_2=9.8$ cm^{-1} we get several two triplet states: a singlet, a triplet, and a quintet of two bound triplets at 28.4, 38.2, and 57.8 cm^{-1}, respectively.

$SrCu_2(BO_3)_2$ has two low energy singlet states S_1 and S_2 which both anticross with triplet state levels (Figs. 4 and 5). In the two dimer model only one singlet of bound triplets is possible and the anticrossing occurs only with $T_{0p}(\pm)$ states. In the experiment an anticrossing is observed between S_2 and $T_{0p}(+)$, Fig. 5(a). The observed anticrossing between S_1 and $T_{0m}(-)$ cannot be explained by the two dimer model. In Sec. II C we show that other DM interactions besides $\mathbf{d}_2$ are weak or absent in $SrCu_2(BO_3)_2$ in the studied $\mathbf{B}_0$ range, although they may have proper symmetry to couple S_1 and $T_{0m}(-)$.

The energy of the 38.2 cm^{-1} triplet in the two dimer model is in the range where triplets are present in $SrCu_2(BO_3)_2$. There is a triplet at 37.5 cm^{-1} labeled as T_1 (Table I). FIR transitions to this state are active in $\mathbf{E}_1\|a$ polarization, Fig. 2. In $\mathbf{E}_1\|c$ the transitions are weaker (Table I). The $T_1(0)$ level is FIR active when $\mathbf{B}_0\|c$ and $T_1(\pm)$ are active when $\mathbf{B}_0\perp c$. All this, polarization and magnetic field dependence, is consistent with the dynamic DM mechanism of the FIR absorption where the dynamic DM is along the *c* axis. The *a*-axis phonon creates a dynamic DM in the direction parallel to the *c* axis. The intradimer dynamic DM interaction d_{3a} does not give any transitions to bound states of triplets. We considered a possibility that the *a*-axis phonon modulates the static interdimer $\mathbf{d}_1$. We found that the pattern of dynamic interdimer DM vectors with the same symmetry as $\mathbf{d}_1$ [Fig. 1(b)] gives selection rules that apply to the 37.5 cm^{-1} T_1 triplet. Transitions to other states are forbidden in the first order of this dynamic DM interaction. The lattice deformation that creates such a pattern of dynamic DM vectors is of A_1 symmetry and is not an optical phonon; in the A_1 symmetry mode Cu atoms on j_1 bond move along the bond in antiphase. We conclude that the two dimer model is not sufficient to account for transitions to states of bound triplets, except to S_2.

Quintet states were observed by high field ESR.[14] Their extrapolated zero field energies are in the range 46–58 cm^{-1}. There are two $\mathbf{E}_1\|\mathbf{a}$ singlet excitations at 52.3 and 53.5 cm^{-1} in this range (Table I). The quintet ($S=2$) has a $m_S=0$ spin level which has the same magnetic field dependence of energy as the $S=0$ state. However, the observed singlets at 52.3 and 53.5 cm^{-1} are not the $m_S=0$ components of the quintet. If in one $\mathbf{B}_0$ field orientation the $m_S=0$ level is infrared-active then in the 90° rotated field orientation other levels, $m_S=\pm 1$ or $m_S=\pm 2$, become active. We studied all possible $\mathbf{B}_0$, $\mathbf{E}_1$ orientations relative to crystal axes and did not find the splitting of the 52.3 and 53.5 cm^{-1} excitations in the magnetic field although they are one to two orders of magnitude more intensive than other magnetic excitations in FIR spectra.

We assigned the *a*-axis polarized ($\mathbf{E}_1\|\mathbf{a}$) 43.0, 52.3, and 53.5 cm^{-1} singlet excitations to magnetic excitations because of the magnetic field and temperature dependence of their energy and intensity.[16] Whether they could be phonons activated by magnetic interactions needs a further study.

III. CONCLUSIONS

In $SrCu_2(BO_3)_2$ the ground state is not exactly a product of singlets on dimers as in the Shastry-Sutherland model, because the intradimer Dzyaloshinskii-Moriya interaction $\mathbf{d}_2$ mixes the ground singlet state with the triplet. From the observed anticrossing between $T_{0p}(+)$ and S_2 we get $d_2=1.8$ cm^{-1}. This is comparable to the interdimer DM, $d_1=0.7$ cm^{-1}, which determines the triplet state energy level zero field splitting. Both $\mathbf{d}_1$ and $\mathbf{d}_2$ determine the magnetic

field dependence of the absorption line intensities.

Although magnetic dipole singlet-triplet transitions are allowed by $\mathbf{d}_2$, the experimentally observed polarization and magnetic field dependencies of absorption line intensities are not described by this interaction. Instead, singlet-triplet transitions are allowed by the dynamic DM mechanism where the electric field component of FIR light couples to a nonsymmetric phonon, which creates the DM interaction. There are two dynamic DM mechanisms in $SrCu_2(BO_3)_2$. In one case the FIR light couples to an *a*-axis phonon and in the other case to a *c*-axis phonon. This is consistent with the calculations of Cépas and Ziman[23] who used a two dimer model in the $j_2=0$ limit.

The experiment also yielded information about higher triplet and singlet excitations. Several of these absorption lines are identified as electric dipole transitions. The two dimer cluster is too small to describe these transitions. Also, we had to use renormalized values of j_1 and j_2 to calculate the energy levels because the actual spin excitations are delocalized over a larger cluster. Obviously a bigger cluster is needed for proper calculation of magnetic excitations in $SrCu_2(BO_3)_2$. Nevertheless, the two dimer model gives us a good description of the one-triplet excitation.

ACKNOWLEDGMENTS

We thank G. Blumberg and O. Cépas for fruitful discussions. This work was supported by the Estonian Science Foundation Grant Nos. 4926, 4927, and 5553.

*Electronic address: roomtom@kbfi.ee

[1] H. Kageyama, K. Yoshimura, R. Stern, N. V. Mushnikov, K. Onizuka, M. Kato, K. Kosuge, C. P. Slichter, T. Goto, and Y. Ueda, Phys. Rev. Lett. **82**, 3168 (1999).
[2] K. Kodama, M. Takigawa, M. Horvatić, C. Berthier, H. Kageyama, Y. Ueda, S. Miyahara, F. Becca, and F. Mila, Science **298**, 395 (2002).
[3] H. Kageyama, M. Nishi, N. Aso, K. Onizuka, T. Yosihama, K. Nukui, K. Kodama, K. Kakurai, and Y. Ueda, Phys. Rev. Lett. **84**, 5876 (2000).
[4] B. S. Shastry and B. Sutherland, Physica B & C **108B**, 1069 (1981).
[5] S. Miyahara and K. Ueda, J. Phys.: Condens. Matter **15**, R327 (2003).
[6] C. Knetter, A. Bühler, E. Müller-Hartmann, and G. S. Uhrig, Phys. Rev. Lett. **85**, 3958 (2000).
[7] A. Koga and N. Kawakami, Phys. Rev. Lett. **84**, 4461 (2000).
[8] W. Zheng, J. Oitmaa, and C. J. Hamer, Phys. Rev. B **65**, 014408 (2001).
[9] C. H. Chung, J. B. Marston, and S. Sachdev, Phys. Rev. B **64**, 134407 (2001).
[10] A. Läuchli, S. Wessel, and M. Sigrist, Phys. Rev. B **66**, 014401 (2002).
[11] T. Munehisa and Y. Munehisa, J. Phys. Soc. Jpn. **73**, 340 (2004).
[12] O. Cépas, K. Kakurai, L. P. Regnault, T. Ziman, J. P. Boucher, N. Aso, M. Nishi, H. Kageyama, and Y. Ueda, Phys. Rev. Lett. **87**, 167205 (2001).
[13] H. Nojiri, H. Kageyama, K. Onizuka, Y. Ueda, and M. Motokawa, J. Phys. Soc. Jpn. **68**, 2906 (1999).
[14] H. Nojiri, H. Kageyama, K. Onizuka, Y. Ueda, and M. Motokawa, J. Phys. Soc. Jpn. **72**, 3243 (2003).
[15] P. Lemmens, M. Grove, M. Fischer, G. Güntherodt, V. N. Kotov, H. Kageyama, K. Onizuka, and Y. Ueda, Phys. Rev. Lett. **85**, 2605 (2000).
[16] T. Rõõm, U. Nagel, E. Lippmaa, H. Kageyama, K. Onizuka, and Y. Ueda, Phys. Rev. B **61**, 14342 (2000).
[17] C. Knetter and G. S. Uhrig, Phys. Rev. Lett. **92**, 027204 (2004).
[18] A. Zorko, D. Arčon, H. van Tol, L. C. Brunel, and H. Kageyama, Phys. Rev. B **69**, 174420 (2004).
[19] S. Miyashita and A. Ogasahara, J. Phys. Soc. Jpn. **72**, 2350 (2003).
[20] K. Sparta, G. J. Redhammer, P. Roussel, G. Heger, G. Roth, P. Lemmens, A. Ionescu, M. Grove, G. Güntherodt, F. Hüning *et al.*, Eur. Phys. J. B **19**, 507 (2001).
[21] K.-Y. Choi, Y. G. Pashkevich, K. V. Lamonova, H. Kageyama, Y. Ueda, and P. Lemmens, Phys. Rev. B **68**, 104418 (2003).
[22] B. Wolf, S. Zherlitsyn, S. Schmidt, B. Lüthi, H. Kageyama, and Y. Ueda, Phys. Rev. Lett. **86**, 4847 (2001).
[23] O. Cépas and T. Ziman, Phys. Rev. B **70**, 024404 (2004).
[24] H. Kageyama, K. Onizuka, T. Yamauchi, and Y. Ueda, J. Cryst. Growth **206**, 65 (1999).
[25] T. Rõõm, D. Hüvonen, U. Nagel, Y.-J. Wang, and R. K. Kremer, Phys. Rev. B **69**, 144410 (2004).
[26] Weak 52.3 and 53.5 cm^{-1} lines are present in $\mathbf{E}_1\|\mathbf{c}$ spectra because the crystal was misaligned relative to the light $\mathbf{k}$ vector; that created a small in-plane $\mathbf{E}_1$ component. As estimated from the residual intensity of the 52.3 and 53.5 cm^{-1} lines in $\mathbf{E}_1\|\mathbf{c}$ polarization the $\mathbf{k}$ vector was out of the (*ab*) plane by $12\pm2°$. The same applies to the $\mathbf{B}_0$ field in Faraday configuration, $\mathbf{B}_0\|\mathbf{k}$. Misalignment of $9\pm1°$ is calculated from the splitting of the triplet components, Fig. 6.
[27] L. Shekhtman, O. Entin-Wohlman, and A. Aharony, Phys. Rev. Lett. **69**, 836 (1992).
[28] L. Shekhtman, A. Aharony, and O. Entin-Wohlman, Phys. Rev. B **47**, 174 (1993).
[29] G. Jorge, R. Stern, M. Jaime, N. Harrison, J. Bonca, S. E. Shawish, C. Batista, H. Dabkowska, and B. Gaulin, cond-mat/0309534 (unpublished).
[30] S. Miyahara, F. Mila, K. Kodama, M. Takigawa, M. Horvatic, C. Berthier, H. Kageyama, and Y. Ueda, J. Phys.: Condens. Matter **16**, S911 (2004).

Low-energy excitations and dynamic Dzyaloshinskii-Moriya interaction in α'-NaV_2O_5 studied by far-infrared spectroscopy

T. Rõõm,* D. Hüvonen, and U. Nagel
National Institute of Chemical Physics and Biophysics, Akadeemia tee 23, 12618 Tallinn, Estonia

Y.-J. Wang
National High Magnetic Field Laboratory, Florida State University, 1800 East Paul Dirac Drive, Tallahassee, Florida 32306, USA

R. K. Kremer
Max-Planck-Institut für Festkörperforschung, Heisenbergstraße 1, D-70569 Stuttgart, Germany
(Received 1 December 2003; published 8 April 2004)

We have studied far-infrared transmission spectra of α'-NaV_2O_5 between 3 and 200 cm^{-1} in polarizations of incident light parallel to *a*, *b*, and *c* crystallographic axes in magnetic fields up to 33 T. The temperature dependence of the transmission spectra was studied close to and below the phase-transition temperature $T_c = 34$ K. The triplet origin of an excitation at 65.4 cm^{-1} (8.13 meV) is revealed by splitting in the magnetic field. The *g* factors for the triplet state are $g_a = 1.96 \pm 0.02$, $g_b = 1.975 \pm 0.004$, and $g_c = 1.90 \pm 0.03$. The magnitude of the spin gap at low temperatures is found to be magnetic-field independent at least up to 33 T. All other infrared-active transitions appearing below T_c are ascribed to zone-folded phonons. Two different dynamic Dzyaloshinskii-Moriya (DM) mechanisms have been discovered that contribute to the oscillator strength of the otherwise forbidden singlet to triplet transition. *First*, the strongest singlet to triplet transition is an electric dipole transition where the polarization of the incident light's electric field is parallel to the ladder rungs ($\mathbf{E}_1 \| \mathbf{a}$). This electric dipole active transition is allowed by the dynamic DM interaction created by a high-frequency optical *a*-axis phonon. *Second*, in the incident light polarization perpendicular to the ladder planes ($\mathbf{E}_1 \| \mathbf{c}$) an enhancement of the singlet to triplet transition is observed when the applied magnetic field shifts the singlet to triplet resonance frequency to match the 68 cm^{-1} *c*-axis phonon energy. The origin of the second mechanism is the dynamic DM interaction created by the 68 cm^{-1} *c*-axis optical phonon. The strength of the dynamic DM is calculated for both mechanisms using the presented theory.

DOI: 10.1103/PhysRevB.69.144410 PACS number(s): 75.10.Pq, 78.30.Hv, 71.70.Gm, 76.30.Fc

I. INTRODUCTION

The opening of a spin gap is of fundamental interest in one-dimensional spin one-half systems. In one-dimensional Heisenberg spin chains the coupling between the spins and lattice leads to the spin-Peierls instability; the atomic distances change together with the nearest-neighbor exchange coupling between the spins. As a result the spin gap opens separating the singlet ground state from the excited triplet state. The spin-Peierls instability was discovered in organic compounds and later on in inorganic $CuGeO_3$.[1] Although α'-NaV_2O_5 is another spin one-half quasi-one-dimensional compound where the spin gap opening and the lattice distortion take place simultaneously,[2,3] it is different from canonical spin-Peierls systems. The magnetic-field dependence of the phase-transition temperature[4,5] T_c and the entropy change[6] at T_c are not consistent with the magnetoelastically driven phase transition in α'-NaV_2O_5, where in addition to the displacement of atoms at $T_c = 34$ K a new charge order appears.[7–10] An extra degree of freedom comes from one electron being shared by the V-O-V rung as α'-NaV_2O_5 is a quarter-filled two-leg spin ladder compound. In the low-temperature phase unpaired electrons on V-O-V rungs shift from the middle of the rung to off-center positions and a zigzag pattern of V^{4+} and V^{5+} ions along the ladder legs exists on all ladders.[7,8,11] There are four ladder planes in the unit cell at ambient pressure and under high pressure a series of successive phase transitions to phases with more than four planes in the unit cell are observed.[12]

α'-NaV_2O_5 is not an ideal one-dimensional spin system as revealed by inelastic neutron scattering (INS).[13,14] In addition to the dispersion of magnetic excitations along the ladder direction two dispersion curves with a rather small dispersion of 1.2 meV along the ladder rung direction are observed. One curve is at 8 meV and the other at 10 meV at the center of the Brillouin zone. More exact spin gap value, 8.13 meV (65.5 cm^{-1}), has been determined by the high-field electron-spin resonance.[15,16]

Doubling of the lattice constants along *a* and *b* axes and quadrupling along *c* axis create additional Raman and infrared-active modes at the phase-transition temperature. The question is whether they are all zone-folded lattice modes or some of them are spin excitations. The controversial modes are infrared-active modes polarized along the *c* axis at 68 and 106 cm^{-1} and Raman modes with frequencies nearly matching the frequencies of the two infrared modes. The origin of the 68 and 106 cm^{-1} excitations is of fundamental interest since the 68 cm^{-1} excitation is almost degenerate with the 65.5 cm^{-1} triplet. Spin chain models do not predict a bound singlet excitation being degenerate with the triplet excitation.[17–19]

Electric and magnetic dipole transitions between singlet and triplet states are forbidden in principle. The reason for this is the different parity of the ground singlet state and the excited triplet state. The singlet state is antisymmetric and

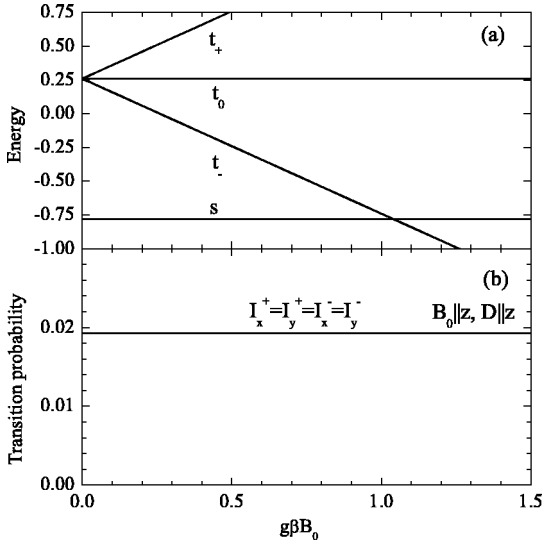

FIG. 1. Two spins coupled by the isotropic exchange coupling, $J=1$, and the DM interaction, $\mathbf{D}\|\mathbf{B}_0$, $D=0.4$. (a) Energy levels; $|t_-\rangle=|T_-\rangle$ and $|t_+\rangle=|T_+\rangle$ are pure triplet states in any field. (b) Nonzero transition probabilities I_i^j from the ground state $|s\rangle$ to the triplet state $|t_j\rangle$ for a given orientation $i=x$ or y of the alternating magnetic field $\mathbf{H}_1$.

the triplet state is symmetric relative to the interchange of two spins. Electric dipole or magnetic dipole operators, responsible for the optical absorption, will not couple these two states. An antisymmetric interaction can mix singlet and triplet states. If such interaction exists the transitions are partially allowed. The strength of the partially allowed optical transition, either magnetic dipole or electric dipole, depends on the orientation of the light polarization and applied magnetic field with respect to the crystal axes. Using infrared spectroscopy it is possible not only to extract a separation of energy levels in a spin system, but also find the origin of the transition, either electric dipole or magnetic dipole, and the orientation of the antisymmetric interaction.

In this paper we study spin gap excitations and phonons in α'-NaV_2O_5 using far-infrared spectroscopy. To explain the experimentally observed singlet to triplet absorption we present a calculation of the dynamic Dzyaloshinskii-Moriya (DM) absorption mechanism by numerical diagonalization of the spin-phonon Hamiltonian. Analytical results in the perturbation theory for the small dynamic DM interaction are given. Also, the theory of the second relevant mechanism, the magnetic dipole active static DM mechanism is presented.

II. STATIC AND DYNAMIC DZYALOSHINSKII-MORIYA INTERACTION

The antisymmetric DM interaction, introduced by Dzyaloshinskii[20] and Moriya,[21] is a combination of superexchange and spin-orbital interactions and is linear in spin-orbital coupling. For a particular spin system the allowed components of the DM interaction are determined by the symmetry of the spin complex.[20,21] Corrections to the energy spectrum due to the DM interaction are usually small because the correction is proportional to D^2/Δ, where D is the magnitude of the DM interaction and Δ is the separation of the singlet and triplet energy levels. In addition to the DM interaction there is a symmetric spin-spin interaction that is quadratic in spin-orbital coupling. Although the symmetric interaction does not couple the singlet and triplet states it affects the splitting of the triplet-state sublevels. It was shown by Shekhtman *et al.*[22,23] for a single-bond superexchange that the triplet state remains degenerate in zero magnetic field if both symmetric and antisymmetric spin-spin interactions are taken into account.

Although the corrections to the energy levels are small, the mixing of the singlet and the triplet state by the antisymmetric interaction could be enough to produce experimentally detectable optical singlet to triplet transitions. The transition probabilities for the magnetic dipole operator in spin chains with DM interactions were calculated by Sakai *et al.*[24] The idea that the electric dipole singlet to triplet transition is partially allowed when an optically active phonon lowers the crystal symmetry and therefore creates a dynamic DM interaction was put forward by Cépas *et al.*[25,26] Below we calculate the energy spectra and transition probabilities using a simple two-spin model. In the case of the static DM mechanism the full spin Hamiltonian with Shekhtman corrections is used. For the dynamic DM interaction we extend the theory of Cépas *et al.* beyond the perturbation theory and solve the Hamiltonian by exact diagonalization.

A. Magnetic dipole transitions and Dzyaloshinskii-Moriya interaction for a spin pair

In this section we calculate the energy spectrum and the magnetic dipole transition probabilities for two isotropically exchange coupled spins ($S=1/2$) in the presence of the antisymmetric DM interaction and the second-order symmetric interaction. We find the eigenvalues and eigenstates of the Hamiltonian $H=H_0+H_{sx}$ and calculate the transition probabilities from the ground state induced by the magnetic dipole operator

$$H_{md}=g\mu_B\mathbf{H}_1\cdot(\mathbf{S}_1+\mathbf{S}_2), \tag{1}$$

where $\mathbf{H}_1$ is the magnetic-field component of the light, g is the electron g factor, and μ_B is the Bohr magneton. The zero-order Hamiltonian is

$$H_0=J\mathbf{S}_1\cdot\mathbf{S}_2+g\mu_B\mathbf{B}_0\cdot(\mathbf{S}_1+\mathbf{S}_2), \tag{2}$$

where J is the isotropic exchange coupling between spins $\mathbf{S}_1$ and $\mathbf{S}_2$, and $\mathbf{B}_0$ is the applied static magnetic field. The first- and second-order corrections are [Eq. (2.19) from Ref. 23]

$$H_{sx}=-\frac{|\mathbf{D}|^2}{4J}\mathbf{S}_1\cdot\mathbf{S}_2+\frac{1}{2J}\mathbf{S}_1\cdot\mathbf{DD}\cdot\mathbf{S}_2+H_{DM}, \tag{3}$$

where $\mathbf{D}$ is the DM vector and we have separated the antisymmetric DM interaction

$$H_{DM}=\mathbf{D}\cdot[\mathbf{S}_1\times\mathbf{S}_2]. \tag{4}$$

We choose singlet and triplet as the basis of eigenstates since they are the eigenstates of H_0. These states are the singlet $|S\rangle=(|+-\rangle-|-+\rangle)/\sqrt{2}$ and the three components of the triplet $|T_-\rangle=|--\rangle$, $|T_0\rangle=(|+-\rangle+|-+\rangle)/\sqrt{2}$, and $|T_+\rangle=|++\rangle$. The spin-quantization axis z is chosen parallel to the applied field $\mathbf{B}_0$ and for a single spin $\langle+|S_z|+\rangle=-\langle-|S_z|-\rangle=1/2$. Let the state vector be $|\Psi\rangle=(T_+,T_0,T_-,S)$. We diagonalize the Hamiltonian $H=H_0+H_{sx}$ for two orientations of applied field, along the DM vector and perpendicular to the DM vector, denoting the eigenstates by (t_+,t_0,t_-,s).

$\boldsymbol{B}_0\|\boldsymbol{D}\|\boldsymbol{z}$. The Hamiltonian in the matrix representation is

$$H=\begin{pmatrix} \frac{1}{4}J+\frac{1}{16}D^2J^{-1}+G_z & 0 & 0 & 0 \\ 0 & \frac{1}{4}J-\frac{3}{16}D^2J^{-1} & 0 & -\frac{1}{2}\imath D \\ 0 & 0 & \frac{1}{4}J+\frac{1}{16}D^2J^{-1}-G_z & 0 \\ 0 & \frac{1}{2}\imath D & 0 & -\frac{3}{4}J+\frac{1}{16}D^2J^{-1} \end{pmatrix}, \tag{5}$$

where $G_z=g\mu_B B_0$ is the Zeeman term. For arbitrarily chosen $J=1$ and $D=0.4$ the energy levels are shown in Fig. 1(a). The symmetric part of H_{sx} adds a correction $D^2/(16J)$ to all energy levels except $|T_0\rangle$ where it is $-3D^2/(16J)$. This correction for $|T_0\rangle$ is partially canceled by H_{DM} that mixes $|S\rangle$ and $|T_0\rangle$. As a result the triplet state sublevels stay degenerate in zero magnetic field as was pointed out in Refs. 22 and 23. The net effect of H_{sx} in zero field is to lower the singlet-state energy by $-3D^2/(16J)$ and to raise the triplet-state energy by $D^2/(16J)$.

The transition probability for the magnetic dipole operator (1) from the ground state is calculated as $I_i^j=|\langle t_j|S_{1i}+S_{2i}|s\rangle|^2$, $i=x,y,z$. The alternating magnetic field $\mathbf{H}_1$ polarized along x or y axis (perpendicular to $\mathbf{B}_0$ and $\mathbf{D}$) gives nonzero intensities as shown in Fig. 1(b). This is because $|s\rangle$ has the triplet component $|T_0\rangle$ mixed in and the transitions from $|T_0\rangle$ to $|T_-\rangle$ and $|T_+\rangle$ are allowed by S_x and S_y operators. The transition probabilities do not depend on the strength of the applied field since the mixing of $|S\rangle$ and $|T_0\rangle$ is independent of $\mathbf{B}_0$.

$\boldsymbol{B}_0\perp\boldsymbol{D}\|\boldsymbol{y}$. The Hamiltonian is

$$H=\begin{pmatrix} \frac{1}{4}J-\frac{1}{16}D^2J^{-1}+G_z & 0 & -\frac{1}{8}D^2J^{-1} & \frac{\sqrt{2}}{4}D \\ 0 & \frac{1}{4}J+\frac{1}{16}D^2J^{-1} & 0 & 0 \\ -\frac{1}{8}D^2J^{-1} & 0 & \frac{1}{4}J-\frac{1}{16}D^2J^{-1}-G_z & \frac{\sqrt{2}}{4}D \\ \frac{\sqrt{2}}{4}D & 0 & \frac{\sqrt{2}}{4}D & -\frac{3}{4}J+\frac{1}{16}D^2J^{-1} \end{pmatrix}. \tag{6}$$

In this field orientation $|T_-\rangle$ and $|T_+\rangle$ are mixed into $|S\rangle$ by H_{DM} and $|t_0\rangle$ remains a pure state, $|t_0\rangle=|T_0\rangle$. Note that there is an avoided crossing at $g\mu_B B_0\approx 1$ between $|s\rangle$ and $|t_-\rangle$ as shown in Fig. 2(a).

The transitions from $|s\rangle$ to $|t_-\rangle$ and $|t_+\rangle$ are observed when $\mathbf{H}_1\|\mathbf{B}_0$, see I_z^- and I_z^+ in Fig. 2(b). In high magnetic field I_z^- prevails over I_z^+ because the mixing of $|T_-\rangle$ into the ground state increases and the mixing of $|T_+\rangle$ decreases. Finite transition probability I_x^0 to the $|t_0\rangle$ is observed in small fields when $\mathbf{H}_1\perp\mathbf{B}_0,\mathbf{D}$ whereas $I_y^0=0$ $(\mathbf{H}_1\|\mathbf{D})$ as B_0 approaches zero. Both transition probabilities are determined by the amount $|T_-\rangle$ and $|T_+\rangle$ are mixed into the ground state since transition operators S_x and S_y couple these two states to the $|t_0\rangle=|T_0\rangle$ state. I_x^0 and I_y^0 gain intensity as the ground state changes into $|T_-\rangle$ with increasing field.

In summary, the following selection rules are observed for

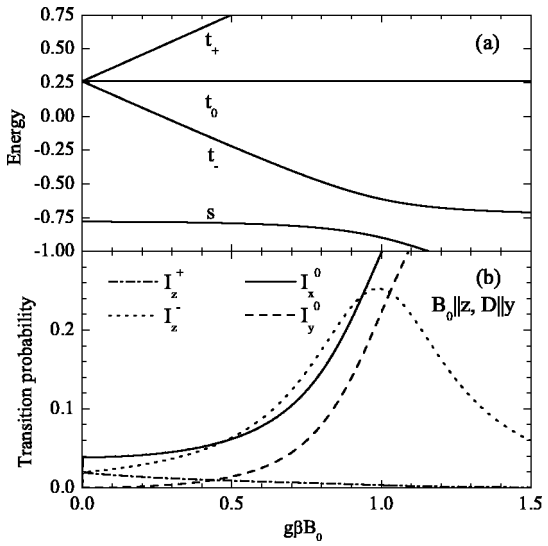

FIG. 2. Two spins coupled by the isotropic exchange coupling, $J=1$, and the DM interaction, $\mathbf{D}\perp\mathbf{B}_0$, $D=0.4$. (a) Energy levels; $|t_0\rangle=|T_0\rangle$ is a pure triplet state in any field. (b) Nonzero transition probabilities I_i^j from the ground state $|s\rangle$ to the triplet state $|t_j\rangle$ for a given orientation $i=x$, y, or z of the alternating magnetic field $\mathbf{H}_1$.

the magnetic dipole transition from the singlet to the triplet state in the presence of DM interaction. *First*, if the magnetic field is parallel to the DM vector $\mathbf{D}\|\mathbf{B}_0$, transitions to the triplet state sublevels $|t_-\rangle$ and $|t_+\rangle$ are observed. These transitions have field-independent intensities and do not depend on polarization in the plane perpendicular to the DM vector, $\mathbf{H}_1\perp\mathbf{D}$. *Second*, if the magnetic field is perpendicular to the DM vector $\mathbf{B}_0\perp\mathbf{D}$, then in small fields ($B_0\ll J/g\mu_B$) the transition to $|t_0\rangle$ has a weak field dependence and is observed in polarization $\mathbf{H}_1\perp\mathbf{B}_0,\mathbf{D}$. The transitions to $|t_-\rangle$ and $|t_+\rangle$ are observed in $\mathbf{H}_1\|\mathbf{B}_0$ polarization. In this polarization in magnetic fields, $g\mu_B B_0\geqslant D$, the transition probability to $|t_-\rangle$ increases and to $|t_+\rangle$ decreases with increasing field. Sakai *et al.*[24] calculated magnetic dipole transition probabilities for interacting spin chains using a 16-spin cluster. In their model the symmetric anisotropic superexchange was not considered. Our single-dimer model leaves the triplet levels degenerate whereas the degeneracy is lifted in their calculation. Whether the degeneracy will be lifted or not when the symmetric anisotropic superexchange in addition to the antisymmetric DM interaction is included in their model needs a separate study.

B. Electric dipole transitions and dynamic Dzyaloshinskii-Moriya interaction for a spin pair

We show that the electric-field component of the far-infrared light $\mathbf{E}_1$ that couples to an optically active phonon can cause transitions between singlet and triplet states if this phonon creates a DM interaction by lattice deformation.

Electric dipole coupling between the phonon and the light in the long-wavelength limit is

$$V=eQE_1, \tag{7}$$

where e is an effective charge associated with a lattice normal coordinate Q. Here we assume that the electric field is polarized parallel to the electric dipole moment of the normal coordinate Q and we have dropped the time dependence of V.

We expand the DM vector $\mathbf{D}$ into a power series of Q,

$$\mathbf{D}(Q)=\mathbf{D}(0)+\left.\frac{\partial\mathbf{D}}{\partial Q}\right|_{Q=0}Q+\cdots. \tag{8}$$

The first term is the static DM vector in the absence of lattice deformation. We already demonstrated in the preceding section that this interaction gives rise to magnetic dipole transitions between singlet and triplet states. Here for simplicity we take $\mathbf{D}(0)=0$. We will ignore terms quadratic in $\mathbf{D}$ in H_{sx} [Eq. (3)] because these symmetric interactions will not give us any transitions between singlet and triplet states. Leaving out higher-order terms of Q we get for the DM interaction (4)

$$H_{DMQ}=Q\mathbf{D}_Q\cdot[\mathbf{S}_1\times\mathbf{S}_2], \tag{9}$$

where $\mathbf{D}_Q\equiv\partial\mathbf{D}/\partial Q|_{Q=0}$. For the phonon system we use the secondary quantization presentation. The lattice normal coordinate Q can be presented in terms of creation and annihilation operators $a^\dagger$ and a, $Q=q(a^\dagger+a)$, where q is the transformation coefficient. Since we left out Q^2 and higher-order terms in Eq. (8), the dynamic DM interaction will couple two phonon states $|n\rangle$ and $|n'\rangle$, where $n'=n\pm1$; n is the occupation number of phonons in mode Q.

The Hamiltonian of the coupled spin-phonon system is

$$H=\hbar\omega_p a^\dagger a+J\mathbf{S}_1\cdot\mathbf{S}_2+g\mu_B\mathbf{B}_0\cdot(\mathbf{S}_1+\mathbf{S}_2)+H_{DMQ}^{(1)}, \tag{10}$$

$$H_{DMQ}^{(1)}=q(a^\dagger+a)\mathbf{D}_Q\cdot[\mathbf{S}_1\times\mathbf{S}_2], \tag{11}$$

$\hbar\omega_p$ is the phonon energy. In the low-temperature limit $k_BT\ll\hbar\omega$ the thermal population of phonon states is low, $\langle n\rangle\approx0$, and we can consider only the phonon states with either 0 or 1 phonon, $|0\rangle$ and $|1\rangle$. After diagonalization of the Hamiltonian (10) we treat V, Eq. (7), as a time-dependent perturbation to calculate the transition probabilities from the ground state. We choose $|S\rangle$ and $|T_i\rangle$ with the quantization axis along the applied field $\mathbf{B}_0$ as the basis for the spin states. Let the state vector be $\Psi=(T_+1,T_+0,T_01,T_00,T_-1,T_-0,S1,S0)$. The Hamiltonian is diagonal in this basis except for the last term, $H_{DMQ}^{(1)}$. The eigenstates are labeled by $|sn\rangle$ and $|t_in\rangle$ where $n=0$ or 1. We solve two separate cases $\mathbf{D}_Q\|\mathbf{B}_0$ and $\mathbf{D}_Q\perp\mathbf{B}_0$.

$\boldsymbol{D}_Q\|\boldsymbol{B}_0\|z$. In this field orientation $\mathbf{D}_Q=(0,0,D_Q)$. The diagonal elements are the same as in Eq. (5) except that $D=0$ and the phonon energy $\hbar\omega_p$ will be added if $n=1$. Beside the diagonal elements the nonzero elements of the Hamiltonian (10) are the ones created by $H_{DMQ}^{(1)}$: $\langle S1\,|\,H_{DMQ}^{(1)}\,|\,T_00\rangle=\langle S0|H_{DMQ}^{(1)}|T_01\rangle=-\langle T_01|H_{DMQ}^{(1)}|S0\rangle=-\langle T_00|H_{DMQ}^{(1)}|S1\rangle=\imath qD_Q/2$. The energy levels, calculated for $J=1$, $\hbar\omega_p=1.2$, and $qD_Q=0.4$, are shown in Fig. 3(a). The largest repulsion is between $|s1\rangle$ and $|t_00\rangle$, which are the linear combinations of $|S1\rangle$ and $|T_00\rangle$. The other two

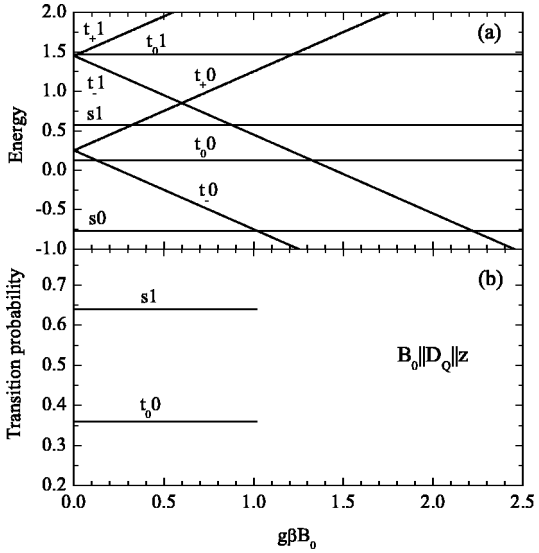

FIG. 3. Two spins coupled by the isotropic exchange coupling, $J=1$, and the dynamic DM interaction, $qD_Q=0.4$, created by the phonon with a frequency $\hbar\omega_p=1.2$; $\mathbf{D}_Q \| \mathbf{B}_0$. (a) Energy levels; $|t_\pm 0\rangle$ and $|t_\pm 1\rangle$ are pure states $|T_\pm 0\rangle$ and $|T_\pm 1\rangle$ in any field. (b) Nonzero electric dipole transition probabilities from the ground state to the coupled spin-phonon state $|t_0 0\rangle$ and $|s1\rangle$. The graph is not extended above the field where the ground state changes from the singlet $|s0\rangle$ to the triplet $|t_- 0\rangle$.

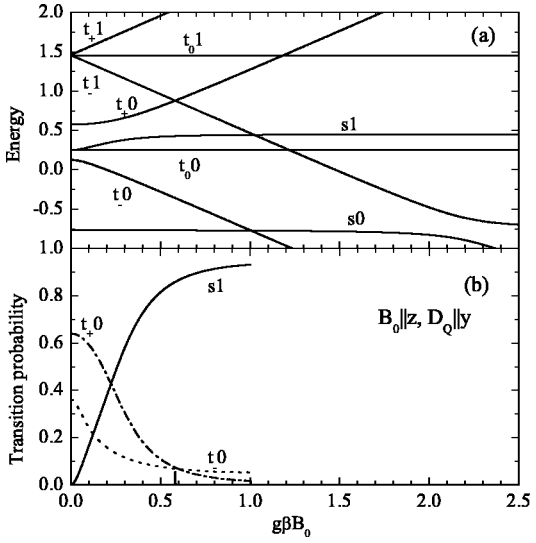

FIG. 4. Two spins coupled by the isotropic exchange coupling, $J=1$, and the dynamic DM interaction, $qD_Q=0.4$, created by the phonon with a frequency $\hbar\omega_p=1.2$; $\mathbf{D}_Q \perp \mathbf{B}_0$. (a) Energy levels; $|t_0 0\rangle$ and $|t_0 1\rangle$ are pure states $|T_0 0\rangle$ and $|T_0 1\rangle$ in any field. (b) Nonzero electric dipole transition probabilities from the ground state to the coupled spin-phonon state $|t_- 0\rangle$ (dotted), $|t_+ 0\rangle$ (dash-dotted), and $|s1\rangle$ (solid). The graph is not extended above the field where the ground state changes from the singlet $|s0\rangle$ to the triplet $|t_- 0\rangle$.

mixed together states are $|S0\rangle$ and $|T_0 1\rangle$ giving us the states $|s0\rangle$ and $|t_0 1\rangle$. One has to keep in mind that not only the spin states are mixed, but also the phonon states $|0\rangle$ and $|1\rangle$ are mixed. All other four states that involve triplet states $|T_\pm\rangle$ are pure states.

The splitting of energy levels has to be taken with some precaution. The splitting due to the dynamic DM is observed when there is one phonon excited, $n=1$. This is not the case at thermal equilibrium at low T when $\langle n\rangle=0$ (the possible role of zero-point vibrations is ignored in our approach). If the phonon is brought to the state $n=1$ by the light-phonon interaction (7) the effect of one phonon on the shift of energy levels should be observed in the experiment, unless it is much smaller than the lifetime or inhomogeneous broadening of energy levels. The magnitude of the shift and whether it could be observed in the experiment or not will not affect conclusions about the transition probabilities.

Calculation of the transition probability $|\langle t_j n'|V|s0\rangle|^2$ is straightforward since V couples states that are diagonal in the basis of pure spin states and nondiagonal in the basis of phonon states $|0\rangle$ and $|1\rangle$. Two transitions from the ground state $|s0\rangle$ are observed, to $|s1\rangle$ and $|t_0 0\rangle$, shown in Fig. 3(b). If the dynamic DM is zero, then $|s0\rangle=|S0\rangle$, $|s1\rangle=|S1\rangle$, and $|t_0 0\rangle=|T_0 0\rangle$. The transition from $|s0\rangle$ to $|s1\rangle$ is an ordinary absorption of an infrared photon $\hbar\omega_p=E_{s1}-E_{s0}$ with probability 1, and the transition to $|t_0 0\rangle$ has zero probability. When the dynamic DM interaction is turned on, additional absorption sets in and a photon of energy $E_{t_0 0}-E_{s0}$ is absorbed. This can be viewed as a virtual excitation of a phonon by the light to the state $|1\rangle$ while the spin state remains singlet, and then the dynamic DM interaction (9) brings the (virtual) phonon back to $|0\rangle$ while changing the spin state to $|T_0\rangle$. The polarization of the absorbed photon with respect to the crystal axes is determined by the phonon states involved.

$\boldsymbol{D}_Q \perp \boldsymbol{B}_0 \| z$. We take $\mathbf{D}_Q=(0,D_Q,0)$. Beside diagonal elements there are eight nonzero elements $\langle T_+1|H^{(1)}_{DMQ}|S0\rangle$, $\langle T_+0|H^{(1)}_{DMQ}|S1\rangle$, $\langle T_-1|H^{(1)}_{DMQ}|S0\rangle$, $\langle T_-0|H^{(1)}_{DMQ}|S1\rangle$, $\langle S1|H^{(1)}_{DMQ}|T_+0\rangle$, $\langle S1|H^{(1)}_{DMQ}|T_-0\rangle$, $\langle S0|H^{(1)}_{DMQ}|T_+1\rangle$, $\langle S0|H^{(1)}_{DMQ}|T_-1\rangle$, all equal to $\sqrt{2}qD_Q/4$. The energy levels, calculated for $J=1$, $\hbar\omega_p=1.2$, and $qD_Q=0.4$, are plotted in Fig. 4(a).

The strongest mixing occurs between $|S1\rangle$ and $|T_\pm 0\rangle$ giving the eigenstates $|s1\rangle$ and $|t_\pm 0\rangle$. Also, there is an additional mixing between $|T_- 0\rangle$ and $|T_+ 0\rangle$ levels in small fields.

In small fields, $g\mu_B B_0 < J$, the mixing of $|S0\rangle$ and $|T_\pm 1\rangle$ is less pronounced since their separation is larger than the separation of $|S1\rangle$ and $|T_\pm 0\rangle$. Therefore, for the analysis of the transition probabilities the ground state can be taken as pure $|S0\rangle$ and the transition probabilities are mainly determined by the mixing between $|S1\rangle$ and $|T_\pm 0\rangle$. The effect of mixing of $|T_\pm 1\rangle$ into the ground state has a secondary effect on the transition probabilities. Transitions from the ground state to three excited states $|t_+ 0\rangle$, $|t_- 0\rangle$, and $|s1\rangle$ have nonzero probabilities [see Fig. 4(b)]. The transition probability to the $|s1\rangle$ state increases with field because $|s1\rangle$ changes gradually from the mixed state into $|S1\rangle$. The transition probabilities to $|t_+ 0\rangle$ and $|t_- 0\rangle$ state decrease as the field increases because the amount of $|S1\rangle$ mixed into them decreases. Again, the polarization of the absorbed photon with respect to the crystal axes is determined by the phonon states involved.

Perturbation theory. Analytical results can be obtained in the limit $|E_{S1}-E_{T_i0}| \gg qD_Q$, $i=-,0,+$. This case holds when $|\hbar\omega_p-(J\pm g\mu_B B_0)| \gg qD_Q$. We find the first-order perturbation corrections to the states $|Sn\rangle$ and $|T_i n\rangle$, where $n=0,1$, using $H^{(1)}_{DMQ}$, Eq. (11), as perturbation. Then the transition probabilities are calculated between the new states $|s0\rangle$ and $|t_i 0\rangle$ as was done in the exact treatment.

For $\mathbf{D}_Q \| \mathbf{B}_0 \| \mathbf{z}$ we get

$$|\langle t_0 0|V|s0\rangle|^2 = I_p \frac{(qD_Q)^2(\hbar\omega_p)^2}{[(\hbar\omega_p)^2-J^2]^2}, \tag{12}$$

where $I_p=(eqE_1)^2$ is the light absorption intensity by the infrared-active phonon. The transition probability from $|s_0\rangle$ to the triplet level $|t_0\rangle$ is independent of the magnetic field.

For the perpendicular case, $\mathbf{D}_Q \perp \mathbf{B}_0 \| \mathbf{z}$,

$$|\langle t_- 0|V|s0\rangle|^2 = I_p \frac{(qD_Q)^2(\hbar\omega_p)^2}{2[(\hbar\omega_p)^2-(J-g\mu_B B_0)^2]^2}, \tag{13}$$

$$|\langle t_+ 0|V|s0\rangle|^2 = I_p \frac{(qD_Q)^2(\hbar\omega_p)^2}{2[(\hbar\omega_p)^2-(J+g\mu_B B_0)^2]^2}. \tag{14}$$

If $\hbar\omega_p \ll J$ then the intensity of the transition from $|s0\rangle$ to $|t_- 0\rangle$ increases with the magnetic field and decreases for the transition to $|t_+ 0\rangle$. If $\hbar\omega_p \gg J$ then the intensity of the $|s0\rangle$ to $|t_+ 0\rangle$ transition increases and of $|s0\rangle$ to $|t_- 0\rangle$ decreases. In the perturbation limit the zero-field intensities of the transitions from $|s0\rangle$ to $|t_- 0\rangle$ and $|t_+ 0\rangle$ are equal.

In summary, the following selection rules are obtained for the electric dipole transition from the singlet to the triplet state in the presence of the dynamic DM interaction: (1) The polarization of the transition: $\mathbf{E}_1$ is parallel to the dipole moment of the optically active phonon that creates the dynamic DM interaction; (2) the orientation of the dynamic DM vector $\mathbf{D}_Q$ is determined by the symmetry of the lattice distortion created by the optically active phonon; (3) if $\mathbf{B}_0 \| \mathbf{D}_Q$ a magnetic-field-independent transition probability to the triplet-state sublevel $|t_0 0\rangle$ is observed; (4) if $\mathbf{B}_0 \perp \mathbf{D}_Q$ magnetic-field-dependent transition probabilities to the triplet-state sublevels $|t_+ 0\rangle$ and $|t_- 0\rangle$ are observed.

III. EXPERIMENT

We studied several single crystals of α'-$Na_xV_2O_y$ from the batch E106.[27] According to the heat-capacity measurements these crystals have $T_c=33.9$ K, and the chemical composition $x=1.02$ and $y=5.06$. The (ab)-plane properties, $\mathbf{E}_1 \perp \mathbf{c}$, $\mathbf{k} \| \mathbf{c}$, were studied on three single crystals, 600 μm [area in the (ab) plane 21 mm^2], 120 μm (20 mm^2), and 40 μm (3.5 mm^2) thick in $\mathbf{c}$ direction. The (bc)-plane properties, $\mathbf{E}_1 \perp \mathbf{a}$, $\mathbf{k} \| \mathbf{a}$, were measured on a mosaic of three crystals, each $\approx$650 μm thick, with a total area of 19 mm^2 in the (bc) plane. The (ac)-plane properties, $\mathbf{E}_1 \perp \mathbf{b}$, $\mathbf{k} \| \mathbf{b}$, were measured on a mosaic of seven crystals, each $\approx$800 μm thick, with a total area of 8.5 mm^2 in the (ac) plane.

The far-infrared measurements were done with a polarizing Martin-Puplett Fourier-transform spectrometer.[28] Light pipes were used to guide the far-infrared light into the sample cryostat equipped with a 12 T Oxford Instruments magnet and two silicon bolometers from Infrared Laboratories operated at 0.3 K. A rotatable polarizer was mounted at the end of the light pipe in front of the sample to control the polarization of light. Spectra were recorded at 0.2 to 0.3 cm^{-1} resolution. The magnetic field was applied parallel to the direction of light propagation (Faraday configuration, $\mathbf{k} \| \mathbf{B}_0$) or perpendicular to the light propagation (Voigt configuration, $\mathbf{k} \perp \mathbf{B}_0$). Measurements above 12 T were performed at the National High Magnetic Field Laboratory on a 33 T Bitter magnet in the Faraday configuration using a Bruker IFS 113v infrared spectrometer and a 4 K silicon bolometer from Infrared Laboratories.

The anisotropic power absorption coefficient $\alpha_i(\omega)$ $(i=a,b,c)$ was calculated from the measured transmission $T_i(\omega)$ assuming one back reflection from the crystal front face and one from the back face, $T_i(\omega)=(1-R_i)^2\exp[-\alpha_i(\omega)d]$, where d is the thickness of the crystal. We used a frequency-independent value for the reflectance coefficient $R_i=[(n_i-1)/(n_i+1)]^2$. Indices of refraction, n_i, at 4 K and terahertz frequencies are $n_a=3.64$, $n_b=3.16$, and $n_c=2.70$ (Ref. 29). According to another paper[30] indices of refraction at 4 K and 0.55 cm^{-1} are $n_a=3.07$, $n_b=3.19$, and $n_c=2.03$. We calculated $n_a/n_b=1.16$ from the fringe pattern in the 10 to 50 cm^{-1} range using our transmission data. This ratio is more similar to the ratio $n_a/n_b=1.15$ from Ref. 29 and therefore we used their values for refraction indices. The real part of the conductivity in units of Ω^{-1} cm^{-1} is

$$\sigma_1^i(\omega)=n_i(\omega)\alpha_i(\omega)/(120\pi), \tag{15}$$

where in the limit of weak absorption we take n_i to be independent of frequency.

IV. RESULTS

A. Absorption spectra and their temperature dependence

The absorption spectra at temperatures above and below the phase-transition temperature T_c for incident light polarizations $\mathbf{E}_1 \| \mathbf{a}$ and $\mathbf{E}_1 \| \mathbf{b}$ are shown in Fig. 5 and for $\mathbf{E}_1 \| \mathbf{c}$ in Fig. 6. Below T_c several new lines appear. The line parameters are listed in Table I. The full width at half maximum (FWHM) of the narrowest lines is determined by the used instrument resolution, 0.2 cm^{-1}. The best fit for the resolution limited narrow lines was obtained using Gaussian line shapes, otherwise a Lorentzian line shape was used.

The $\mathbf{E}_1 \| \mathbf{a}$ absorption at 40 K is dominated by a continuous absorption steadily increasing towards high frequencies. Above 180 cm^{-1} the absorption is too strong and our data are not reliable above this frequency. There are two derivativelike absorption lines, one at 91.2 cm^{-1} and the other at 140 cm^{-1}, the latter being relatively broad and has its phase opposite to the 91.2 cm^{-1} line phase. There is a narrow line at 137.6 cm^{-1} on top of the 140 cm^{-1} line. When T is lowered, the absorption continuum is diminished over the entire frequency range. Still, substantial absorption continuum remains above 130 cm^{-1}. At $T=4$ K the 91.2 and 140 cm^{-1} lines have a normal absorptionlike line shape. New lines ap-

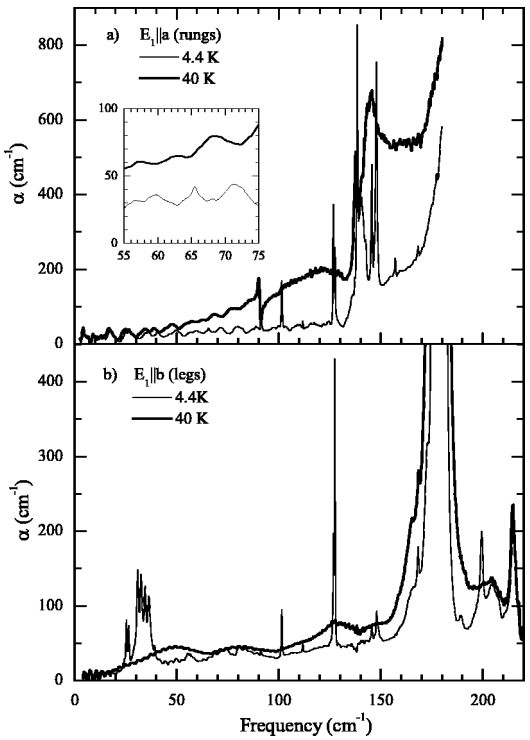

FIG. 5. Absorption spectra of α'-NaV_2O_5 below, $T=4.4$ K, and above, $T=40$ K, the phase-transition temperature. (a) $\mathbf{E}_1\|\mathbf{a}$, (b) $\mathbf{E}_1\|\mathbf{b}$. The inset shows the singlet to triplet excitation at 65 cm^{-1}.

pear as well: doublets at 102, 127, 147 cm^{-1} and single lines at 112, 157, 168 cm^{-1}. The inset in Fig. 5(a) shows a weak line at 65.4 cm^{-1}, the singlet to triplet excitation. The magnetic properties of this transition are described in more detail in Sec. IV B. The *T*-dependent spectra of the singlet to triplet transition are plotted in Fig. 7. To better extract this relatively weak line the difference of two spectra at fixed *T*, one measured in 0 T field and the other measured in 5 or 10 T field, was calculated. One can see that the negative line, representing the zero-field spectrum, together with the positive features (the lines in 5 or 10 T spectra) shift to lower frequencies as the temperature increases and at the same time the lines lose intensity and broaden. The temperature dependence of line parameters is plotted in Fig. 8.

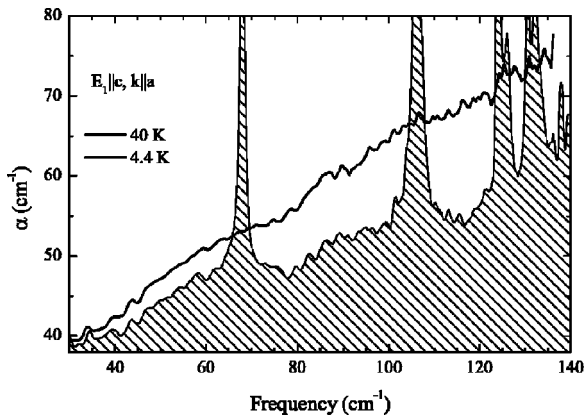

FIG. 6. Absorption spectra at 4.4 K and 40 K in $\mathbf{E}_1\|\mathbf{c}$ polarization.

TABLE I. Absorption line positions ω_0 (cm^{-1}), full widths at half maximum γ(cm^{-1}), and areas (cm^{-2}) in 4.4 K and 40 K spectra of α'-NaV_2O_5 in zero magnetic field. Index *T* refers to the singlet to triplet excitation and *F* to the Fano line shape.

	4.4 K			40 K		
	ω_0	γ	Area	ω_0	γ	Area
$\mathbf{E}_1\|\mathbf{a}$	65.4^T	0.6	6			
	91.2	0.2	50	90.7^F	0.8	120
	101.4	0.26	110			
	101.7	0.19	47			
	111.7	0.18	8			
	126.7	0.17	240			
	127.5	0.22	140			
	138.5	0.4	450	137.7	2.2	1000
	140	4.4	2000	141.0^F	8	5300
	145.6	0.5	230			
	147.8	0.8	650			
	157.1	0.29	25			
	168.2	0.35	16			
$\mathbf{E}_1\|\mathbf{b}$	25.3	0.55	54			
	26.4	0.47	37			
	30.8	0.84	130			
	32.5	1.05	145			
	34.5	0.95	109			
	36.4	1.51	181			
	65.4^T	0.2	0.3			
	39.1	0.43	9			
	91.3	0.3	5			
	101.4	0.24	70			
	111.7	0.2	24			
	126.7	0.26	100			
	127.5	0.2	320			
	145.7	0.58	11			
	148.0	0.65	25			
	168.3	0.42	27	168.6	0.6	20
	180			180		
	199.4	1.4	157			
	215.1	2.2	420	214.9	2.5	450
$\mathbf{E}_1\|\mathbf{c}$	65.4^T	0.2	0.5			
	68	<1	>100			
	106	<2.5	>110			
	124	<1	>50			
	126	<1.5	>30			
	130	<1	>20			
	132	<2	>50			

The $\mathbf{E}_1\|\mathbf{b}$ absorption at 40 K is dominated by a strong phonon line at 180 cm^{-1} and a weaker line at 215 cm^{-1}, Fig. 5(b). The temperature-dependent absorption continuum, as was observed in $\mathbf{E}_1\|\mathbf{a}$ polarization, is absent in $\mathbf{E}_1\|\mathbf{b}$ [note the different vertical scales in Figs. 5(a) and 5(b)]. Several lines, at 101.4, 111.7, 126.7, and 127.5 cm^{-1}, have the same frequency as in the *a*-axis spectrum, although different

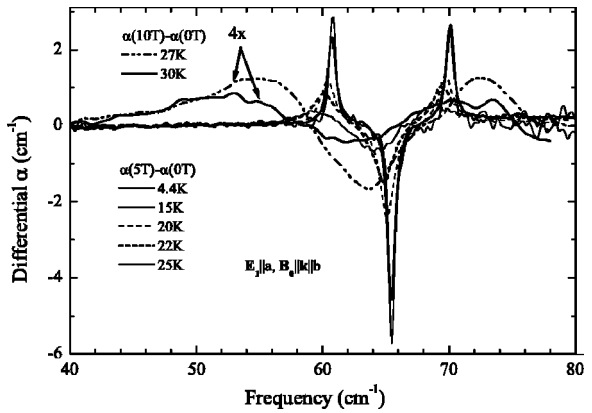

FIG. 7. Temperature dependence of the singlet to triplet absorption spectrum in $\mathbf{E}_1\|\mathbf{a}$ polarization.

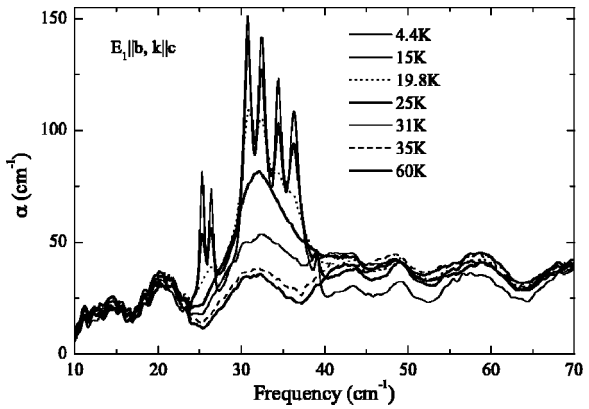

FIG. 9. Temperature dependence of seven low-frequency *b*-axis phonons.

strength. The line parameters are listed in Table I. The temperature evolution of the multiplet of seven lines in the $\mathbf{E}_1\|\mathbf{b}$ spectrum below 40 cm^{-1} is shown in more detail in Fig. 9. Below $T_c = 34$ K a broad line appears at 32 cm^{-1}. Another line appears at 26 cm^{-1} as T is lowered. At low T those two features split into a doublet and a quintet. The line at the highest frequency, 39 cm^{-1}, is relatively weak compared to other six lines. The spectra shown in Fig. 9 have not been corrected for light interference fringes in the sample. The 60 K spectrum could be used as a background, but with some precaution as some intensity is lost between 40 and 70 cm^{-1} when T is lowered.

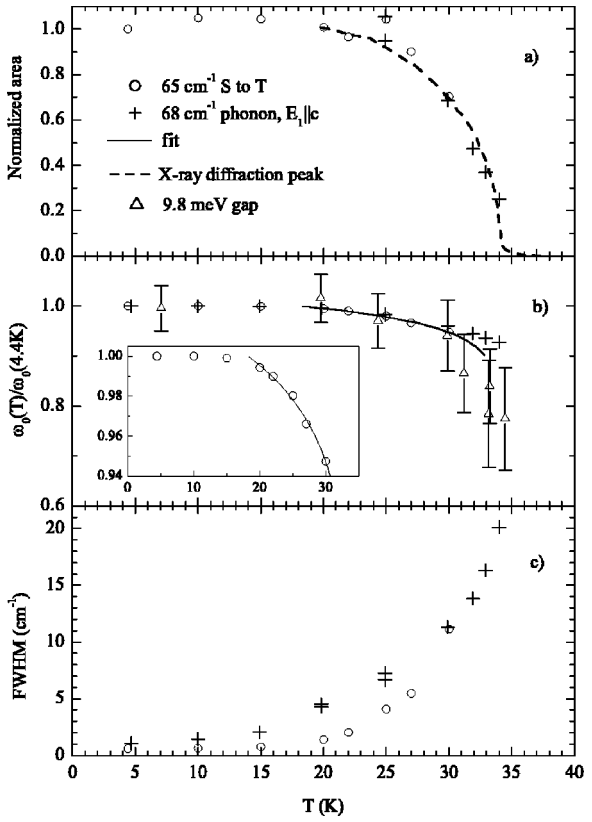

FIG. 8. Zero magnetic-field temperature dependence of the normalized absorption line area [panel (a)], normalized resonance frequency (b), and FWHM (c) for the singlet to triplet transition at 65.4 cm^{-1} $\mathbf{E}_1\|\mathbf{a}$ (circles), and for the 68 cm^{-1} *c*-axis phonon (crosses). Inset to (b): the solid line is a fit of the S to T transition energy $\Delta(T)/\Delta(4.7\ \mathrm{K}) = (1 - T/T_c)^{\beta}$ above 20 K; $T_c = 33.9$ K, $\beta = 0.039 \pm 0.002$. Additionally the x-ray-diffraction peak intensity from Ref. 38 is plotted with a dashed line in panel (a) and the normalized gap at 9.8 meV measured by INS (Ref. 3) is shown with triangles in (b).

The $\mathbf{E}_1\|\mathbf{c}$ absorption spectrum has no sharp features below 140 cm^{-1} in the high-temperature phase at $T = 40$ K (Fig. 6). When T is lowered below 34 K new lines evolve at 68, 106 cm^{-1}, and two doublets around 124 and 132 cm^{-1}. Since the low-T transmission was too small at the transmission minimums and the absorption coefficient cannot be determined accurately, only the upper limits for the linewidths and the lower limits for the line areas are given in Table I. The temperature dependence of the 68 cm^{-1} line is shown in Fig. 10. The line shifts to lower frequency and broadens as T is raised from 4.5 K. Some intensity change is still observed above T_c between 34 and 35 K, but there are no visible differences between the 35 K and 37 K spectra. The temperature dependence of line parameters is plotted in Fig. 8 together with the singlet to triplet resonance data. Since the largest experimentally detectable absorption was limited by the thickness of available crystals the line area has been re-

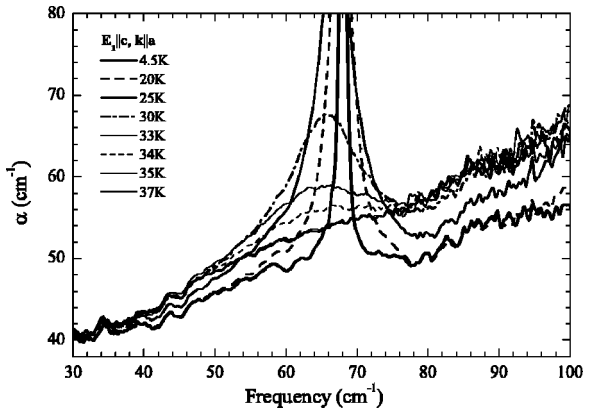

FIG. 10. The temperature dependence of the 68 cm^{-1} *c*-axis phonon absorption spectrum.

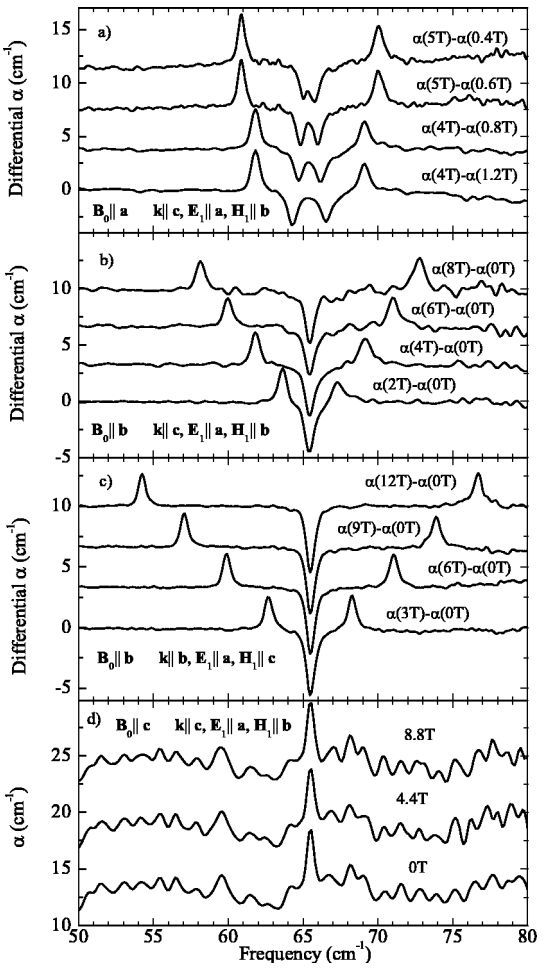

FIG. 11. Magnetic-field dependence of the singlet to triplet transition spectra in $\mathbf{E}_1\|\mathbf{a}$ polarization. Spectra have been shifted in vertical direction. Measurements were done in Voigt (a),(b) and in Faraday configuration (c),(d).

liably determined only above 25 K. Below 25 K the plotted FWHM is the upper limit for the linewidth.

B. Singlet to triplet absorption in magnetic field

We studied the magnetic-field effect on the absorption spectra below 130 cm^{-1} at 4.4 K in magnetic fields up to 12 T in all three polarizations, $\mathbf{E}_1\|\mathbf{a}$, $\mathbf{E}_1\|\mathbf{b}$, and $\mathbf{E}_1\|\mathbf{c}$. We did not see any line shifts nor intensity changes except for the 65.4 cm^{-1} absorption line.

For $\mathbf{E}_1\|\mathbf{a}$ polarization the magnetic-field effect on the 65.4 cm^{-1} line is demonstrated in Fig. 11. When the field $\mathbf{B}_0$ is parallel to the *a* or *b* axis, the line splits [panels (a)–(c)]. In $\mathbf{B}_0\|\mathbf{c}$ configuration the line does not split or change its intensity [panel (d)]. From the field dependence of the resonance frequency the 65.4 cm^{-1} absorption line can be identified as a transition from a singlet ground state $S=0$ to a triplet excited state $S=1$. Light is absorbed, depending on its polarization, either by transitions to $m_S=1$ and $m_S=-1$ triplet levels when $\mathbf{B}_0\perp\mathbf{c}$ or to the magnetic-field-independent $m_S=0$ level when $\mathbf{B}_0\|\mathbf{c}$. The measurements were extended to 33 T in one polarization and field orientation, $\mathbf{E}_1\|\mathbf{a}$, $\mathbf{B}_0\|\mathbf{b}$.

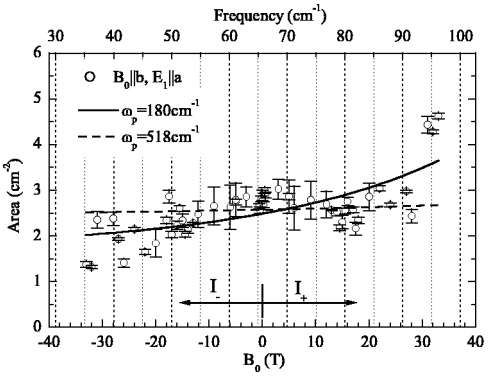

FIG. 12. The magnetic-field, $\mathbf{B}_0\|\mathbf{b}$, dependence of the singlet to triplet resonance line area at 4.4 K in $\mathbf{E}_1\|\mathbf{a}$ polarization. The values for the transition to $m_S=-1$ are plotted in the negative field direction and for the transition to $m_S=1$ in the positive field direction; $g_a\mu_B=0.922$ $\mathrm{cm}^{-1}/\mathrm{T}$. The lines show the theoretical transition probability for the electric dipole transition for a set of parameters where ω_p is the resonance frequency of an optical phonon coupled to the spin system by the dynamic DM interaction: solid line, $\omega_p=180$ cm^{-1}; dashed line, $\omega_p=518$ cm^{-1}.

The field dependence of the singlet to triplet transition line areas is shown in Fig. 12. The lines were fitted with a Lorentzian function, FWHM being between 0.5 and 0.6 cm^{-1}. The line areas of the transitions to the $m_S=-1$ and $m_S=1$ levels depend weakly on the magnetic field. Below (see Sec. V A 1) we calculate the electric dipole transition probability using the presented theory of the dynamic DM effect, and compare it to our measurement results.

An important question to answer is which component of light, $\mathbf{E}_1$ or $\mathbf{H}_1$, interacts with the spin system. What is common for the data presented in Fig. 11 is that all these measurements were done with the light polarized along the ladder rungs, $\mathbf{E}_1\|\mathbf{a}$. We made complementary measurements rotating the incident light's polarization by 90°, thus interchanging the orientations of $\mathbf{E}_1$ and $\mathbf{H}_1$, and found that the singlet to triplet transition was at least ten times weaker if $\mathbf{E}_1\perp\mathbf{a}$. While the data presented in panels (a), (b), and (d) of Fig. 11 still leave open the possibility that the singlet to triplet transition could be a magnetic dipole transition where $\mathbf{H}_1\|\mathbf{b}$, there are two other observations that contradict this. *First*, in Fig. 11(c) $\mathbf{H}_1$ is not parallel to the *b* axis while $\mathbf{E}_1$ is still parallel to the *a* axis and the transition is still strong. *Second*, in Fig. 13 two spectra with $\mathbf{H}_1\|\mathbf{b}$ are presented for the $\mathbf{B}_0\|\mathbf{a}$ applied magnetic-field orientation. The upper curve with $\mathbf{E}_1\|\mathbf{c}$ shows about ten times weaker absorption on the singlet to triplet transition than the lower curve with $\mathbf{E}_1\|\mathbf{a}$. Since the same orientation of $\mathbf{H}_1$ gives different intensities the orientation of magnetic-field component of light is irrelevant. Summarizing the results presented in Figs. 11 and 13 we conclude that the strongest contribution to the singlet to triplet absorption comes from an electric dipole transition with the dipole moment along the *a* axis.

There are other contributions to the singlet to triplet absorption, although much weaker than in $\mathbf{E}_1\|\mathbf{a}$ polarization, as is shown in Fig. 13. The upper spectrum is for the *c*-axis polarized light. Two vertical dashed lines mark the area

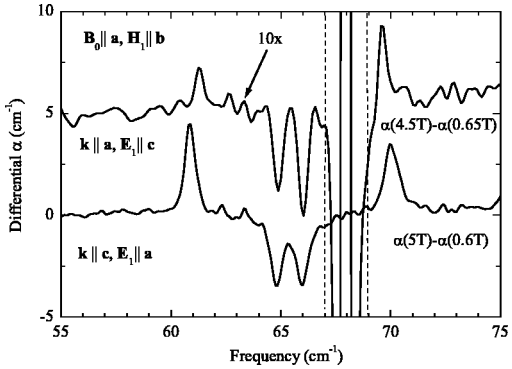

FIG. 13. Differential absorption spectra of the singlet to triplet transition at 4.4 K in $\mathbf{E}_1\|\mathbf{a}$ and $\mathbf{E}_1\|\mathbf{c}$ polarizations. The $\mathbf{E}_1\|\mathbf{c}$ spectrum has been multiplied by 10 and offset in the vertical direction. Both spectra have been measured in $\mathbf{B}_0\|\mathbf{a}$, $\mathbf{H}_1\|\mathbf{b}$ geometry.

where the strong absorption due to the 68 cm^{-1} excitation takes place in this polarization (see also Fig. 6). One can see that the absorption lines closer to the 68 cm^{-1} excitation are stronger than the lines further away.

The line areas measured in different geometries as a function of magnetic-field strength are plotted in Fig. 14. We used the method of differential absorption, where spectra taken in different magnetic fields are subtracted from each other to detect weak transitions. In this differential method the transition from the singlet state to the $m_S=0$ triplet state escapes detection (unless the intensity depends on the field) since the energy of this triplet level does not change with magnetic field. Therefore, only the intensities of the transitions to the $m_S=-1$ and $m_S=1$ triplet levels can be detected and are plotted in Fig. 14. An interesting finding is the enhancement of the singlet to triplet transition in $\mathbf{E}_1\|\mathbf{c}$ polarization close to the 68 cm^{-1} excitation. It is natural to associate the oscillator strength of this weak transition with the interaction between the spins and the 68 cm^{-1} excitation, which has a dipole moment along the c axis. The exception is $\mathbf{B}_0\|\mathbf{b}$ orientation where there is no enhancement in $\mathbf{E}_1\|\mathbf{c}$ polarization. In this field direction only the transition to the $m_S=0$ level has a nonzero oscillator strength but is not detected because of the measurement method.

Besides the strong $\mathbf{E}_1\|\mathbf{a}$ absorption and the resonantly enhanced $\mathbf{E}_1\|\mathbf{c}$ absorption there is a field-independent oscillator strength, as is seen in Fig. 14(a). No polarization anisotropy is observed there in contrary to the first two mechanisms of singlet to triplet transitions that can be recognized by their polarization dependence. In high fields the transitions to the $m_S=-1$ and $m_S=1$ levels have the same strength in $\mathbf{E}_1\|\mathbf{b}$ and $\mathbf{E}_1\|\mathbf{c}$ polarizations [Fig. 14(a)]. When $\mathbf{B}_0\|\mathbf{c}$ and $\mathbf{E}_1\|\mathbf{b}$ [Fig. 14(b)] the intensity of the transitions to the $m_S=-1$ and $m_S=1$ levels is zero and in this configuration the transition to the $m_S=0$ level is active. More detailed analysis of this mechanism is given in Sec. V A 3 where we associate this with a magnetic dipole transition.

Within the error limits the g factors of the triplet state are the same for the two in-plane field orientations $g_a=1.96\pm0.02$, $g_b=1.975\pm0.004$. The fit of the resonance frequencies of the singlet to triplet transition for the third field orientation, $\mathbf{B}_0\|\mathbf{c}$, gives $g_c=1.90\pm0.03$.

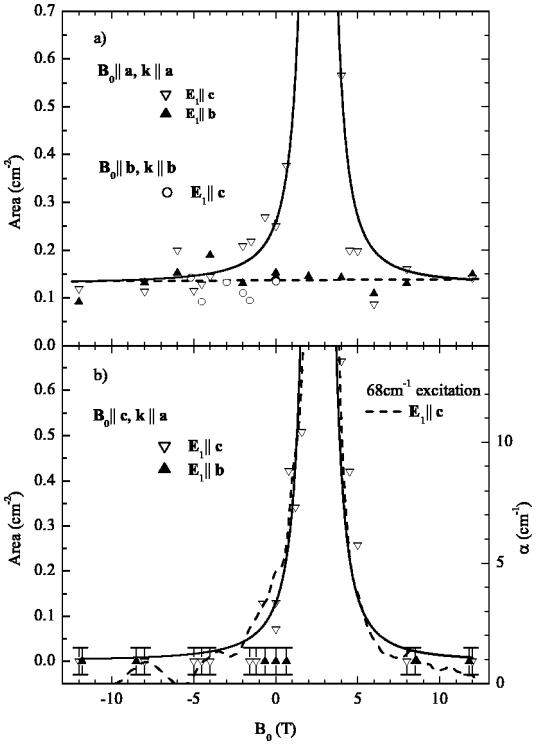

FIG. 14. The magnetic-field dependence of the singlet to triplet transition line area at 4.4 K in two polarizations, $\mathbf{E}_1\|\mathbf{c}$ (empty symbols) and $\mathbf{E}_1\|\mathbf{b}$ (filled triangles). The line areas are plotted in the negative field direction for the transition to the $m_S=-1$ triplet level and for the transition to $m_S=1$ in the positive field direction. The zero-field data points on the graph are one-half of the measured area. (a) $\mathbf{B}_0\|\mathbf{a}$ and $\mathbf{B}_0\|\mathbf{b}$. (b) $\mathbf{B}_0\|\mathbf{c}$. The dashed line in (a) is a guide for the eye. The dashed line in (b), units on the right axis, is the 68 cm^{-1} absorption line shape with the background subtracted and the energy units converted into magnetic-field units using the triplet state g factor, $g_c=1.90$. The error bars shown only in (b) apply to data points in both panels. A solid line in (b) is a fit to the dynamic DM mechanism induced by the 68 cm^{-1} phonon. The oscillator strength of the phonon and the singlet to triplet transition in zero field are 400 cm^{-2} and 0.13 cm^{-2}, respectively. The only fit parameter is the dynamic DM interaction, $qD_Q=0.13$ cm^{-1}.

In zero field the triplet levels $m_S=-1,0$, and 1 are degenerate; it is best seen when comparing the zero-field line positions in Figs. 11(c) and 11(d). Determining the size of the zero-field splitting is limited by the linewidth. We can say that the zero-field splitting of the triplet levels is less than half of the linewidth, $\gamma/2=0.25$ cm^{-1}.

V. DISCUSSION

A. Triplet state and Dzyaloshinskii-Moriya interaction

In this section we analyze three different contributions to the singlet to triplet optical absorption observed experimentally in α'-NaV_2O_5. Two of them fall into the same category, the electric dipole active dynamic DM mechanism. The third contribution is probably due to the static DM in-

teraction mechanism where magnetic dipole transitions are active, but cannot be explained with a single-dimer model.

We rule out a possible singlet to triplet absorption mechanism based on a staggered g factor. The staggered g-factor mechanism requires that the principal axes of the g tensors of a pair of spins with anisotropic g factors must not coincide. Let us consider for an example the spin $\mathbf{S}_1$ with its principal axes rotated from the crystal a axis by an angle θ and the spin $\mathbf{S}_2$ by an angle $-\theta$ and $\mathbf{B}_0 \| \mathbf{a}$. Let the Hamiltonian contain isotropic exchange interaction $J\mathbf{S}_1 \cdot \mathbf{S}_2$ and Zeeman interaction $\mathbf{B}_0 \cdot (\tilde{\mathbf{g}}_1 \cdot \mathbf{S}_1 + \tilde{\mathbf{g}}_2 \cdot \mathbf{S}_2)$. Matrix elements between the singlet and triplet states equal to $\pm B_0(g_a - g_b)\sin\theta\cos\theta$ appear. It is important that the singlet-triplet mixing is proportional to B_0. *First*, there is no mixing in zero field ($B_0 = 0$) and the staggered g-factor mechanism is turned off. *Second*, the transition probabilities increase as $(B_0)^2$ if the magnetic field is small compared to the separation of the singlet and triplet states. In the experiment we observe a singlet to triplet transition in zero field, and also the observed magnetic-field dependence is different from that of the staggered g-factor mechanism. Therefore this mechanism does not apply to the singlet-triplet transitions in α'-NaV_2O_5.

1. Dynamic Dzyaloshinskii-Moriya: $\mathbf{E}_1 \| \mathbf{a}$

The strongest singlet to triplet absorption is observed in $\mathbf{E}_1 \| \mathbf{a}$ polarization. There is no resonant enhancement in the magnetic-field dependence of the line area as seen in Fig. 12 and any of the optically active excitations in $\mathbf{E}_1 \| \mathbf{a}$ polarization is a candidate that can create the dynamic DM interaction. Nevertheless we can make some choices. The 91 cm^{-1} a-axis phonon is not active since no enhancement is observed when the upper branch of the triplet resonance crosses the phonon frequency at 28 T (Fig. 12) although there is an interaction between this phonon and the continuum of magnetic excitations as is manifested by the Fano line shape of the phonon line above T_c (Fig. 5).

In Fig. 12 we have plotted two fit curves based on perturbation calculation results [Eqs. (13) and (14)]. In one case the phonon frequency was fixed to 518 cm^{-1} that is the strongest a-axis optical phonon.[31] In the other case the phonon frequency was a fitting parameter giving us (180 ± 10) cm^{-1}. This value represents the lowest boundary for the frequency of the DM phonon. Phonons with lower frequencies would give a too steep magnetic-field dependence of the singlet to triplet transition probability. It is likely that the lowest boundary of the phonon frequency has been underestimated since the three high-field data points above 30 T influence the fit by lowering the phonon frequency. Additional measurements above 33 T are required to clarify this intensity enhancement. Based on these fits the strength of the dynamic DM interaction qD_Q can be obtained. The closest low-T phase infrared-active a-axis phonon in frequency to 180 cm^{-1} is the 199 cm^{-1} zone-folded phonon.[31] The plasma frequencies Ω_p of the 199 cm^{-1} and 518 cm^{-1} phonons are 48 cm^{-1} (Ref. 32) and 853 cm^{-1} (Ref. 33), respectively. We convert the plasma frequency into the line area in absorbance units, $\int \alpha(\omega) d\omega$, using $\int \alpha(\omega) d\omega = \pi^2 \Omega_p^2 / n_a$. From the fit results we calculate $qD_Q = 5$ cm^{-1} for the 199 cm^{-1} phonon and $qD_Q = 0.9$ cm^{-1} for the 518 cm^{-1} phonon.

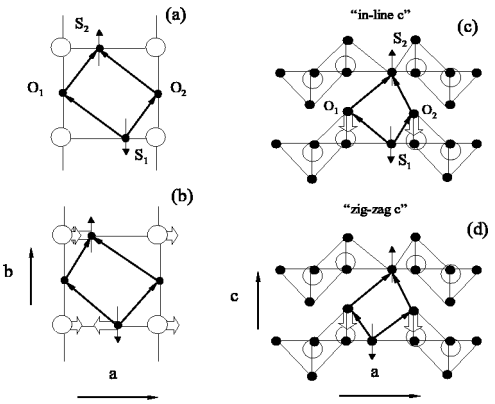

FIG. 15. Cartoons of superexchange paths in the ab plane [panels (a) and (b)] with one ladder shown and in the ac plane [(c) and (d)] with two ladders shown. For illustrative purposes it is assumed that the spin is located on the rung oxygen. Oxygens are shown by filled circles and vanadium atoms by open circles. Block arrows show the displacement of atoms due to a phonon. (a) Superexchange paths between two spins over on-leg oxygens within the same ladder in the zigzag ordered phase; (b) same superexchange paths when an a-axis phonon is involved; (c) superexchange paths between two spins in the neighboring planes over apical oxygens displaced by a c-axis phonon when spins are in-line along c axis or (d) zigzag.

The orientation of the DM vector is determined by the vector product of the vectors connecting two spins over the superexchange path[34,35]

$$\frac{\mathbf{D}}{|\mathbf{D}|} = [\mathbf{R}_{S_1,O_i} \times \mathbf{R}_{O_i,S_2}]. \tag{16}$$

In the zigzag ordered low-T phase two superexchange paths exist, one over on-leg oxygen O_1 and the other over O_2, shown in Fig. 15(a). The resultant DM vector is zero since the two DM vectors, pointing in **c** direction, cancel each other. The zero length of the DM vector follows from the general arguments of symmetry too as in this particular case there exists a local center of inversion located between two V-O-V rungs. The 518 cm^{-1} a-axis phonon displaces on-rung oxygens along the rung (on-rung V-O-V stretching mode),[36] Fig. 15(b). Because of the phonon the two superexchange paths are not"equal" anymore and the resulting DM vector points along the c axis. The orientation of the dynamic DM vector, $\mathbf{D}_Q \| \mathbf{c}$, is consistent with the selection rules for the dynamic DM interaction observed experimentally. The transition to the $|t_0 0\rangle$ is observed when $\mathbf{B}_0 \| \mathbf{D}_Q$, Fig. 11(d). The transitions to the $|t_- 0\rangle$ and $|t_+ 0\rangle$ states are observed when $\mathbf{B}_0 \perp \mathbf{D}_Q$, Figs. 11(a)–11(c).

There is another phonon with an oscillator strength larger than that of the 518 cm^{-1} a-axis phonon. That is the 582 cm^{-1} b-axis phonon that stretches on-leg V-O-V bonds.[31,33] In the high-T phase where electron charge (and spin) is rung centered, such distortion does not produce any DM interaction from the principles of symmetry. In the low-T phase the charges are ordered in a zigzag pattern. The

on-leg V-O-V bond-stretching phonon lowers the symmetry and creates the DM interaction along the *c* axis. We do not observe a singlet to triplet absorption with an electric dipole moment along the *b* axis in the experiment. There are two possibilities why the $\mathbf{E}_1\|\mathbf{b}$ absorption is not observed. *First*, there is no zigzag charge order. *Second*, there is a zigzag charge order and although the dynamic DM is allowed by symmetry, the actual value of qD_Q is small and the absorption cannot be observed in our experiment. Since there is a mounting evidence in the favor of a low-T zigzag charge order[7,8,11] we consider the second case likely.

2. Dynamic Dzyaloshinskii-Moriya: $\mathbf{E}_1\|\mathbf{c}$

The singlet to triplet absorption with the electric dipole moment along the *c* axis is due to the dynamic DM interaction. In this particular case the dynamic DM mechanism is brought in by the 68 cm^{-1} optically active *c*-axis phonon. The enhancement of the singlet-triplet absorption close to the 68 cm^{-1} line is present if the magnetic field is either parallel to *a* or *c* axis, but missing if the field is along the *b* axis. In Sec. V C we present further arguments supporting the assignment of the 68 cm^{-1} resonance to a phonon and not to a magnetic excitation.

In Fig. 14 the fit of the singlet to triplet transition intensities to the dynamic DM absorption mechanism is shown. The input parameters are the resonance frequency of the phonon, $\omega_p = 68$ cm^{-1}, and the frequency of the singlet to triplet transition as the function of magnetic field, $\omega_{T_\pm} = \Delta \pm g\mu_B B_0$, where $\Delta = 65.4$ cm^{-1}. We estimated the low-temperature oscillator strength of the phonon from the T dependence presented in Fig. 10 and got $\Omega_p^2 = 400$ cm^{-2}. The ratio of the singlet to triplet absorption oscillator strength Ω_{ST}^2 to the oscillator strength of the phonon, Ω_p^2, is $\Omega_{ST}^2/\Omega_p^2 \sim 0.13/400 = 3.3\times10^{-4}$. The only fit parameter is the strength of the dynamic DM interaction, $qD_Q = 0.13$ cm^{-1}.

We used $\mathbf{D}_Q\|\mathbf{b}$ in our fit because the splitting of the triplet in the magnetic field is observed if $\mathbf{B}_0\|\mathbf{a}$ or $\mathbf{B}_0\|\mathbf{c}$ (Fig. 14). According to the selection rules for the dynamic DM only the transitions to the triplet states with $m_S = 1$ and $m_S = -1$ are observed when the magnetic field is perpendicular to the dynamic DM vector $\mathbf{D}_Q \perp \mathbf{B}_0$. The selection rules for the dynamic DM if $\mathbf{B}_0\|\mathbf{D}_Q\|\mathbf{b}$ allow only transitions to the $m_S = 0$ level that does not shift with the magnetic field and we do not see it in the differential absorption spectra that are taken in different magnetic fields. The background intensities that do not depend on the magnetic field in Fig. 14(a) are analyzed in the following (Sec. V A 3).

Which lattice deformations along the *c* axis (electric dipole) will give the dynamic DM interaction in the *b*-axis direction? It turns out that we have to consider interplane interactions. For the beginning let us consider two spins on the neighboring rungs, as shown in Fig. 15(a), where optical *c*-axis phonons have the out-of (ab) plane antiphase movements of oxygen and vanadium atoms. In the low-T zigzag ordered phase the dynamic DM vector will have components along both, *a* and *b* axis. The *b*-axis component of the dynamic DM turns to zero for a vanishing zigzag order, i.e., in the limit of rung-centered spin distribution. The *a*-axis component stays nonzero. To get a dynamic DM exclusively along the *b* axis we have to consider interactions between the spins in the neighboring planes. Here the path for the DM interaction between spins in the neighboring planes goes over the apical oxygens. Two arrangements along the *c* axis are possible in the zigzag ordered phase, shown in Figs. 15(c) and 15(d): in-line or zigzag. In both arrangements the displacement of the apical oxygens in the **c** direction will create a dynamic DM along the *b* axis. As one can see not only the dynamic, but also the static DM in the **b** direction is allowed by the symmetry.

In the experiment we do not see magnetic dipole active optical transitions caused by the static DM interaction. To compare the strength of magnetic and electric dipole transitions we must know the magnitude of the static DM interaction. The magnitude of the DM interaction was estimated by Moriya,[21] $D \approx (|g - g_e|/g_e)J$, where J is isotropic exchange interaction and $g_e = 2$ is the free-electron g factor. We use $g = 1.90$ and $J = 60$ meV (from Ref. 14) and get $D = 25$ cm^{-1}. The transition intensity I is proportional to $(|V|/\delta\mathcal{E})^2$ where $|V|$ is the matrix element of the interaction (D or qD_Q) between the two states and $\delta\mathcal{E}$ is their energy separation. For the static DM effect $\delta\mathcal{E}$ is the singlet-triplet gap, $\delta\mathcal{E} = 65.4$ cm^{-1}; for the dynamic DM it is the energy difference between the phonon energy and the triplet level, $\delta\mathcal{E} = 68 - 65.4 = 2.6$ cm^{-1}. The intensity of the magnetic dipole transition is weaker than the electric dipole transition by the factor of $\alpha_f^{-2} = 137^2$, where α_f is the fine-structure constant (see Ref. 37, p. 171). If we use $D = 25$ cm^{-1} and $qD_Q = 0.13$ cm^{-1} we get that the intensity due to the dynamic mechanism is $(0.13\times65.4)^2/(\alpha_f 25\times2.6)^2 \approx 300$ times larger than the intensity due to the static mechanism. Optical transitions due to the static DM interaction are suppressed with respect to the transitions caused by the dynamic DM because electric dipole transitions are stronger than magnetic dipole transitions.

Our conclusion is that the dynamic DM interaction along the *b* axis, $qD_Q = 0.13$ cm^{-1}, is between the spins on the ladders of the neighboring planes. The 68 cm^{-1} *c*-axis phonon that creates the dynamic DM interaction involves the displacement of apical oxygens.

3. Third optical singlet-triplet absorption mechanism

There is a third mechanism for the optical triplet absorption that is responsible for the magnetic-field-independent intensities of the transitions to the $m_S = -1$ and $m_S = 1$ triplet levels, shown in Fig. 14(a) by solid triangles and empty circles. The same mechanism contributes together with the enhanced part discussed in the preceding section to the intensity plotted with empty triangles on the same graph.

We could assume that the third mechanism is also an electric dipole absorption mechanism as the two mechanisms ascribed to the singlet-triplet absorption in $\mathbf{E}_1\|\mathbf{a}$ and $\mathbf{E}_1\|\mathbf{c}$ polarizations. Since this absorption is present in both polarizations $\mathbf{E}_1\|\mathbf{b}$ and $\mathbf{E}_1\|\mathbf{c}$ one has to assume that the electric dipole moment is either in the (bc) plane or, just by coincidence, two electric dipole mechanisms, one polarized along

the b axis and the other polarized along the c axis, give the same intensities. The case that the optical phonon responsible for the dynamic DM effect has a dipole moment in the (bc) plane contradicts with the data available on phonons and with the crystal symmetry. The second case of coinciding intensities is ruled out by the selection rules if applied to the full data set presented in Figs. 14(a) and 14(b).

The third mechanism could be a magnetic dipole DM mechanism. By applying the selection rules to the data we should be able to determine the orientation of the DM vector. According to the theory (Sec. II A) transitions to the $m_S=-1$ and $m_S=1$ states have constant and equal intensities when $\mathbf{B}_0\|\mathbf{D}$. This condition is satisfied by two data sets, solid triangles ($\mathbf{H}_1\|\mathbf{c}$), and empty triangles ($\mathbf{H}_1\|\mathbf{b}$) in Fig. 14(a), measured with $\mathbf{B}_0\|\mathbf{a}$. We have $\mathbf{D}\|\mathbf{a}$, where $I_x^{\pm}=I_y^{\pm}$ and $x\equiv b$ and $y\equiv c$ (see Fig. 1). However the set represented by the circles in Fig. 14(a) is the $I_y^{\pm}$ intensity in the perpendicular configuration, $\mathbf{B}_0\perp\mathbf{D}$ (in our notation $\mathbf{D}\|\mathbf{y}\|\mathbf{a}$), which should have zero intensity according to the theory (see Fig. 2). Also, in the $\mathbf{B}_0\|\mathbf{H}_1\|\mathbf{c}$ configuration $I_z^{\pm}$ should have nonzero intensities. In the experiment, filled triangles in Fig. 14(b), no intensity is observed contrary to the theory. Therefore the assumption $\mathbf{D}\|\mathbf{a}$ is not consistent with the full data set. Also, we can prove that neither $\mathbf{D}\|\mathbf{b}$ nor $\mathbf{D}\|\mathbf{c}$ is fully consistent with the experiment.

Our conclusion is that the third optical triplet absorption mechanism is a magnetic dipole transition, but cannot be explained by an isolated dimer model with DM interactions. Apparently, a more elaborate model including the interdimer DM interactions, is necessary.

B. Spin gap and phase transition

We studied the effect of temperature and magnetic field on the singlet to triplet transition. The results are shown with circles in Fig. 8. We observe that the intensity of the singlet to triplet transition [Fig. 8(a)] follows the intensity of the x-ray-diffraction peak[38] reported in the same figure. Gaulin *et al.* have shown that the intensity of the x-ray-diffraction peak can be fitted with a single function $I=t^{\beta}$ over the reduced temperature, $t=1-T/T_c$, in the range from 6×10^{-3} to 2×10^{-2} with the critical exponent $\beta=0.18$. Our data taken below 30 K are above 1.1×10^{-1} in the reduced temperature scale, which is unsuitable for the determination of the critical exponent.

The singlet-triplet splitting (spin gap), shown in Fig. 8(b), is more rigid than the singlet to triplet transition probability or the x-ray scattering intensity. The rigidity of the spin gap has been confirmed earlier by INS measurements[3] and by high-field electron-spin-resonance measurements, although not in the zero magnetic field.[16] The far-infrared S to T gap is in agreement with the INS gap also shown in Fig. 8(b). In the ultrasonic experiment[39] the measurements were extended close enough to T_c that one is able to determine the critical exponent for the spin gap. The temperature dependence of the spin gap, measured indirectly by the ultrasonic probe, gives the critical exponent $\beta=0.34$ below the reduced temperature 10^{-2}. Although far-infrared measurements of the gap are direct, reasonable data can be obtained only too far from T_c as the absorption line broadens and gets weak and therefore the fit, inset to Fig. 8(b), gives us an exceptionally low critical exponent, $\beta=0.039\pm0.002$.

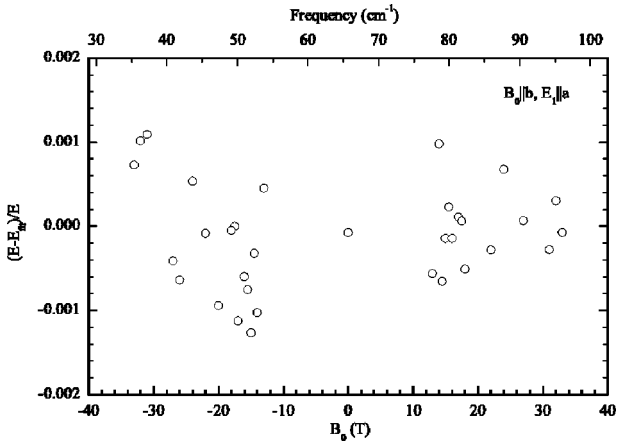

FIG. 16. Relative deviation $(E-E_{fit})/E$ of S to T_{-1} (plotted at negative field values) and S to T_{+1} (plotted at positive field values) transition energy E from the linear fit E_{fit}.

The magnetic-field dependence of the spin gap and the triplet state g factor have been measured up to 33 T for one field orientation, $\mathbf{B}_0\|\mathbf{b}$, at 4.7 K. The line positions of the transitions from the singlet ground state to the triplet states with $m_S=\pm1$ were fitted with a linear function $E_{fit}=\Delta\pm g\mu_B B_0$. The reduced residual of the linear fit is less than 0.0012 of the transition energy, as shown in Fig. 16. This means that the triplet state g factor is not renormalized by the magnetic field as high as 33 T and the spin gap is independent of the field up to 33 T. The independence of the gap value Δ on the field at low temperature is not surprising.[40] The role of the magnetic field is to couple to thermally excited quasiparticles. At low temperature the number of quasiparticles is small and hence the effect of the magnetic field is negligible.

In conclusion, the temperature dependence of the intensity of the singlet to triplet transition agrees with the x-ray scattering intensity temperature dependence. Also, the singlet-triplet splitting at 8.13 meV has the same temperature dependence as the singlet-triplet splitting of the second excitation branch at 9.8 meV measured by the INS. The 8.13 meV spin gap is not altered by the magnetic field at least up to 33 T.

C. Phonons and phase transition

1. C-axis phonons

In Sec. V A 2 while calculating the dynamic DM interaction for $\mathbf{E}_1\|\mathbf{c}$ we assumed that the electric dipole moment of the c-axis polarized optical singlet to triplet transition comes from the interaction between the spin system and the 68 cm^{-1} optical c-axis phonon. An alternative would be that the 68 cm^{-1} resonance is not a phonon but a singlet electronic excitation. Here we analyze existing data and show that the data are not in contradiction with the assumption that the 68 cm^{-1} resonance is a phonon mode.

There is a series of infrared-active c-axis modes appearing below 34 K as shown in Fig. 6 and found by other

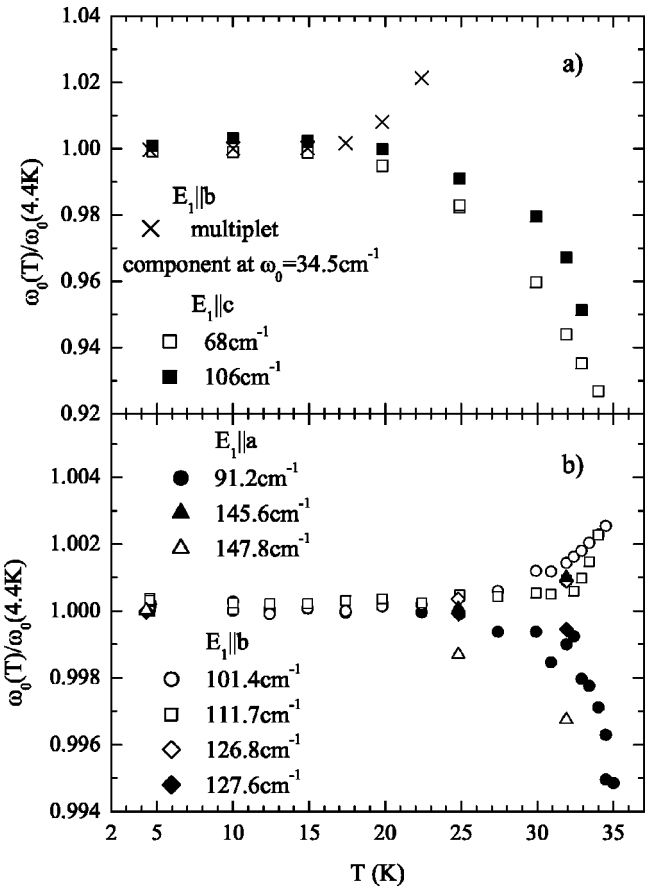

FIG. 17. Temperature dependence of normalized phonon frequencies. (a) *b*-axis multiplet and *c*-axis phonons, (b) *a*- and *b*-axis phonons.

groups.[32,41] The two low-frequency modes, at 68 and 106 cm^{-1}, are the strongest. The temperature dependence of their resonance frequencies plotted in Fig. 17(a) is an order of magnitude larger as compared to the *a*- and *b*-polarized modes plotted in Fig. 17(b). Modes at frequencies close to 68 and 106 cm^{-1} have been found by Raman spectroscopy.[42,43] Sample dependence of mode frequencies by few wave numbers has been observed both in infrared[32] and Raman.[43] It is known that Na deficiency of α'-$Na_xV_2O_5$ affects T_c and in samples where $x=0.97$ the phase transition is suppressed completely.[44] A Na doping dependence study[43] has shown that the frequency variation of Raman modes from sample to sample is related to the Na content of the sample. Raman measurements[45] on the sample from the same batch as the one studied here gave values for the mode frequencies 65.9 and 105 cm^{-1} at 4.4 K. This means that Raman and infrared spectroscopy observe different modes since the frequencies of infrared modes are 68 and 106 cm^{-1}. Neither of the Raman modes[42,43] nor the infrared modes (this work and Ref. 41) split in the magnetic field. The comparison of the *T* dependence of the normalized mode frequency has shown that the *T* dependence of the 65.9 cm^{-1} Raman mode follows the *T* dependence of the 68 cm^{-1} infrared mode and the 105 cm^{-1} Raman mode follows the *T* dependence of the 106 cm^{-1} infrared mode. Therefore, although the infrared and the Raman modes do not have the same frequencies, it is likely that the origin of the infrared and Raman modes near 68 and 106 cm^{-1} is the same, lattice modes or electronic excitations.

The origin of the low-frequency infrared and Raman modes has been under the debate. It has been concluded that the Raman modes are not lattice vibrations.[42,43] In Ref. 32 the conclusion was that the infrared modes at 68 and 106 cm^{-1} are zone-folded *c*-axis phonons and it was speculated that their peculiar *T* dependence compared to other zone-folded phonon modes is caused by the interaction of phonons with charge and spin degrees of freedom. Indeed, the 68 cm^{-1} mode and the singlet to triplet excitation at 65.4 cm^{-1} have similar *T* dependencies of their infrared absorption line parameters as shown in Fig. 8. Assuming that 68 and 106 cm^{-1} excitations are zone-folded phonons we would have to explain why their frequencies depend on Na deficiency and why their frequencies have a different temperature dependence than the other zone-folded modes have. We argue that both points can be explained if charge correlations develop inside ladder planes prior to the transition to the low-*T* phase and at the phase transition three-dimensional correlations build up between the planes.

Charge ordering within ladder planes precedes the lattice distortion and the opening of the spin gap as evidenced by the vanadium Knight shift and the sodium quadrupolar and Knight shifts.[10] The presence of two-dimensional charge correlations in the ladder planes above 35 K is also supported by the x-ray-diffraction measurements.[38] In α'-NaV_2O_5 there are modulated ladders with a zigzag charge order within one plane.[7,9,10] It is possible to construct four different planes with the zigzag charge order and when stacked in certain sequence along the *c* axis a unit cell is formed compatible with the observed x-ray structure.[8,11] By applying pressure the critical temperature is reduced and it has been found that the soft axis is the *c* axis.[27,46] A ''devil's-staircase-like'' sequence of phase transitions to the phases with unit cells incorporating more than four planes in the *c* direction takes place under pressure larger than 0.5 GPa.[12] Therefore the interactions between layers are important in the formation of three-dimensional correlations.

Interactions between ladder planes are important for those modes, which are zone folded along the *c* axis. The primary candidates are the modes with antiphase movements of atoms along the *c* axis in the neighboring planes, which are naturally the modes that are polarized along the *c* axis. The *c*-axis modes have the largest frequency shift close to the phase-transition point. The exception is the *b*-polarized multiplet (Fig. 9). It is the only non-*c*-axis low-frequency mode, which has a relative change of frequency with temperature [Fig. 17(a)] that is comparable to the *c*-axis modes. Considering the low frequency of the multiplet it is likely that the seven lines are a result of the folding of a *b*-polarized acoustical, not optical-phonon branch. To get seven optical-phonon branches out of one phonon branch a *c*-axis folding is required in addition to *a*- and *b*-axis foldings. Therefore this multiplet involves relative movements of atoms in neighboring layers and is a subject to interlayer couplings.

Our conclusion is that the *c*-axis phonon modes are most susceptible to three-dimensional correlations between ladder

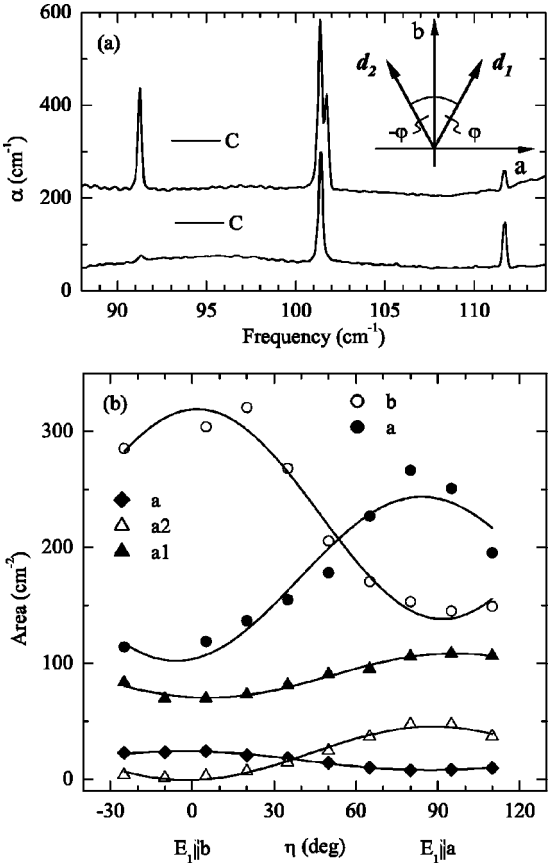

FIG. 18. Polarization dependence of low-frequency phonon absorption line intensities. (a) Absorption spectra in $\mathbf{E}_1\|\mathbf{a}$ (shifted upwards by 150 cm^{-1}) and $\mathbf{E}_1\|\mathbf{b}$ polarizations. (b) Absorption line areas as a function of polarization angle in the (ab) plane; $\eta=0$ corresponds to $\mathbf{E}_1\|\mathbf{b}$. Inset to (a) shows the orientation of electric dipoles rotated from the b axis by an angle φ and $-\varphi$.

planes and therefore their T dependence is different from other low-frequency phonon modes. We assign the 68 cm^{-1} (and 106 cm^{-1}) infrared-active mode and the 66 cm^{-1} (and 105 cm^{-1}) Raman active modes to the zone-folded phonons.

2. Polarization dependence of line intensities

In NaV_2O_5 the a- and b-axes are not equivalent and one would expect the selection rules to apply so that the phonon active in the $\mathbf{E}_1\|\mathbf{a}$ absorption is missing in $\mathbf{E}_1\|\mathbf{b}$ spectrum and vice versa. In other words, phonons polarized along a axis should have different frequencies than phonons polarized along the b axis.

This rule applies well at 40 K (Fig. 5). The strong 180 cm^{-1} phonon is missing in the $\mathbf{E}_1\|\mathbf{a}$ spectrum and the structure at 140 cm^{-1} is missing in the $\mathbf{E}_1\|\mathbf{b}$ spectrum. The 90.7 cm^{-1} line is present only in the $\mathbf{E}_1\|\mathbf{a}$ spectrum.

At 4.4 K this selection rule does not apply to all absorption lines. The 101.4 and 111.7, 126.7 and 127.5 cm^{-1} phonons [Figs. 18(a) and 5] have absorption in both polarizations. The leakage of the wrong polarization through the polarizer is ruled out. For example, the 101.7 cm^{-1} line present in $\mathbf{E}_1\|\mathbf{a}$ spectrum is missing in $\mathbf{E}_1\|\mathbf{b}$ spectrum [Fig. 18(a)] and the multiplet at 30 cm^{-1} is missing in $\mathbf{E}_1\|\mathbf{a}$ spectrum (Fig. 5).

TABLE II. Rotation angle φ calculated from the two dipole model. φ_a (φ_b) is the rotation angle of the phonon dipole moment from the crystal a axis (b axis).

ω_0 (cm^{-1})	101.4	101.7	111.7	126.8	127.5
$\varphi_b\equiv\varphi$			32		35
$\varphi_a=90°-\varphi$	37	0		31	

We measured the polarization dependence of line intensities in the (ab) plane. The areas of absorption lines between 100 and 130 cm^{-1} are plotted in Fig. 18(b) as a function of the angle η between the polarizer and the b axis. The lines at 91 cm^{-1} were not included since they are two different lines, one at 91.2 cm^{-1} in the a polarization and the other at 91.3 cm^{-1} in the b polarization. As the 101.7 cm^{-1} line has zero intensity at $\eta=0°$, $\mathbf{E}_1\|\mathbf{b}$ it belongs to the phonon modes representing the averaged crystal symmetry. It is important that the intensity of the 101.4 cm^{-1}, 111.7 cm^{-1}, 126.7 cm^{-1}, and 127.5 cm^{-1} lines never falls to zero between $\eta=0°$ and 90°. A similar effect was found by Damascelli *et al.*[31] for several infrared-active phonons at higher frequencies. The simplest explanation would be that the zone-folded a- and b-polarized phonons are pairwise degenerate, but then it is hard to explain why there is a constant intensity ratio of at least four pairs of low frequency and of one high-frequency (718 cm^{-1}) pair of a- and b-axis phonons, as is shown below.

We assume, as was done in Ref. 31, that there are two regions in the crystal with a symmetry different from the averaged crystal symmetry. In one region the electric dipole moment of a phonon, **d**, is rotated from the crystal b axis by an angle φ and in the other region by $-\varphi$ as shown in the inset to Fig. 18(a). The optical conductivity in the first region is $\sigma_1(\varphi)=aE_1^2d^2\cos^2(\varphi-\eta)$, where a is a constant independent of angular parameters. η is the angle between the b axis and the electric-field vector of light $\mathbf{E}_1$. The conductivity in the second region is $\sigma_1(-\varphi)=aE_1^2d^2\cos^2(\varphi+\eta)$. Since the phonons are independent in the two regions the total observed conductivity is $\sigma_1=\sigma_1(\varphi)+\sigma_1(-\varphi)=I_b\cos^2\eta+I_a\sin^2\eta$, where $I_b=2aE_1^2d^2\cos^2\varphi$ and $I_a=2aE_1^2d^2\sin^2\varphi$ are the oscillator strengths observed in the experiment in the b and a polarizations, respectively. The solid lines in Fig. 18(b) are the fits of the integrated absorption line areas where Eq. (15) has been used to convert $\alpha(\omega)$ into $\sigma_1(\omega)$. The results are given in Table II. Note that two of the absorption lines belong to the dipoles rotated from the a axis and two to the dipoles rotated by approximately the same angle from the b axis. The averaged value of the rotation of the dipole moment is $\bar{\varphi}=34°\pm3°$. A similar result, $\varphi=39°$, we obtain for the 718 cm^{-1} phonon using the data from the Ref. 31 where the given oscillator strength in the $\mathbf{E}_1\|\mathbf{a}$ polarization is 0.021 and in the $\mathbf{E}_1\|\mathbf{b}$ polarization is 0.014.

The two regions with a symmetry that is different from the crystal symmetry can be associated with two types of ladder planes with a zigzag charge order. In Ref. 31 it was

assumed that the crystal is split into domains with two different diagonal charge patterns. Considering the recent x-ray studies[8,11] it is more likely that there are no domains and two types of planes exist with different diagonal charge pattern instead. The two different charge configurations come from the way the two neighboring zigzag charge ordered ladders are positioned with respect to each other within the plane. A shift of every second ladder by one-half of the superlattice constant in the **b** direction creates two different structures where charged stripes of $V^{+4.5-\delta_c/2}$ run diagonal from left to the right or from right to the left in the (ab) plane.[11] This diagonal charge order within a single plane determines the orientation of the phonon dipole moments. It is possible to estimate the charge offset $x=l(1+\delta_c)/2$ from the center of the rung knowing the tilt angle of the dipole moments φ. Here l is the length of the rung and the charge transfer factor δ_c is associated with the formal valence of vanadium ions in the low-T zigzag ordered phase, $V^{+4.5-\delta_c/2}$ and $V^{+4.5+\delta_c/2}$. The charge transfer factor depends only on the angle φ, $\delta_c \approx \tan\varphi$, since the rung length is approximately equal to the distance between the nearest-neighbor V atoms along the leg. We get $\delta_c=0.67\pm0.07$ using $\varphi=\overline{\varphi}$. From the analysis of INS data the authors of Ref. 14 come to a similar value, $\delta_c=0.6$.

Our study of phonon modes in the low-temperature phase supports the view that the symmetry of the individual ladder planes is lower than the averaged crystal symmetry. In addition it has been found by sound velocity measurements[47] that the c_{66} shear mode couples to the pretransitional charge fluctuations of B_{1g} symmetry, which correspond to the static zigzag charge order in the low-T phase. There are phonon modes in α'-NaV_2O_5 in the low-T phase where the normal coordinates are confined into planes. These modes show the symmetry of an individual plane determined by the zigzag charge ordering. For other modes the movement of atoms is correlated between the neighboring planes or they are insensitive to the zigzag charge order and therefore they reflect the averaged crystal symmetry.

From the analysis of the infrared spectra we conclude that two types of planes exist with the zigzag charge order where the charged stripes are aligned approximately in [110] or in $[\overline{1}10]$ directions. The formal charge of the vanadium atoms forming the zigzag pattern is $+4.17\pm0.04$ and $+4.83\pm0.04$.

D. Continuum of excitations and Fano resonances

A broad absorption continuum is observed in $\mathbf{E}_1\|\mathbf{a}$ polarization above T_c that starts gradually below 20 cm^{-1} [Fig. 5(a)] and extends up to 400 cm^{-1} (Ref. 31). The change of the continuum with temperature is correlated with the phase transition at 34 K as demonstrated in Fig. 19 where normalized optical conductivity is plotted for three different frequencies. The continuum absorption at 4.4 K shows a threshold at 130 cm^{-1} in $\mathbf{E}_1\|\mathbf{a}$ polarization while at lower frequencies it is similar to the absorption in $\mathbf{E}_1\|\mathbf{b}$ polarization (Fig. 20). It is natural to associate the absorption continuum with an optical excitation of two triplets since the lowest in energy one triplet excitation is at 65.4 cm^{-1}.

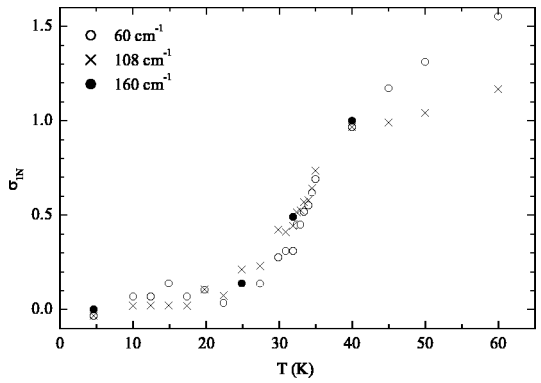

FIG. 19. Temperature dependence of the normalized optical conductivity in $\mathbf{E}_1\|\mathbf{a}$ polarization $\sigma_{1N}=[\sigma_{1a}(T)-\sigma_{1a}(4.4\text{ K})]\times[\sigma_{1a}(40\text{ K})-\sigma_{1a}(4.4\text{ K})]^{-1}$ at 60 (open circles), 108 (crosses), and 160 cm^{-1} (filled circles).

There are two derivativelike phonon absorption lines, one at 91.2 and the other at 140 cm^{-1}, in the $\mathbf{E}_1\|\mathbf{a}$ absorption spectrum above T_c in Fig. 5(a). This line shape, known as the Fano resonance, comes from the interaction of a discrete level and a continuum of states.[48,49] The Fano line shape[49] does not describe a normal absorptionlike line shape. To account for an arbitrary line shape, including the Lorentzian line, we use an empirical formula[50] for the dielectric function $\epsilon(\omega)$ where the asymmetry is described by the phase θ:

$$\epsilon(\omega)=\epsilon_\infty+\frac{\Omega_p^2\exp(-\imath\theta)}{\omega_p^2-\omega^2-\imath\omega\gamma}. \tag{17}$$

Ω_p is the plasma frequency, ϵ_∞ is the background dielectric constant, and ω_p is the resonance frequency of the phonon, and γ is the FWHM of the Lorentzian line at $\theta=0$.

We did a T dependence study of the 91 cm^{-1} line and the evolution of this line with T is shown in Fig. 21. The phonon line at 140 cm^{-1} is on a steeply rising background. Since the frequency dependence of the absorption background is not known it is difficult to subtract the background reliably and we did not attempt to evaluate the T dependence of the

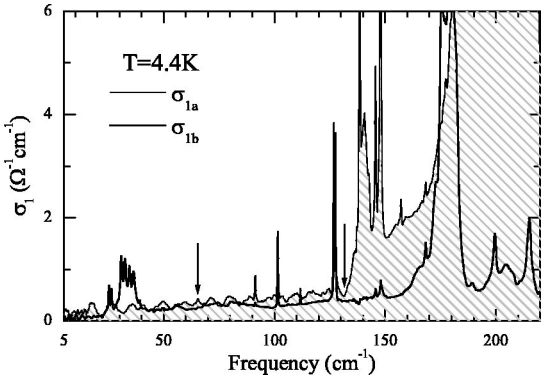

FIG. 20. Real parts of optical conductivities σ_{1a} (shaded and thin line) in $\mathbf{E}_1\|\mathbf{a}$ polarization and σ_{1b} (thick line, $\mathbf{E}_1\|\mathbf{b}$) at 4.4 K. Arrows point to the singlet to triplet resonance at 65.4 cm^{-1} and to the onset of the absorption continuum at 132 cm^{-1} in $\mathbf{E}_1\|\mathbf{a}$ polarization.

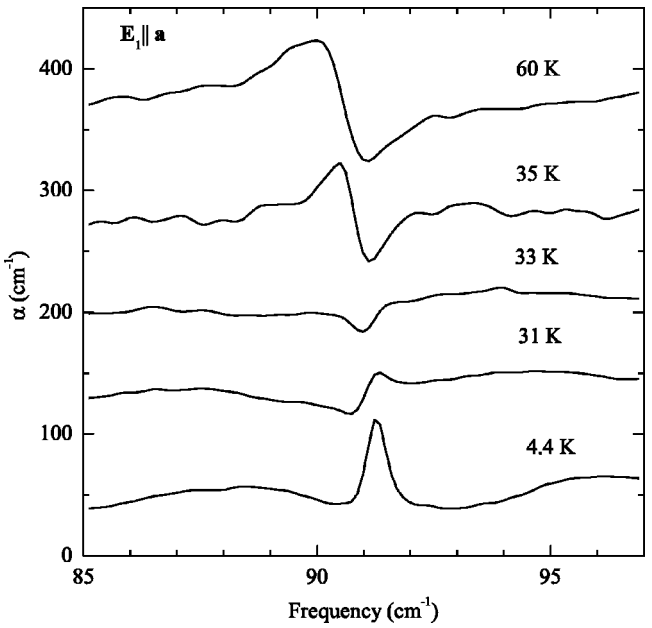

FIG. 21. Temperature dependence of the 91 cm^{-1} phonon absorption line in $\mathbf{E}_1\|\mathbf{a}$ polarization. Spectra have been offset by 50 cm^{-1} in vertical direction.

140 cm^{-1} line parameters. The absorption lines were fit with Eq. (17). The relation between the real part of the conductivity and dielectric function is $\sigma_1(\omega)=\omega\,\mathrm{Im}[\epsilon(\omega)]/60$, where σ_1 is in units $\Omega^{-1}\mathrm{cm}^{-1}$ and Eq. (15) was used to calculate σ_1 from the measured absorption spectra. The fit parameters are plotted in Fig. 22. The phase θ [Fig. 22(d)] changes from $3\pi/2$ at 35 K to π at 33 K where the line has the shape of an antiresonance (Fig. 21). At 31 K the line has a derivativelike line shape again, but with a phase $\pi/2$. Also the phonon resonance frequency ω_p stays fairly constant at higher temperatures and changes abruptly at 35 K. The line area S and γ have a smooth T dependence around $T_c=35$ K. At 4.4 K $\theta=0$ and the normal line shape is recovered. The line width γ [Fig. 22(a)] goes down with T and is limited by the 0.4 cm^{-1} instrumental resolution for this T dependence study. We know from the higher-resolution measurement that the linewidth is 0.2 cm^{-1} or less at 4.4 K. The line area [Fig. 22(c)] has a different T dependence than other parameters, having a minimum at ≈ 32 K. S changes substantially even above T_c, by a factor of 2 from 35 to 40 K.

In this paper we will not present a theory covering the optical conductivity of a system where phonons interact with a two-particle continuum of magnetic excitations. A proper theory must account for a microscopic mechanism responsible for the optical absorption continuum.[51] Nevertheless, some observations can be made based on the empirical fit of the phonon line shape. The phase θ that is related to the Fano parameter q, $q^{-1}\propto\tan(\theta/2)$, which depends on the strength of the interaction between the phonon and the magnetic system. The T dependence of θ shows that the spin-phonon interaction weakens as T is lowered below 35 K. The other reason why the normal line shape of the 91 cm^{-1} phonon at low T is recovered could be vanishing of the two-particle absorption continuum below 130 cm^{-1}. The direct evidence

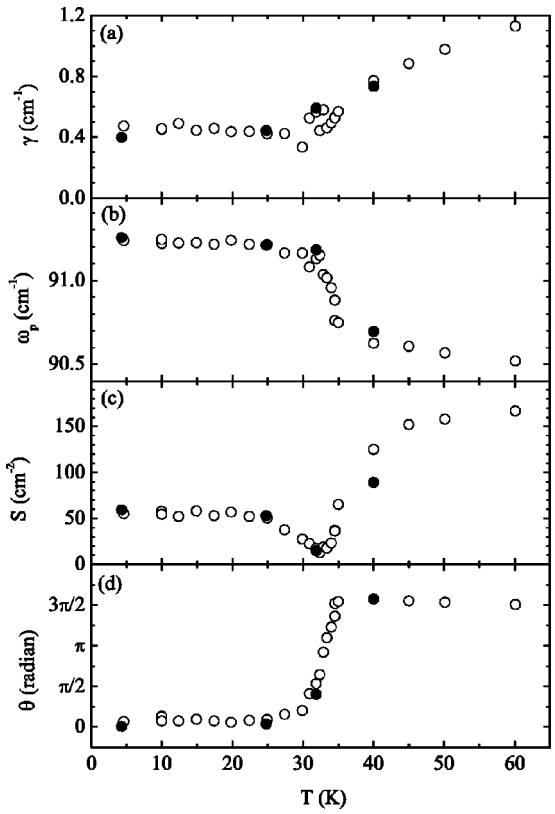

FIG. 22. Temperature dependence of the Fano fit parameters of the 91 cm^{-1} phonon line: (a) Full width at half maximum γ, (b) phonon resonance frequency ω_p, (c) integrated line area S, (d) asymmetry parameter θ. Open circles, 120 μm thick sample; filled circles, 40 μm thick sample.

that the spin-phonon interaction is switched off or is very weak at low temperatures is the Lorentzian shape of the 140 cm^{-1} phonon line.

In conclusion, our data show that there is an absorption continuum in the a-axis polarized optical absorption that develops a gap at low T. This gap, 130 cm^{-1}, is equal to twice the singlet-triplet excitation energy, 65.4 cm^{-1}. Therefore the absorption continuum can be assigned to an absorption of a photon with a simultaneous creation of two magnetic (spin) excitations. Two low-frequency a-axis polarized optical phonons at 91 and 140 cm^{-1} interact with the magnetic system as evidenced by their derivativelike line shape in the high-T phase.

VI. CONCLUSIONS

Using far-infrared spectroscopy we have probed spin excitations and phonons in the quarter-filled spin ladder compound α'-NaV_2O_5. The interaction between the spins and the phonons is observed in the gapped spin state below 34 K and above, in the paramagnetic phase.

The zigzag charge order within the ladders in the gapped state is in accordance with the polarization dependence of several infrared-active zone-folded optical phonons. In the high-T phase two a-axis optical phonons interact with the continuum of excitations as manifested by the Fano line

shape of phonon lines. At low T the continuum absorption is gapped with a threshold energy 130 cm^{-1}, twice the singlet-triplet gap, and the interaction between the phonons and the continuum of excitations is turned off.

The strength of the singlet to triplet absorption at 65.4 cm^{-1} is strongly anisotropic. Absorption is strongest when the electric field of the incident light is polarized along the ladder rungs ($\mathbf{E}_1 \| \mathbf{a}$). In this polarization the strength of the singlet to triplet absorption has a weak magnetic-field dependence up to 28 T. In $\mathbf{E}_1 \| \mathbf{c}$ polarization a strong magnetic-field dependence of the singlet-triplet absorption is observed. This field dependence is due to the dynamic DM interaction created by the 68 cm^{-1} c-axis optical phonon. In the case of the dynamic DM absorption mechanism the singlet-triplet absorption is electric dipole active and the polarization of the transition is determined by the polarization of the optical phonon creating the dynamic DM interaction by the lattice deformation. Using the presented theory we calculated the strength of the dynamic DM interaction. The dynamic DM interaction, $qD_Q = 0.13$ cm^{-1}, created by the 68 cm^{-1} c-axis optical phonon is interladder between the spins in the neighboring planes and points along the b axis. We assign the strong a-axis polarized absorption also to a dynamic DM effect, in this case due to the lattice deformation caused by one of the high-frequency a-axis optical phonons. This dynamic DM interaction is intraladder and is along the c axis. Above 28 T an increase in the S to T_+ a-axis absorption intensity is observed. The origin of the mechanism responsible for that increase is not clear and additional measurements above 33 T are required.

To summarize, the optical singlet to triplet transition in α'-NaV_2O_5 is dominated by an electric dipole active mechanism. We have observed the resonant enhancement of the singlet to triplet transition close to the c-axis 68 cm^{-1} mode. We described the enhancement of the electric dipole transition with the theory of the dynamic DM mechanism and assigned the 68 cm^{-1} mode to a c-axis optical phonon. From the analysis of the phonon infrared spectra we concluded that two types of ladder planes exist with the zigzag charge order along the ladders where the charged stripes across the ladders are aligned approximately in [110] or in $[\bar{1}10]$ directions.

ACKNOWLEDGMENTS

We thank G. Blumberg and O. Cépas for helpful discussions. Work in Tallinn was supported by the Estonian Science Foundation Grants Nos. 3443, 4926, and 4927. A portion of the work was performed at the National High Magnetic Field Laboratory, which is supported by NSF Cooperative Agreement No. DMR-0084173 and by the State of Florida. U. Nagel was supported by a NATO expert visit Grant No. PST.EV.978692.

*Electronic address: roomtom@kbfi.ee

[1] M. Hase, I. Terasaki, and K. Uchinokura, Phys. Rev. Lett. **70**, 3651 (1993).
[2] M. Isobe and Y. Ueda, J. Phys. Soc. Jpn. **65**, 1178 (1996).
[3] Y. Fujii, H. Nakao, T. Yosihama, M. Nishi, K. Nakajima, K. Kakurai, M. Isobe, Y. Ueda, and H. Sawa, J. Phys. Soc. Jpn. **66**, 326 (1997).
[4] W. Schnelle, Y. Grin, and R.K. Kremer, Phys. Rev. B **59**, 73 (1999).
[5] S.G. Bompadre, A.F. Hebard, V.N. Kotov, D. Hall, G. Maris, J. Baas, and T.T.M. Palstra, Phys. Rev. B **61**, R13 321 (2000).
[6] D.C. Johnston, R.K. Kremer, M. Troyer, X. Wang, A. Klümper, S.L. Budko, A.F. Panchula, and P.C. Canfield, Phys. Rev. B **61**, 9558 (2000).
[7] H. Nakao, K. Ohwada, N. Takesue, Y. Fujii, M. Isobe, Y. Ueda, M.v. Zimmermann, J.P. Hill, D. Gibbs, J.C. Woicik, I. Koyama, and Y. Murakami, Phys. Rev. Lett. **85**, 4349 (2000).
[8] S. Grenier, A. Toader, J.E. Lorenzo, Y. Joly, B. Grenier, S. Ravy, L.P. Regnault, H. Renevier, J.Y. Henry, J. Jegoudez, and A. Revcolevschi, Phys. Rev. B **65**, 180101 (2002).
[9] T. Ohama, H. Yasuoka, M. Isobe, and Y. Ueda, Phys. Rev. B **59**, 3299 (1999).
[10] Y. Fagot-Revurat, M. Mehring, and R.K. Kremer, Phys. Rev. Lett. **84**, 4176 (2000).
[11] S. van Smaalen, P. Daniels, L. Platinus, and R.K. Kremer, Phys. Rev. B **65**, 060101 (2002).
[12] K. Ohwada, Y. Fujii, N. Takesue, M. Isobe, Y. Ueda, H. Nakao, Y. Wakabayashi, Y. Murakami, K. Ito, Y. Amemiya, H. Fujihisa, K. Aoki, T. Shobu, Y. Noda, and N. Ikeda, Phys. Rev. Lett. **87**, 086402 (2001).
[13] T. Yosihama, M. Nishi, and Y. Ueda, J. Phys. Soc. Jpn. **67**, 744 (1998).
[14] B. Grenier, O. Cépas, L.P. Regnault, J.E. Lorenzo, T. Ziman, J.P. Boucher, A. Hiess, T. Chatterji, J. Jegoudez, and A. Revcolevschi, Phys. Rev. Lett. **86**, 5966 (2001).
[15] S. Luther, H. Nojiri, M. Motokawa, M. Isobe, and Y. Ueda, J. Phys. Soc. Jpn. **67**, 3715 (1998).
[16] H. Nojiri, S. Luther, and Y. Ueda, J. Phys. Soc. Jpn. **69**, 2291 (2000).
[17] G.S. Uhrig and H.J. Schulz, Phys. Rev. B **54**, R9624 (1996).
[18] G. Bouzerar, A.P. Kampf, and G.I. Japaridze, Phys. Rev. B **58**, 3117 (1998).
[19] W. Zheng, C.J. Hamer, R.R.P. Singh, S. Trebst, and H. Monien, Phys. Rev. B **63**, 144411 (2001).
[20] I. Dzyaloshinskii, J. Phys. Chem. Solids **4**, 241 (1958).
[21] T. Moriya, Phys. Rev. **120**, 91 (1960).
[22] L. Shekhtman, O. Entin-Wohlman, and A. Aharony, Phys. Rev. Lett. **69**, 836 (1992).
[23] L. Shekhtman, A. Aharony, and O. Entin-Wohlman, Phys. Rev. B **47**, 174 (1993).
[24] T. Sakai, O. Cépas, and T. Ziman, J. Phys. Soc. Jpn. **69**, 3521 (2000).
[25] O. Cépas, K. Kakurai, L.P. Regnault, T. Ziman, J.P. Boucher, N. Aso, M. Nishi, H. Kageyama, and Y. Ueda, Phys. Rev. Lett. **87**, 167205 (2001).
[26] O. Cépas, T. Sakai, and T. Ziman, Prog. Theor. Phys. Suppl. **145**, 43 (2002).
[27] R.K. Kremer, I. Loa, F.S. Razavi, and K. Syassen, Solid State Commun. **113**, 217 (1999).

[28] Martin-Puplett spectrometer SPS-200 is made by Sciencetech Inc., Ontario, Canada.
[29] A.I. Smirnov, M.N. Popova, A.B. Sushkov, S.A. Golubchik, D.I. Khomskii, M.V. Mostovoy, A.N. Vasilev, M. Isobe, and Y. Ueda, Phys. Rev. B **59**, 14 546 (1999).
[30] M. Poirier, P. Fertey, J. Jegoudez, and A. Revcolevschi, Phys. Rev. B **60**, 7341 (1999).
[31] A. Damascelli, C. Presura, D. van der Marel, J. Jegoudez, and A. Revcolevschi, Phys. Rev. B **61**, 2535 (2000).
[32] M.N. Popova, A.B. Sushkov, S.A. Klimin, E.P. Chukalina, B.Z. Malkin, M. Isobe, and Y. Ueda, Phys. Rev. B **65**, 144303 (2002).
[33] D. Smirnov, J. Leotin, P. Millet, J. Jegoudez, and A. Revcolevschi, Physica B **259-261**, 992 (1999).
[34] F. Keffer, Phys. Rev. **126**, 896 (1962).
[35] M. Lohmann, H.A. Krug von Nidda, M.V. Eremin, A. Loidl, G. Obermeier, and S. Horn, Phys. Rev. Lett. **85**, 1742 (2000).
[36] Z.V. Popović, M.J. Konstantinović, R. Gajić, V.N. Popov, M. Isobe, Y. Ueda, and V.V. Moshchalkov, Phys. Rev. B **65**, 184303 (2002).
[37] R. Loudon, *The Quantum Theory of Light*, 2nd ed. (Oxford University Press, London, 1983).
[38] B.D. Gaulin, M.D. Lumsden, R.K. Kremer, M.A. Lumsden, and H. Dabkowska, Phys. Rev. Lett. **84**, 3446 (2000).
[39] P. Fertey, M. Poirier, M. Castonguay, J. Jegoudez, and A. Revcolevschi, Phys. Rev. B **57**, 13 698 (1998).
[40] M. Azzouz and C. Bourbonnais, Phys. Rev. B **53**, 5090 (1996).
[41] K. Takehana, T. Takamasu, G. Kido, M. Isobe, and Y. Ueda, Physica B **294-295**, 79 (2001).
[42] P. Lemmens, M. Fischer, G. Els, G. Güntherodt, A.S. Mischenko, M. Weiden, R. Hauptmann, C. Geibel, and F. Steglich, Phys. Rev. B **58**, 14 159 (1998).
[43] M.J. Konstantinović, J.C. Irwin, M. Isobe, and Y. Ueda, Phys. Rev. B **65**, 012404 (2001).
[44] M. Isobe and Y. Ueda, J. Magn. Magn. Mater. **177-181**, 671 (1998).
[45] G. Blumberg, A. Gozar, B.S. Dennis, R.K. Kremer, P. Canfield, and A.F. Panchula (private communication).
[46] I. Loa, K. Syassen, R.K. Kremer, U. Schwarz, and M. Hanfland, Phys. Rev. B **60**, R6945 (1999).
[47] H. Schwenk, S. Zherlitsyn, B. Luthi, E. Morre, and C. Geibel, Phys. Rev. B **60**, 9194 (1999).
[48] G. Breit and E. Wigner, Phys. Rev. **49**, 519 (1936).
[49] U. Fano, Phys. Rev. **124**, 1866 (1961).
[50] C.C. Homes, T. Timusk, D.A. Bonn, R. Liang, and W.N. Hardy, Can. J. Phys. **73**, 663 (1995).
[51] It has been shown by Damascelli *et al.* (Ref. 31) that the direct two-magnon optical absorption is possible because of the asymmetrical charge distribution on the ladder rungs.